Title
Metal-Semiconductor Hybrids and Pt-Ga Alloys for Catalytic Applications

Author
Oba, Fadekemi A.

Publication Date
2015

Metal-Semiconductor Hybrids and Pt-Ga Alloys for Catalytic Applications

By

Fadekemi Adetola Oba

A dissertation submitted in partial satisfaction of the

requirements for the degree of

Doctor of Philosophy

in

Chemistry

in the

Graduate Division

of the

University of California, Berkeley

Committee in charge:

Professor A. Paul Alivisatos, Chair
Professor Gabor Somorjai
Professor Ali Javey

Spring 2015

Metal-Semiconductor Hybrids and Pt-Ga Alloys for Catalytic Applications

by

Fadekemi Adetola Oba

Abstract

Metal-Semiconductor Hybrids and Pt-Ga Alloys for Catalytic Applications

by

Fadekemi Adetola Oba

Doctor of Philosophy in Chemistry

University of California, Berkeley

Professor A. Paul Alivisatos, Chair

Catalyst design using nanocrystals unlocks a wealth of independently tunable parameters which can optimize the catalytic performance of a material. The controlled placement of nanocrystals with distinct size, shape and composition within a single particle combines the advantages of each individual component for targeted reactions. Furthermore, the tailored mixing of two or more elements within a single nanocrystal can lead to novel properties distinct from the single elements themselves. Such parameters can be useful in enhancing the activity, selectivity and stability of a catalyst under reaction conditions. Thus, special attention must be paid to the assembly of such catalysts. Solution phase synthesis is a versatile tool for creating complex nano-architectures in a rational and controlled manner.

Catalytic reactions often have competing unwanted side reactions which lead to deactivation or degradation. Nanocrystal building blocks can be tuned to address these issues on an atomic level. Furthermore, structure-activity relationships can elucidate information regarding the nature of the active site when the catalyst itself has been carefully designed, assembled and thoroughly characterized. This dissertation covers the colloidal synthesis of platinum and ruthenium loaded chalcogenide semiconductor nanocrystals for applications in water splitting, as well as platinum-gallium alloy nanocrystals for propane dehydrogenation.

Chapter 1 of this dissertation reviews the fundamentals of semiconductor nanocrystals, which covers the basic properties of nanocrystals, background on their colloidal synthesis and requirements to achieving solar water splitting. The design of a platinum and ruthenium loaded core/shell cadmium selenide/cadmium sulfide nanorod is introduced. Chapter 2 discusses the synthesis of this four component heterostructure, detailing crucial considerations that must be addressed when assembling such multicomponent structures. Initial photocatalytic studies are presented at the end, followed by synthetic approaches to replacing ruthenium with iron or cobalt oxide based materials. Chapter 3 reviews some fundamentals of metal nanocrystals and the synthesis/applications of alloys in heterogeneous catalysis. A brief background on propane dehydrogenation is provided, with a succinct description of major problems encountered and proposed solutions. This precedes the synthetic development and characterization of platinum-gallium nanocrystals for propane dehydrogenation in Chapter 4. Chapter 5 presents the *in-situ* monitoring of structural changes which occur under experimentally relevant conditions and initial propane dehydrogenation studies. Concluding remarks are summarized in Chapter 6, followed by an appendix of additional results and references.

Table of Contents

Chapter 1. Semiconductor Nanocrystals: Fundamentals, Synthesis and Photocatalytic Applications

Chapter 2. Dual Metal Loaded II-VI Semiconductors for Photocatalytic Applications

Chapter 3. Metal Nanocrystals: Fundamentals, Synthesis Applications in Heterogeneous Catalysis

Chapter 4. Synthesis of Pt-Ga Nanoparticles for Propane Dehydrogenation

Chapter 5. Propane Dehydrogenation Activity of Pt-Ga Catalysts and their *In-situ* Structural Changes

List of Figures

Tables

Acronyms used

PtAc= platinum acetylacetonate

GaAc= gallium acetylacetonate

GaCl= gallium trichloride

GaN= bis (μ-dimethyl amino) tetrakis (dimethyl amino) digallium

GaNSi= gallium tris (trimethylsilyl) amide

LiNSi= lithium bis (trimethylsilyl) amide

OAc= Oleic Acid

OLAm= Oleylamine

HDD=1, 2-hexadecanediol

SnAc= tin acetylacetonate

EDS= Energy Dispersive X-Ray Spectroscopy

TEM= Transmission Electron Microscopy

XPS= X-Ray Photoelectron Spectroscopy

PDH= Propane Dehydrogenation

XRD= X-Ray Diffraction

HAADF= High-Angle Annular Dark Field Image

TNO= Trimethylamine n-oxide

Acknowledgements

My time spent here at Cal was filled with numerous rich and rewarding experiences from both inside and outside the lab. I am grateful to have had this opportunity to work with talented researchers from a variety of academic levels and backgrounds.

When I first met Professor Paul Alivisatos, I was impressed by his very kind, welcoming attitude and open mind to pursuing science. Working with him has been very gratifying. He gave me the freedom to explore unknown territory while eagerly but patiently awaiting the outcome. You have my enormous gratitude as my advisor throughout my graduate studies. Professor Gabor Somorjai and Naomi Ginsberg were also very supportive during my growth and maturity as a scientist.

I would also like to thank my friends and family. My brother, Ade Oba, and mother, Remi Oba, have been very loving and supportive of my studies here at Cal. Also, my room-mates (Wendy & Lindsey Porter and Melinda Thomas) and other good friends (including Michael & Sandra Wood, Wil & Sydni Hart, Jaymie Lollie, Andrew Gordon, Alisha & Javen Smith and Stephen & Judy Smith) have been there for me in the good times (and bad) … my experience here would have been very different in the absence of these strong familial and enduring ties.

I have worked with several colleagues at different phases of my Ph.D., some at length, others for more intermittently, and yet others were instrumental in providing expertise or useful discussions on various topics, science based or otherwise. These include Lilac Amirav, Selim Alayoglu, Xingchen Ye, Gerome Melaet, Yogesh Surendranath, Myoung-hwan Oh, Qiao Zhang, Karthish Manthiram, Debraj Ghosh, Brandon Beberwyck, Ming Lee Tang, Danny Hellebusch, Trevor Ewers, Tina Ding, Katie Lutker, Jacob Kanady, David Barton, Matthew Lucas, Pete Nickias and David Britt. I am thankful to have met and worked with you all in various capacities. Also, Aditya Limaye was a very hardworking undergraduate researcher whom I had the pleasure of teaching.

Prashant Jain, Jessy Rivest, Jesse Engel, Kaori Takano, David Grauer, Noah Bronstein, Andrew Olson, Jacob Olshansky, Kate Nichols, Vivian Ferry, Lam-Kiu Fong, Son Nguyen, Marcus Scheele and Charina Choi were great lab mates and coworkers to be around. Many thanks.

Lastly, but not the least, I would like to thank Jim Breen (glass blower!), James Wang and Negest Williams for making sure things were always moving forward and offering their assistance in times of need. I also cannot forget my early chemistry professors who were influential in my path to pursuing graduate studies: Drs. Kenward Vaughan, David Saiki and Carl Kemnitz. Carl was an enthusiastic, passionate and brilliant mentor from my undergraduate and early graduate study days. Thank you for always being in your office, with the door wide open, almost any day and anytime.

Chapter 1: Semiconductor Nanocrystals: Fundamentals, Synthesis and Photocatalytic Applications

1.1 Colloidal semiconductor nanocrystals as tunable building blocks

1.1.1 Nanocrystal Fundamentals

Semiconductor nanocrystals are particularly interesting because of the novel physicochemical properties they display in contrast to their bulk counterpart [1]. The electronic energy levels and density of states in the material are size dependent, exhibiting particularly dramatic changes for nanosized materials in which quantum confinement effects are more evident. In a bulk semiconductor, the band-gap energy ($E_g(\infty)$) is composition dependent and is the minimum energy required to excite an electron (e^-) from its ground state in the valence band (VB) into the empty conduction band (CB), leaving a hole (h^+) behind [2]. The effective band-gap, $E_{g,eff}$ (R), of a spherical particle of radius R, is described according to the following equation using the effective mass approximation [2, 3]:

$$\boldsymbol{E_{g,eff}(R) = E_g(\infty) + \frac{\hbar^2\pi^2}{2R^2}\left(\frac{1}{m_e}+\frac{1}{m_h}\right) - \frac{1.8e^2}{\varepsilon R}} \qquad \mathbf{(1.1)}$$

where m_e and m_h are the effective masses of the electron and hole, respectively, and ε is the bulk optical dielectric constant or relative permittivity. At the simplest level, the classical particle-in-a-box model predicts that the energy level spacing increases quadratically with decreasing R. While $E_{g,eff}$ (R) is inversely proportional to R^2 (second term in Equation 1.1) and increases with decreasing R, the Coulombic interaction (third term in Equation 1.1) increases with decreasing R, corresponding to a decrease in $E_{g,eff}$ (R). At small R, the second term of equation 1.1 dominates, hence $E_{g,eff}$ (R) would increase with decreasing R, resulting in absorption and emission at bluer wavelengths.

From a qualitative point of view using Figure 1.1, one can also deduce that the energy level spacing and band gap energy decrease as the number of atoms increases from a single atom or molecule to a bulk solid material. Coupled electron-hole pairs, or excitons, have a characteristic length scale which is defined by the exciton Bohr radius- the distance in an e^--h^+ pair [3]. When the crystallite size is comparable to or smaller than this exciton radius, further spatial confinement of the charge carriers occurs, thereby increasing the energy of the electronic states and the spacing between them (Figure 1.1). At these small sizes, quantum confinement effects have a more significant impact on the optical and electronic properties of the material [2]. The charge carriers which are excited upon light absorption can go on to participate in a host of chemical reactions, particularly those related to solar energy conversion [4], [5]. To date, several complex semiconductor nano-architectures have been successfully synthesized using colloidal synthetic techniques, allowing for tunability in the semiconductor band structure [6]–[8].

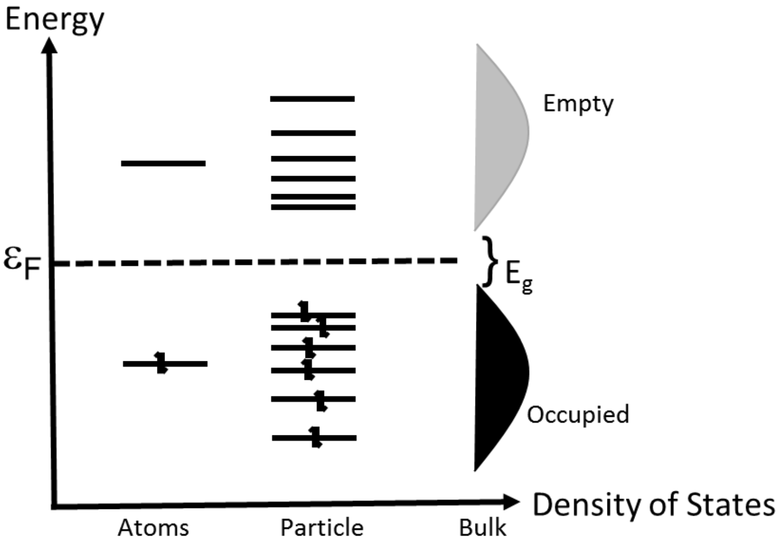

Figure 1.1 Change in electronic energy states for transition of bulk to nano-sized semiconductor

A brief review of the nucleation and growth of colloidal nanocrystals is presented in the following section.

1.1.2 Colloidal Synthesis of Nanocrystals: Nucleation and Growth

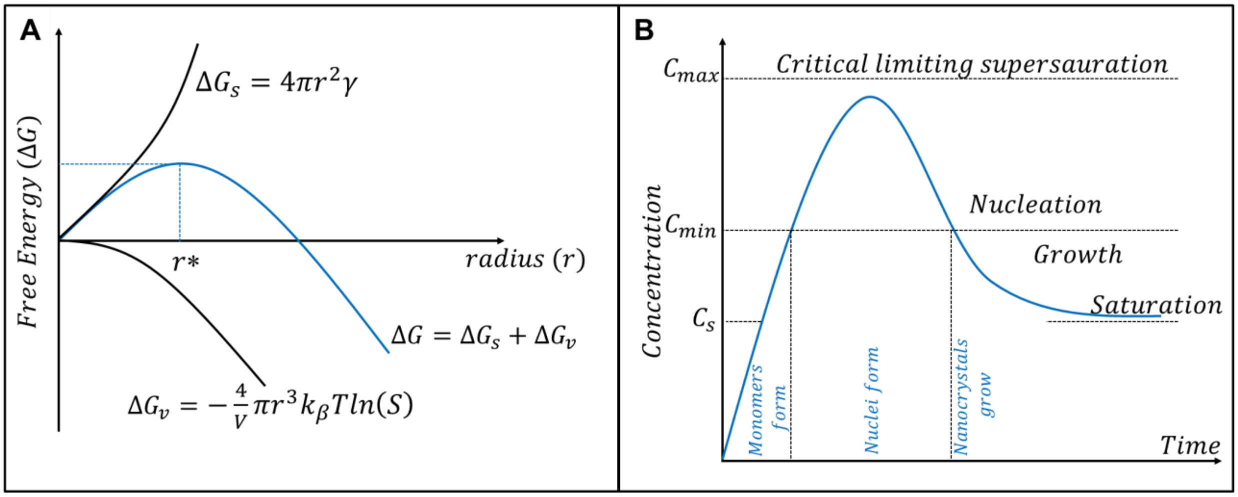

Figure 1.2. (A) Free energy change associated with nanocrystal nucleation. (B) Nucleation and growth stages of nanocrystals

In general, colloidal nanocrystals are synthesized by reacting molecular precursors, such as organometallic compounds or inorganic salts, in the presence of surfactant molecules which precipitate a new solid phase from a homogeneous solution [9] [10]. This occurs in three general stages: formation of monomer species to form a supersaturated solution, burst of nucleation from solution and finally the subsequent growth of nuclei until the desired size is reached (Figure 1.2 b). A supersaturated solution will undergo homogeneous nucleation because of thermodynamics- the solution is not energetically stable. The free energy change (ΔG) that results due to formation of a new surface and new volume can be represented as follows:

$$\Delta \boldsymbol{G} = -\frac{\boldsymbol{4}}{\boldsymbol{V}}\boldsymbol{\pi r^3 k_\beta T ln(S)} + \boldsymbol{4\pi r^2 \gamma} \qquad (\mathbf{1.2})$$

where V is the volume of precipitated species, r is the nuclei radius, k_β is Boltzmann's constant, T is temperature, S is the saturation and γ is the surface energy per unit surface. In this expression, the first term represents the change in free energy associated with a new volume, ΔG_V, and the second term represents the free energy change associated with formation of a new surface, ΔG_S. For the case where S>1, there is a critical nucleus size, r*, where ΔG has a positive maximum (Figure 1.2 a). This represents the activation energy barrier for nucleation to occur. The critical nuclei size can be determined from solving for $\frac{d\Delta G}{dr} = 0$ in equation 1.2 to obtain the following expression:

$$\boldsymbol{r}^* = \frac{\boldsymbol{2V_\gamma}}{\boldsymbol{3k_\beta T ln(S)}} \qquad (\mathbf{1.3})$$

Any nuclei formed which are larger than the critical size will be stable, and further decrease their free energy through continued growth. Thus, all nuclei where r > r* will grow via molecular addition while those nuclei of r < r* will dissolve. Nucleation is terminated once the concentration of the solution drops below the critical supersaturation level needed, followed by nanocrystal growth and a size focusing period. During this focusing event, smaller nanocrystals grow faster than the bigger ones due to the larger thermodynamic free energy driving force over particles bigger than r*. Monodisperse nanocrystals are obtained for reactions in which there is a brief nucleation event (high saturation S) followed by growth which is quenched during the size focusing period. Further reaction time leads to size defocusing from Ostwald ripening, resulting in continued growth of larger particles and dissolution of smaller particles. From equation 1.3, one can deduce that smaller critical nuclei sizes of r* are obtained for a higher saturation S. Furthermore, if the rate of nucleation is slow, then fewer nuclei form, leading to larger nanocrystals. However, if the rate of nucleation is fast, then more nuclei form, rapidly depleting the available monomers for subsequent growth, resulting in smaller nanocrystals.

For heterogeneous nucleation to occur on preformed nanocrystal seeds, the seed must be stable under the experimental conditions and the surface energy of the new phase must not increase the barrier to heterogeneous nucleation over homogeneous nucleation. Furthermore, there must be no diffusion between the components of the deposited phase and the nanocrystal seed. There are three general growth modes of heterogeneous deposition of a material onto another. These are the Franck-van der Merwe, Stranski-Krastanov and Volmer-Weber growth modes (Figure 1.3) [11], [12].

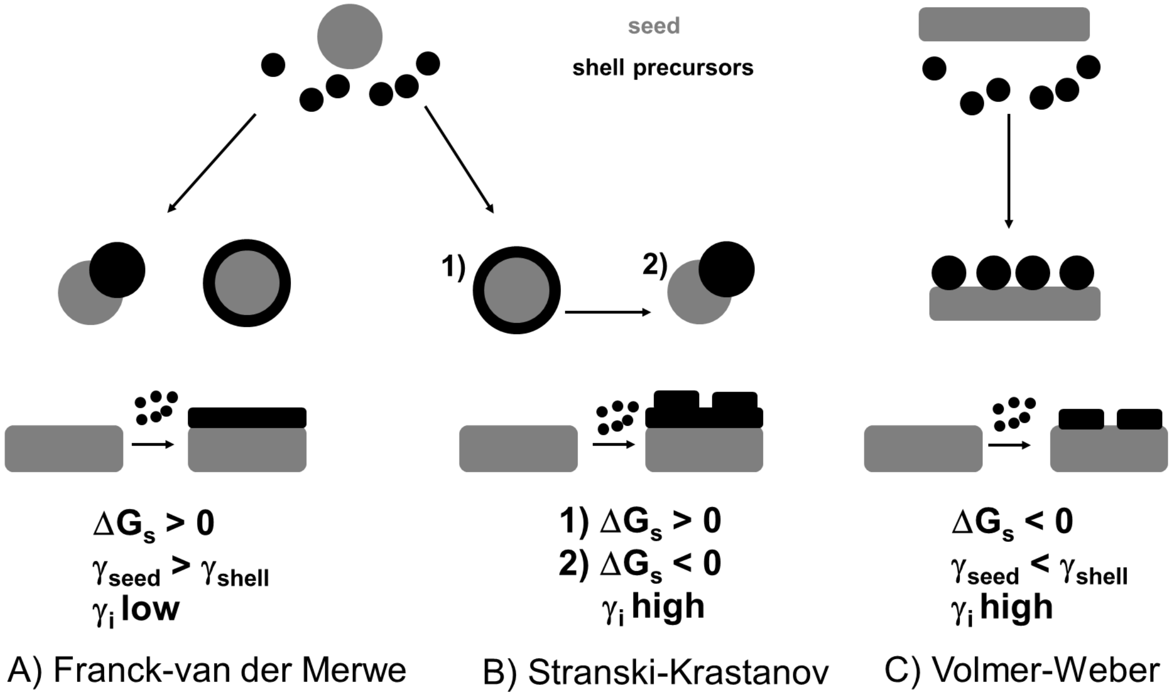

Figure 1.3. (A) Franck-van der Merwe (B) Stranski-Krastanov and (C) Volmer-Weber growth

The overall sign of ΔG_s will determine which growth mode is preferred during the heterogeneous deposition of a new shell over a preformed seed. ΔG_s can be represented according to the following equation:

$$\Delta \boldsymbol{G_s} = \boldsymbol{\gamma_{seed}} - \boldsymbol{\gamma_{shell}} + \boldsymbol{\gamma_i} \qquad (\mathbf{1.4})$$

where γ_{seed} and γ_{shell} are the surface energies associated with the seed and shell materials, respectively, for a solid/liquid interface for colloidal nanoparticles. The surface energy change due to the formation of a new solid/solid interface is denoted as γ_{i}. Dynamic adhesion of surrounding species such as ligands or monomers will affect γ_{seed} and γ_{shell}, while γ_{i} is mainly influenced by the bonding strength and lattice mismatch. If the deposited shell has a lower surface energy and/or low lattice mismatch ($\Delta G_s > 0$), then subsequent deposition will occur uniformly, unless the lattice mismatch among the available seed facets vary considerably such that selective deposition occurs on certain facets. This is referred to as the Franck-van der Merwe mode and can result in either core-shell nanoparticles or dimers (Figure 1.3 a). Furthermore, the growth rate on different facets can affect the final morphology. Slow growth rates are more favorable for uniform deposition to form core-shell structures, while faster growth rates on selected facets might lead to nanocrystal oligomers. In the Volmer-Weber mode ($\Delta G_s < 0$), discontinuous island growth occurs because of the high shell surface energy and/or high lattice mismatch (Figure 1.3 c). The third deposition mode is a sort of mixed growth where the shell initially deposits uniformly ($\Delta G_s > 0$) and once a critical thickness has been exceeded, the interfacial strain can no longer be accommodated, forcing segregation of the shell material into discrete islands ($\Delta G_s < 0$). This is termed the Stranski-Krastanov mode (Figure 1.3 b).

This issue of nanocrystal seed stability will be discussed in further detail in this thesis, as it was a key parameter to accessing multicomponent nanoparticles synthesized through the sequential deposition of a shell onto preformed seeds. Different growth modes were also observed during shell deposition onto preformed metal nanocrystal seeds, leading to different heterostructure morphologies. Typical organic surfactants include phosphonic acids, carboxylic acids, alkylthiols, alkyphosphines and their oxides, and alkylamines. These ligands have a great influence not only on the nucleation and growth kinetics, but also on the stability of seeds used for subsequent material deposition via heterogeneous nucleation. Nonetheless, the controlled deposition of new phases onto preformed seeds has advanced in recent years, and a brief summary of these achievements is presented in the following section.

1.1.3 Recent Advances in Multicomponent Nanoparticle Synthesis

Colloidal inorganic nanocrystals are tunable material building blocks with tremendous chemical flexibility. Exceptional advances in our means for control over the size [13], [14], shape [15], [16], [17] and composition [18]–[20] of solution grown nanocrystals have transformed colloidal synthesis such that it now mimics molecular synthesis [7], [21]. Hybrid nanostructures can exhibit several features synergistically [22] and deliver more than one function simultaneously [23]–[25]. Increasing functional demands of metal-semiconductor hybrid heterostructures have spurred the design of more complex structures which are assembled in a predictable manner through a series of sequential procedures with separately optimized steps.

Examples of metal-semiconductor hybrid nanoparticles are numerous [26]. CdS nanorods have been decorated with Fe_xO_y [27], Au nanoparticles [28][29], tipped with Pt [19], [30], Co [31] and Pt@Co core/shell nanoparticles [32]. Copper sulphide nanoparticles have been encapsulated within inorganic Ru cages [33], AgCdSe tipped Au nanorods have been synthesized with a microphone like morphology [34] and CdSe/CdS/ZnS-Au@hollow SiO_2 yolk/shell nanospheres have been made for catalytic applications [29].

1.2 Semiconductors for Solar Water Splitting

1.2.1 Photocatalytic Hydrogen Generation from Semiconductor Photocatalysts

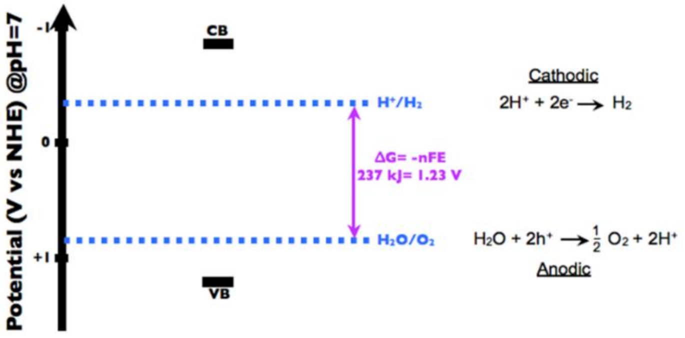

Figure 1.4. Energetic requirements for Overall Water Splitting vs Normal Hydrogen Electrode (NHE)

The photocatalytic splitting of water into hydrogen and oxygen using solar energy is a clean and renewable source of hydrogen fuel. Hydrogen evolution via photoelectrochemical water splitting was discovered in 1972 using an n-type TiO_2 electrode [35]. Since then, though considerable efforts have been invested in developing various photocatalysts, systems that are sufficiently stable and efficient for practical use have yet to be realized [5], [36], [37]. It is particularly difficult to find a photochemically stable semiconductor system with suitable band gap and electron affinity for visible light absorption and for driving the subsequent redox chemistry (Figure 1.4).

First, a photocatalyst must absorb light of $h\upsilon > E_g$ to generate excitons that must separate and migrate towards the surface. There, the e^- and h^+ act as reducing and oxidizing agents to produce H_2 and O_2 respectively. Solar water splitting is a thermodynamically uphill reaction, which has a standard Gibbs free energy change ΔG^0 of 237 kJ/mol or 1.23 V. In theory, a suitable photocatalyst should therefore have at the minimum $E_g > 1.23$ V or < 1000 nm, but to use visible light, a $E_g <$ 3.0 V or > 400 nm is desired. In reality however, water splitting systems operate at higher potentials in order to overcome losses due to the entropic increase required to drive this reaction and the overpotential needed to overcome the oxygen and hydrogen evolution reaction kinetics. In addition, the CB edge should be more negative than the reduction potential of H^+/H_2 (0 V vs NHE at pH 0) and the VB edge should be more positive than the oxidation potential of O_2/H_2O (1.23 V vs NHE at pH 0), as shown in Figure 1.4 above.

Many accounts of photocatalysts which are quite active for water splitting into stoichiometric amounts of hydrogen and oxygen have been reported [5], [36], [37]. Some good examples are based on La doped oxides [38], perovskites [39], Pt loaded III-V tandem cells [40] and $BiVO_4$ [41]. Band Engineering allows for improved charge separation via targeted direction of charge carriers towards distinct interfaces or localized reaction centers [42]–[45]. Cadmium chalcogenides have size dependent band edge energies, large extinction coefficients and advanced synthetic protocols for controlling their dimensions [15], [16], [46]–[51]. Cadmium sulfide (CdS) has been heavily studied for photocatalytic H_2 evolution because of its suitable band gap and band edge energies [52]–[57]. However, its photo-oxidative instability has limited its application, as photogenerated h^+ oxidize the CdS and cause photocorrosion [58]–[61]. For a semiconductor with suitable VB edge, if its thermodynamic oxidization potential is less positive than that of water oxidation, photocorrosion will occur [62]. One way to circumvent this issue is to stabilize the semiconductor using kinetics. Sustainable photochemical reduction at the cathode demands fast h^+ transfer out of the chalcogenide VB to prevent photodegradation [58], [60], [61], [63], [64].

Band engineering using quasi-type II heterostructures are interesting because they spatially separate electrons and holes, slow down their recombination and facilitate transport to the surface to participate in chemical reactions [43]–[45], [65], [66]. Prior studies have used this as a means of stabilizing CdS based photocatalysts by embedding a cadmium selenide (CdSe) quantum dot within a CdS nanorod [54], [55], [67]–[69]. In this construct, the h^+ is three dimensionally confined to the CdSe while the e^- is delocalized along the length of the CdS rod. A reduction catalyst can then be placed on the CdS end to direct proton reduction at a localized site. While this quasi-type II band alignment enhances the stability of the CdSe/CdS core shell system, the issue of stability is still a concern. Fast h^+ transfer out of the CdSe to a sacrificial h^+ scavenger in solution determines the long term stability [58]. A host of synthetic techniques can be utilized to modify the band structure by controlling the size, shape and composition of the components in a nanoparticle [44].

The next chapter focuses on the rational design and synthesis of CdSe/CdS hybrid heterostructures with Pt and Ru at distinct sites, a system which should perform non-sacrificial photochemical reduction and oxidation reactions. Here, placement of an oxidation catalyst where h^+ trapping occurs should rapidly funnel the h^+ out of the CdSe, thereby preventing catalyst degradation. This oxidation catalyst, when used in place of a sacrificial h^+ scavenger, could stabilize the chalcogenide and open a pathway to interesting photo-oxidation reactions.

1.2.2 Rational Design of a Dual Metal Loaded CdSe/CdS Hybrid Heterostructure

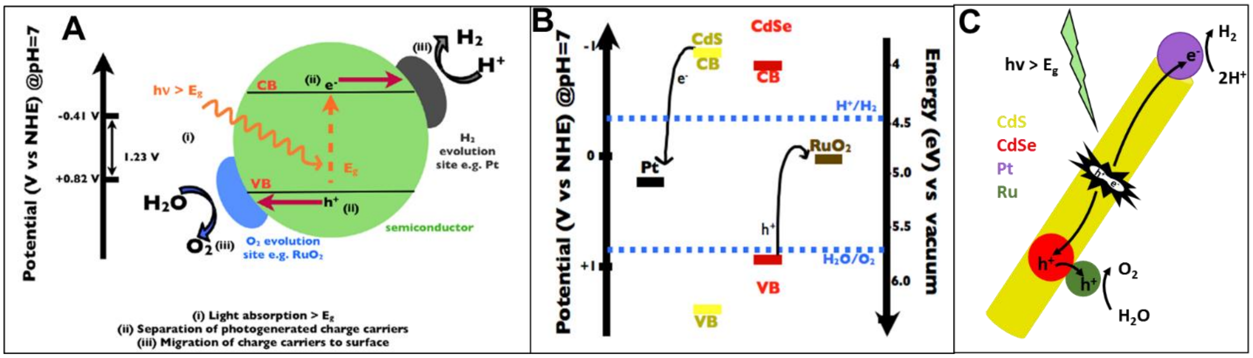

Figure 1.5. (A) Photocatalytic scheme and (B) Band alignment in dual metal loaded CdSe/CdS with corresponding (C) Charge transfer schematic

A cadmium sulfide (CdS) nanorod with an internally embedded cadmium selenide (CdSe) quantum dot was chosen for the light absorption and charge separation events. A platinum (Pt) nanoparticle reduction catalyst was placed on one end of the CdS nanorod and a Ru oxidation catalyst was placed at the CdSe seed. In this construct, electrons delocalized in the CdS are transferred to the Pt, while h^+ localized in the CdSe should be transferred to the Ru oxidation catalyst. This allows for spatial separation of charge carriers across four components as well as a tunable physical distance between distinct reaction sites. Prior work [54] has shown that the CdSe@CdS-Pt combination is highly active for hydrogen production and addition of a Ru oxidation catalyst adjacent to the CdSe is expected to enhance the structure's stability. A schematic and relative band alignment of this four component structure is detailed in Figure 1.5. The fermi levels of the co-catalysts will change under irradation as electrons and holes are transferred to the Pt and RuO_2, respectively. The principles herein can be applied to other nanoparticle heterostructure growth procedures and the synthetic challenges and parameters in designing such a system are discussed in detail in the chapter 2.

Chapter 2: Dual Metal loaded II-VI Semiconductors for Photocatalytic Applications

Reproduced in part with permission from Lilac Amirav, Shaul Aloni and Paul Alivisatos

2.1 Synthesis of Ru and Pt loaded CdSe/CdS heterostructures

2.1.1 Chemicals, Materials and Equipment

Trioctylamine (TOA), triruthenium dodecacarbonyl ($Ru_3(CO)_{12}$), hexadecylamine (HDA), cadmium oxide (CdO), octadecylphosphonic acid (ODPA), propylphosphonic acid (PPA), hexylphosphonic acid (HPA), octylphosphonic acid (OPA), trioctylphosphine oxide (TOPO), trioctylphosphine (TOP), sulfur, selenium, 1,2-dichlorobenze (DCB), oleic acid (OAc), oleylamine (OLAm), dioctyl ether (OE), 1,2-hexadecanediol, phenyl ether, platinum acetylacetonate, methanol, isopropanol, toluene, acetone, chloroform, benzyl ether, monosodium phosphate, disodium phosphate, Ru ICP/DCP standard (10 mg/mL). All syntheses and purification were done under an inert Argon environment, with the exception of the Ru oxide nanoparticles. The flow rate of a 20% O_2/Ar mixture was confirmed by connecting a flow meter to the exhaust from the reaction flask.

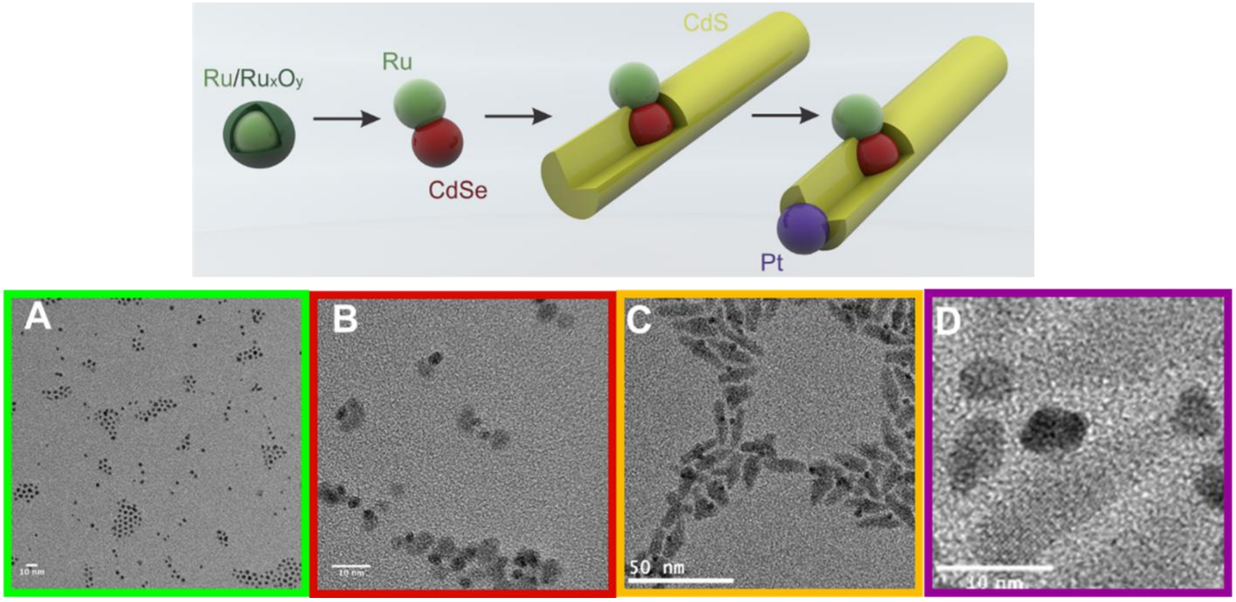

Figure 2.1. Synthetic scheme of Ru-CdSe@CdS-Pt nanorod (top) and TEM starting with (A) Ru@Ru_xO_y (B) CdSe growth onto Ru@Ru_xO_y (C) CdS growth onto Ru-CdSe (D) Pt tipping of Ru-CdSe@CdS

The synthesis commenced with production of Ru nanoparticles that have an oxidized surface, denoted as Ru@Ru_xO_y (Figure 2.1 a). Next, a CdSe quantum dot (Figure 2.1 b) was grown onto the Ru@Ru_xO_y, forming a dimer denoted as Ru-CdSe. These dimers served as seeds for the growth of CdS nanorods exclusively on the CdSe (Figure 2.1 c), denoted as Ru-CdSe@CdS. Conditions were optimized to achieve the greatest percentage of Ru-CdSe dimers with one CdSe dot attached, as this afforded the greatest control in the subsequent CdS growth. Finally, the rods were tipped with a Pt nanoparticle (Figure 2.1 d) on one end of the CdS rod, denoted as Ru-CdSe@CdS-Pt.

TEM images were taken on a FEI G2 20 Tecnai microscope at 200 kV and a LaB_6 filament. HRTEM were taken at the National Center for Electron Microscopy (NCEM) on the FEI Tecnai microscope. Other images were acquired on a JEOL 2100-F 200 kV field-emission analytical transmission electron microscope at the Molecular Foundry, Lawrence Berkeley National Lab. Samples were prepared by drop-casting a few drops of the particle solution in toluene on either ultrathin (20 nm) Si_3N_4 membranes or ultrathin (< 3 nm) carbon on a holey carbon film supported on a 300-mesh gold grid, followed by rinsing with methanol and drying in air. The samples were heated for ~1h at 50 ^oC in a vacuum desiccator and left under vacuum overnight to remove organic contaminants. High-angle annular dark-field (HAADF) images were acquired in STEM mode using a Gatan 806 HAADF detector. Elemental X-ray analyses of the nanorod samples were performed in STEM mode with a 7 Å probe using an Oxford INCA high solid-angle energy dispersive X-ray spectrometer (EDS). EDS mapping images were rendered in Digital Micrograph as pseudo-color maps for clear visualization.

Absorption spectra were taken on an Agilent 8453 spectrometer. XRD patterns were taken on a Bruker GADDS Hi-Start D8 diffractometer with a Co anode at 45 kV/35 mA (λ=1.79 A). ICP-OES was done on a Perkin Elmer 5300 DV optical emission ICP with auto sampler. ICP samples were dissolved in household bleach and the standards were prepared using serial dilution of a commercial Ru standard. XPS was taken on a Perkin-Elmer PHI 5300 ESCA XPS System using a Mg anode. XPS samples were prepared by drop casting a dilute solution of nanoparticles onto a Au coated Si wafer substrate. Once color was evident on the substrate from the nanoparticles, silver paint was added to one corner of the grid to minimize the effects of charging. This was left to dry for at least 2 hours before loading onto an XPS sample holder. All peaks were calibrated in reference to the C 1s peak.

Cyclic Voltammetry (CV) was done (in air) by drop casting *in-situ* oxidized $Ru@Ru_xO_y$ nanoparticles and metallic Ru nanoparticles onto separate glassy carbon working electrodes. An Ag/AgCl reference electrode was used and a Pt wire used for the counter electrode. Scan rates of 0.2 V/sec were applied from -0.3 to 0.88 V. The solution used was 0.1 M monosodium/disodium phosphate pH 7 buffer.

2.1.2 Synthesis of $Ru@Ru_xO_y$ nanoparticles

A. *In-situ* Oxidation

$Ru@Ru_xO_y$ nanoparticles were synthesized using a protocol for Ru nanoparticles, developed by Hoefelmeyer [70], with modifications. The procedure involved thermal decomposition of triruthenium dodecacarbonyl ($Ru_3(CO)_{12}$) in a mixture of hexadecylamine (HDA) and trioctylamine (TOA), while bubbling 20% O_2/Ar through the solution. A 25 ml three-neck round bottom flask containing 1 g HDA and 4 ml of TOA was heated to 60^0C under Ar using standard schlenk line techniques. Then, the system was opened and 90 mg of $Ru_3(CO)_{12}$ powder added. The system was resealed and a 20% O_2/Ar mixture was bubbled into the reaction at 100 ml/min for 1 hour. The temperature was then set to 200 ^0C and the 1 hour duration for the reaction was timed from 90^0C (coincident with an orange to dark brown colour change due to onset of $Ru_3(CO)_{12}$ decomposition). Different flow rates of 10 ml/min, 220 ml/min and 440 ml/min were also tested. Different durations of oxidation tested include 30 minutes and 2 hours. For a standard reaction, after 1 hour, the mixture was quenched with a cool water bath and 4 ml toluene added to the mixture at about 60 ^{0}C. To this mixture, 2 ml of octylamine was added, followed by a 1:1 volume of methanol to precipitate the nanoparticles. After centrifuging at 7500 rpm for 10 minutes, the precipitate was redispersed in 2 ml of octylamine plus 8 ml of chloroform, followed by addition of 10 ml acetone. This was centrifuged and the nanoparticles subjected to two or three more cycles of precipitation and redispersion using chloroform/acetone in a 1.3:1 volume ratio. The final redispersion was in toluene.

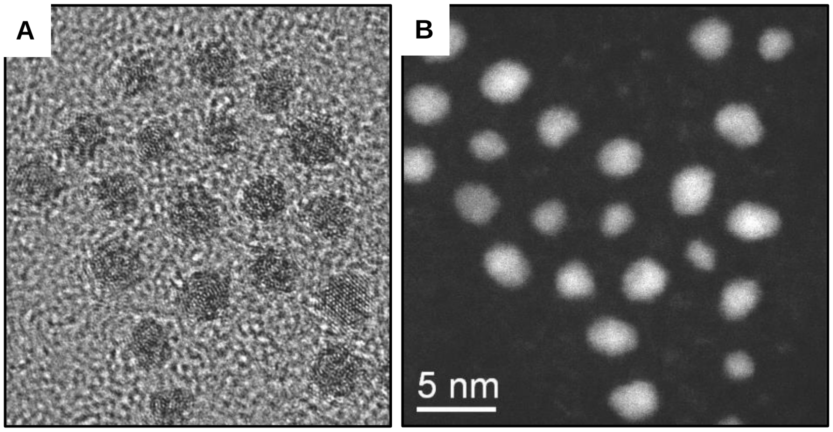

Figure 2.2. (A) HRTEM and corresponding (B) HAADF image of *in-situ* oxidized Ru@Ru$_x$O$_y$

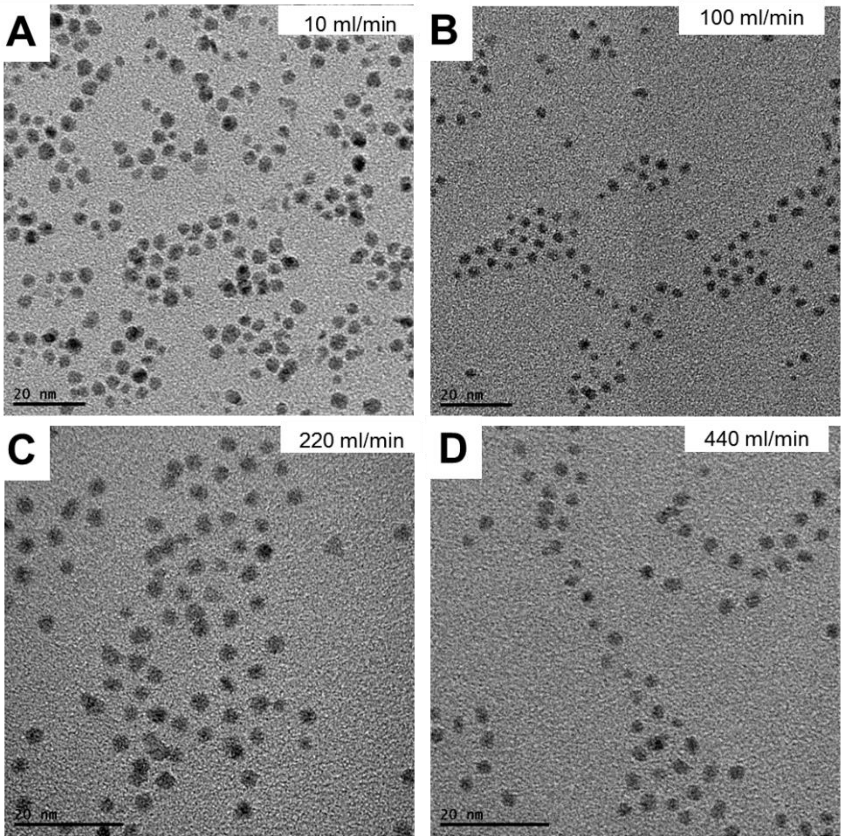

Figure 2.3. TEM of *in-situ* oxidized Ru@Ru$_x$O$_y$ formed using (A) 10 ml/min (B) 100 ml/min (C) 220 ml/min (D) 440 ml/min of a 20% O_2/Argon gas

B. Post-partum Oxidation

This reaction is similar to the in-situ oxidation protocol with a few changes. A 20% O_2/Ar mixture was bubbled into the reaction after metallic Ru nanoparticles had formed. Thus, after 30 minutes of $Ru_3(CO)_{12}$ thermal decomposition at 200 ^{0}C, the temperature was cooled to 100 ^{0}C and 20% O_2/Ar bubbled for 30 minutes or 1 hour. Alternatively, the temperature was maintained at 200 ^{0}C following the thermal decomposition and the same oxidation treatment applied at the higher temperature. Flow rates of 1 ml/min, 11 ml/min, 92 ml/min and 460 ml/min were tested. At the end of each reaction, the reaction mixture was quenched and purified in the same manner as in-situ oxidized nanoparticles. The temperature of postpartum oxidation did not have a major effect on the final Ru-CdSe heterostructures formed, so all results shown in the section on the subsequent CdSe deposition are for Ru oxidized at 100 ^{0}C.

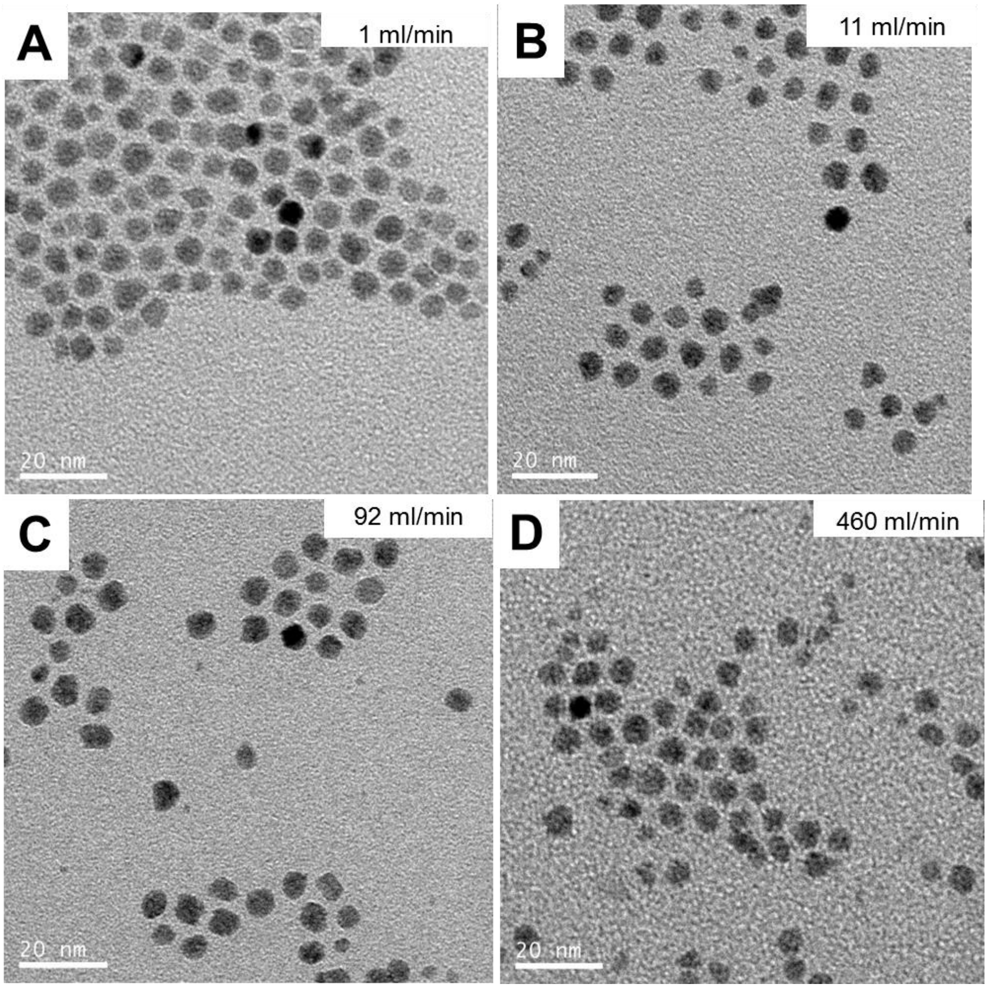

Figure 2.4. TEM of postpartum oxidized Ru@Ru_xO_y formed using (A) 1 ml/min (B) 11 ml/min (C) 92 ml/min (D) 460 ml/min of a 20% O_2/Argon gas at 100 ^{0}C.

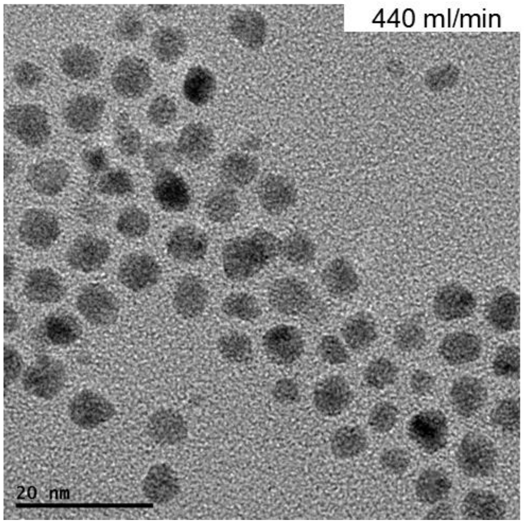

Figure 2.5. TEM of postpartum oxidized Ru@Ru_xO_y formed using 440 ml/min at 200 ^{0}C

C. Metallic Ru

The reaction is similar to the above oxidation protocol, except no 20% O_2/Ar was bubbled into the reaction. Instead, after 30 minutes of thermal decomposition of the $Ru_3(CO)_{12}$ precursor at 200 ^{0}C, the reaction was quenched and purified in the same manner as previously discussed.

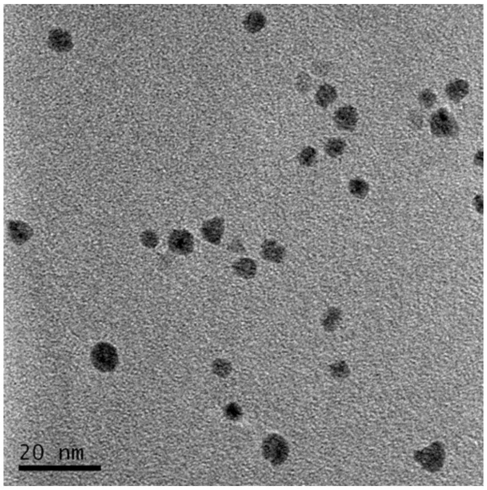

Figure 2.6. TEM of metallic Ru nanoparticles formed without any oxidation treatment

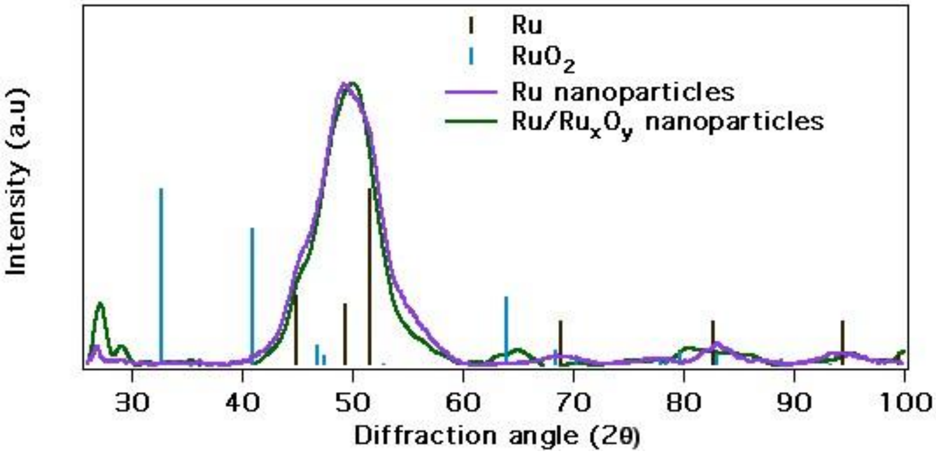

Figure 2.7. X-Ray Diffraction of metallic Ru and Ru@Ru_xO_y nanoparticles, as synthesized

D. Discussion

As seen in Figure 2.2, crystalline Ru@Ru_xO_y nanoparticles were synthesized. The duration of oxidation and the onset of its bubbling through solution with respect to the Ru growth affected the size of the resulting Ru@Ru_xO_y nanoparticles (Figures 2.3-2.6) more so in the *in-situ* oxidation studies. Chemical oxidizing agents, e.g. trimethylamine oxide, were tested but proved unsuccessful for the subsequent heterogeneous deposition of CdSe. Longer in-situ oxidation resulted in smaller diameters while postpartum oxidation of preformed metallic Ru nanoparticles gave bigger nanoparticles.

X-Ray Diffraction (XRD) analysis of Ru@Ru_xO_y nanoparticles suggested a metallic Ru composition with some evidence of Ru oxide formation, presumably at the surface (Figure 2.7). Formation of a Ru oxide species was confirmed using X-Ray Photoelectron Spectroscopy (XPS),

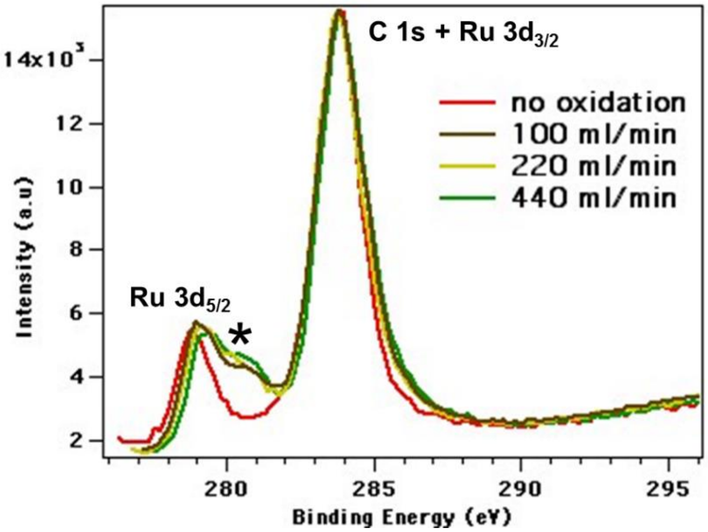

Figure 2.8. XPS of Ru 3d region on in-situ oxidized Ru@Ru_xO_y nanoparticles

where changes in the oxidation state of Ru were monitored in the Ru 3d region (Figure 2.8). The Ru $3d_{3/2}$ peak was much more intense than the Ru $3d_{5/2}$ peak due to its overlap with the C 1s peak. The small blue shift of 0.4 eV in the binding energy of the Ru $3d_{5/2}$ peak in Ru@Ru_xO_y as compared to Ru implies some measure of oxidation occurred. Higher flow rates of O_2/Ar used reveal larger blue shifts of the Ru $3d_{5/2}$ peak, indicating a more oxidized surface resulted with higher flow rates. Furthermore, RuO_2 is typically associated with a broad feature around 281 eV (denoted as * in Figure 2.8), though its origin is still under debate [71]–[73]. All *in-situ* oxidized Ru@Ru_xO_y nanoparticles displayed this feature, which was either absent or undetectable in postpartum oxidized Ru@Ru_xO_y nanoparticles. This distinct feature was later monitored after subsequent CdSe deposition onto the Ru@Ru_xO_y to determine if the oxide survived.

CV was used to determine whether the oxidation treatment had any effect on the electrochemical performance for metallic Ru and *in-situ* oxidized Ru@Ru_xO_y nanoparticles. When metallic Ru nanoparticles were tested on a glassy carbon electrode, no subsequent oxidation in the potential window scanned seemed apparent. In fact, the current continually decreased with subsequent scans. This was in stark contrast to the Ru@Ru_xO_y nanoparticles under the same conditions (Figure 2.9), which showed a marked increase in the current with subsequent scans. It appears that once some oxide was present on the surface, it acts as a nucleation site for further oxidation to occur. Thus, oxidation of preformed Ru was more difficult with the absence of a native surface oxide layer.

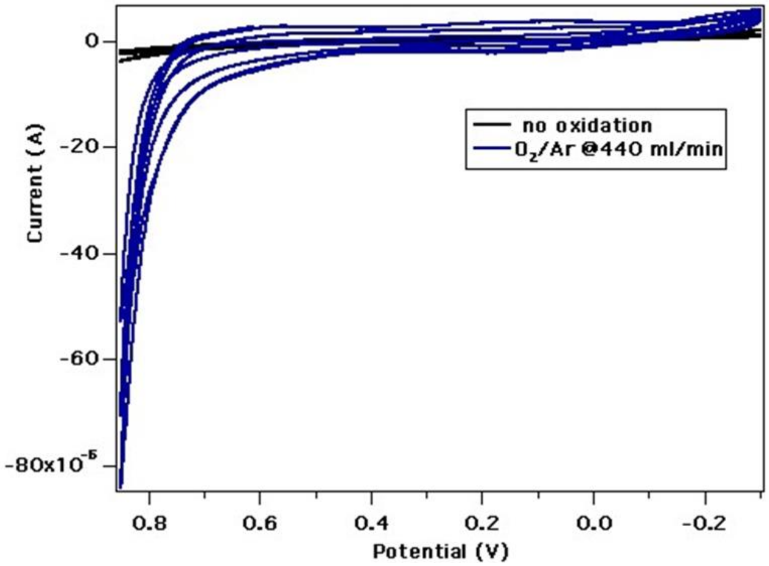

Figure 2.9. CV of metallic Ru nanoparticles vs *in-situ* oxidized Ru@Ru_xO_y nanoparticles

To the best of our knowledge, no protocol yet exists for the preparation of colloidally stable RuO_2 nanoparticles. While bulk RuO_2 nanoparticles can be formed after extended annealing of Ru at high temperatures, this often results in massive sintering and a loss of colloidal stability as the native ligands decompose and expose a bare nanocrystal surface. This was not conducive to subsequent CdSe deposition in a controlled fashion, so mild oxidation conditions were preferred. The size of the Ru nanoparticles may be an important factor to consider when trying to oxidize preformed Ru nanoparticles. Alonso-Vante [74] studied the redox properties of Ru clusters synthesized from $Ru_3(CO)_{12}$ using pure oxygen at temperatures above 200 ^{0}C. They found that once Ru nanoparticles grew past a certain size (on the order of 8 nm), they were resistant to mild oxidation treatments and did not form any bulk RuO_2. On the other hand, they found that 2 nm Ru clusters could be reversibly reduced and re-oxidized to an amorphous Ru_xO_y species under mild oxidation conditions. While they did not check for any surface oxide formation via XPS, it is a telling indicator as to why it was so difficult to synthesize colloidal RuO_2 nanoparticles under our mild oxidation conditions. The larger the Ru nanoparticle, the less likely it is to oxidize under mild conditions.

2.1.3 Synthesis of Ru-CdSe Heterostructures

A protocol for growing CdSe onto preformed Ru@Ru_xO_y nanoparticles was developed. 10^{-7} mol Ru@Ru_xO_y nanoparticles were dissolved in 1 mL 1, 2-dichlorobenzene (DCB), then mixed with selenium (Se) powder and oleylamine (OLAm). Injection of this mixture into a hot solution of cadmium-oleate produced heterostructures of CdSe attached to Ru (denoted Ru-CdSe). A 25 ml three-neck round bottom flask containing 0.5 mmol (64 mg) CdO, 1 ml oleic acid (3 mmol**)** and 5 ml dioctyl ether was heated to 210 ^{0}C under Ar, forming a clear Cd-oleate complex. The Ru@Ru_xO_y /Se/DCB/OLAm injection solution consisted of Ru@Ru_xO_y filtered with a 20 µm PTFE syringe filter, 0.5 ml olelylamine (1.5 mmol) and 0.25 mmol (20 mg) Se powder and was prepared under Ar. A second injection solution consisting of 50-150 mg phosphonic acid (R-PhAcid where R= propyl, octadecyl, hexyl) dissolved in 1 ml DCB at 100 ^{0}C was prepared. Once the Cd-oleate complex was formed, it was cooled to 200^{0}C and the Ru/Se mixture rapidly injected. After 2-4 minutes, the flask was removed from the heating mantle, and the R-PhAcid/DCB mixture rapidly injected when the temperature of the reaction had cooled to 150^{0}C. Once cooled, the particles were collected and 1 ml octylamine was added. To this, a 1:1 volume ratio of methanol was added and the particles precipitated by centrifuging at 6000 rpm for 5 minutes. The particles were subjected to 2 more cycles of redispersion and precipitation using a 1.3:1 volume ratio of chloroform and acetone. The final product was redispersed in toluene. Increasing either the concentration of OAc or OLAm relative to each other was also tested to determine the effect on the shape of the CdSe.

Attempts to grow Ru-CdSe heterostructures in the opposite sequence where Ru was deposited onto preformed CdSe seeds were unsuccessful. Since the sequence of growing CdSe onto preformed Ru was favorable for heterogeneous deposition using the Ru and Se precursors mentioned above, this avenue was investigated further.

A. Using Ru@Ru_xO_y from *in-situ* oxidation

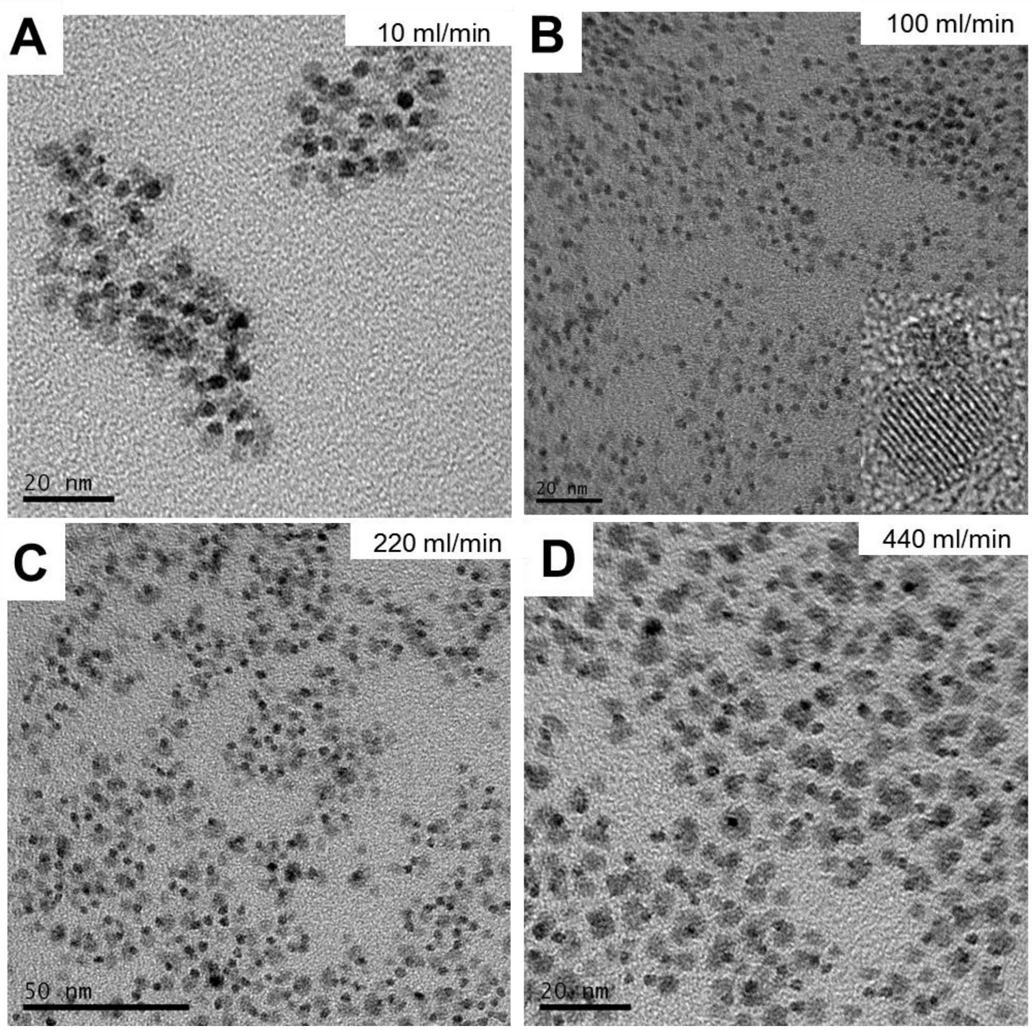

Figure 2.10. Ru-CdSe formed using *in-situ* oxidized Ru@Ru_xO_y nanoparticles from (A) 10 ml/min (B) 100 ml/min (C) 220 ml/min (D) 440 ml/min of a 20% O_2/Argon

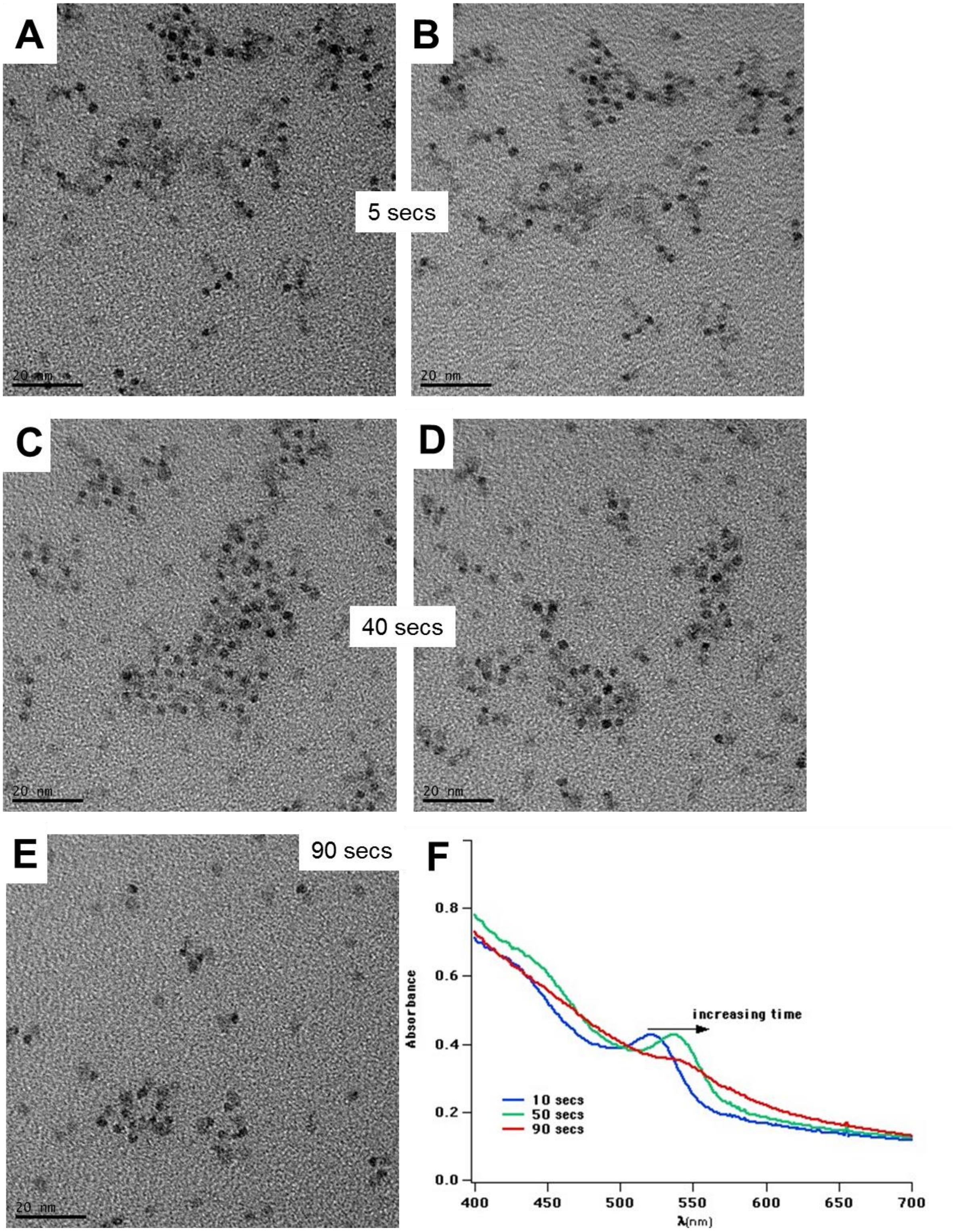

Figure 2.11. Aliquots taken during the CdSe growth onto *in-situ* oxidized Ru@Ru$_x$O$_y$ nanoparticles at (A, B) 5 secs (C, D) 40 secs (E) 90 seconds and (F) corresponding UV-VIS

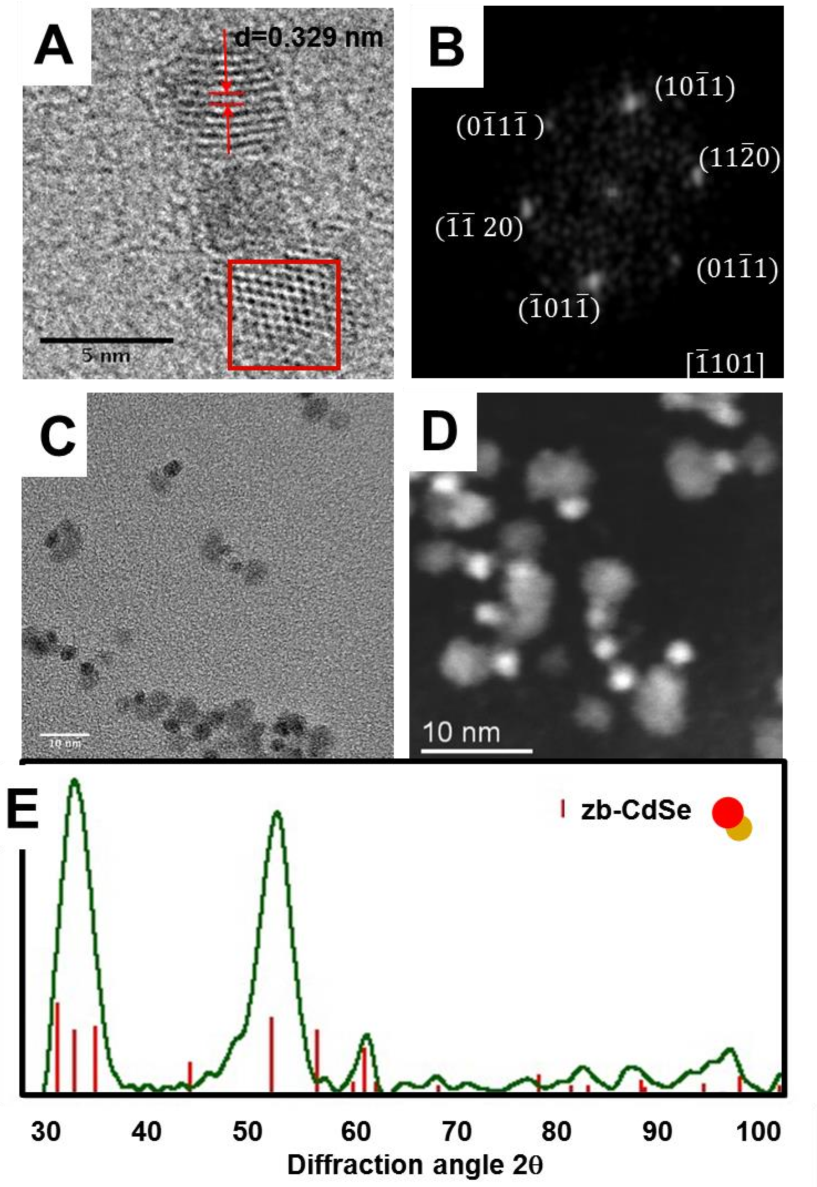

Figure 2.12. (a) HRTEM of Ru-CdSe trimer and (b) corresponding FFT pattern. A low magnification TEM (c) is accompanied by its (d) a HAADF image and (e) XRD pattern

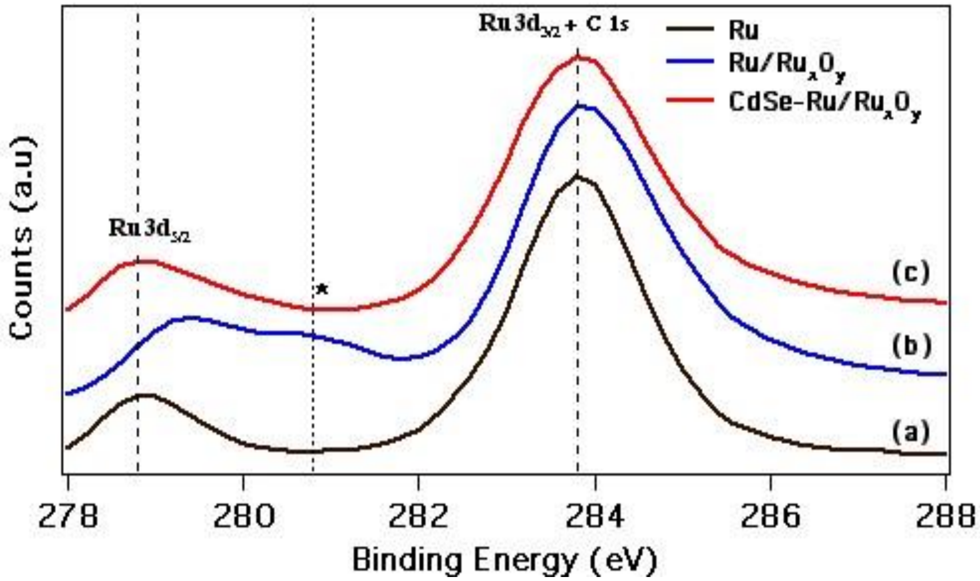

Figure 2.13. XPS spectrum of (a) Ru (b) *in-situ* oxidized Ru@Ru$_x$O$_y$ (c) Ru-CdSe nanoparticles

The primary mode of CdSe deposition and growth seemed to match that of the Franck-van der Merwe mode (Figure 1.3). For Ru@Ru$_x$O$_y$ nanoparticles oxidized at a low flow rate of 10 ml/min, clusters of CdS-Ru are seen (Figure 2.10 a). At higher flow rates, Ru-CdSe hybrids with anywhere from one deposited CdSe nanocrystal to a core-shell Ru-CdSe configuration are seen. A greater percentage of Ru-CdSe dimers form on *in-situ* oxidized Ru@Ru$_x$O$_y$ nanoparticles from medium flow rates (100 and 220 ml/min in Figure 2.10 b and c respectively), while more dumbbell and almost core-shell structures were seen using high flow rates of 440 ml/min (Figure 2.10 d). This suggests that for Ru surfaces which are less oxidized, the CdSe nucleation is restricted. Hence, *in-situ* oxidation at medium flow rates maximized the yield of Ru-CdSe dimers.

Aliquots taken during the first 2 minutes of growth (quenched in a methanol bath) provide some insight into the formation mechanism of CdSe (Figure 2.11 a-f). After 5 seconds, heterogeneous nucleation is evident as CdSe deposition on Ru@Ru$_x$O$_y$ nanoparticles is seen in the TEM images (Figure 2.11 a, b). At this early stage, the CdSe shape is ill defined, having a spindle like morphology. After 40 seconds, the CdSe shape has become well defined and spherical (Figure 2.11 c, d) once they have had time to grow and restructure into their lowest surface energy state. By 90 seconds, the CdSe growth (Figure 2.11 e) has entered the defocusing regime, as seen by the broadened excitonic feature in Figure 2.11 f. Homogeneous CdSe seems to form concurrently with heterogeneous CdSe. Furthermore, flooding the system with Ru@Ru$_x$O$_y$ nanoparticles to eliminate homogeneous CdSe nucleation proved ineffective, suggesting the barrier to CdSe nucleation is similar in both cases.

An electron diffraction pattern indexed from a HRTEM image (Figure 2.12 a, b) suggests a wurtzite crystal structure of CdSe (w-CdSe) was present. The d spacing of 0.329 nm matches the (101) reflection of w-CdSe when imaged along the $[\bar{1}101]$ zone axis. Most likely, both the hexagonal and cubic phases are present, and XRD of CdSe points to a bulk zinc blende (zb) phase

(Figure 2.12 e). Deposition of CdSe onto the Ru@Ru_xO_y nanoparticles was also clearly evident from the TEM and HAADF image in Figure 2.12.

The Ru_xO_y shell was seemingly reduced to metallic Ru during the CdSe growth. It's possible that OLAm acted as a mild reducing agent under these conditions, though heterogeneous nucleation of CdSe still occurred in the absence of any OLAm. XPS revealed the disappearance of the signature feature of RuO_2 at 281 eV and a red shift of the Ru $3d_{5/2}$ peak to that seen in metallic Ru nanoparticles (Figure 2.13). This was found to play a key role in controlling the final morphology of the Ru-CdSe heterostructure, affecting the quantity and location of CdSe deposition. Variations in the oxidation conditions for synthesizing Ru@Ru_xO_y gave control over the hybrid morphology, forming either a core-shell structure, a flower-like decoration, or a dimer with a single CdSe dot attached to the Ru nanoparticle. The variation in CdSe deposition is further explored using Ru@Ru_xO_y nanoparticles with postpartum oxidation in the following section.

B. Using Ru@Ru_xO_y Nanoparticles from post-partum oxidation

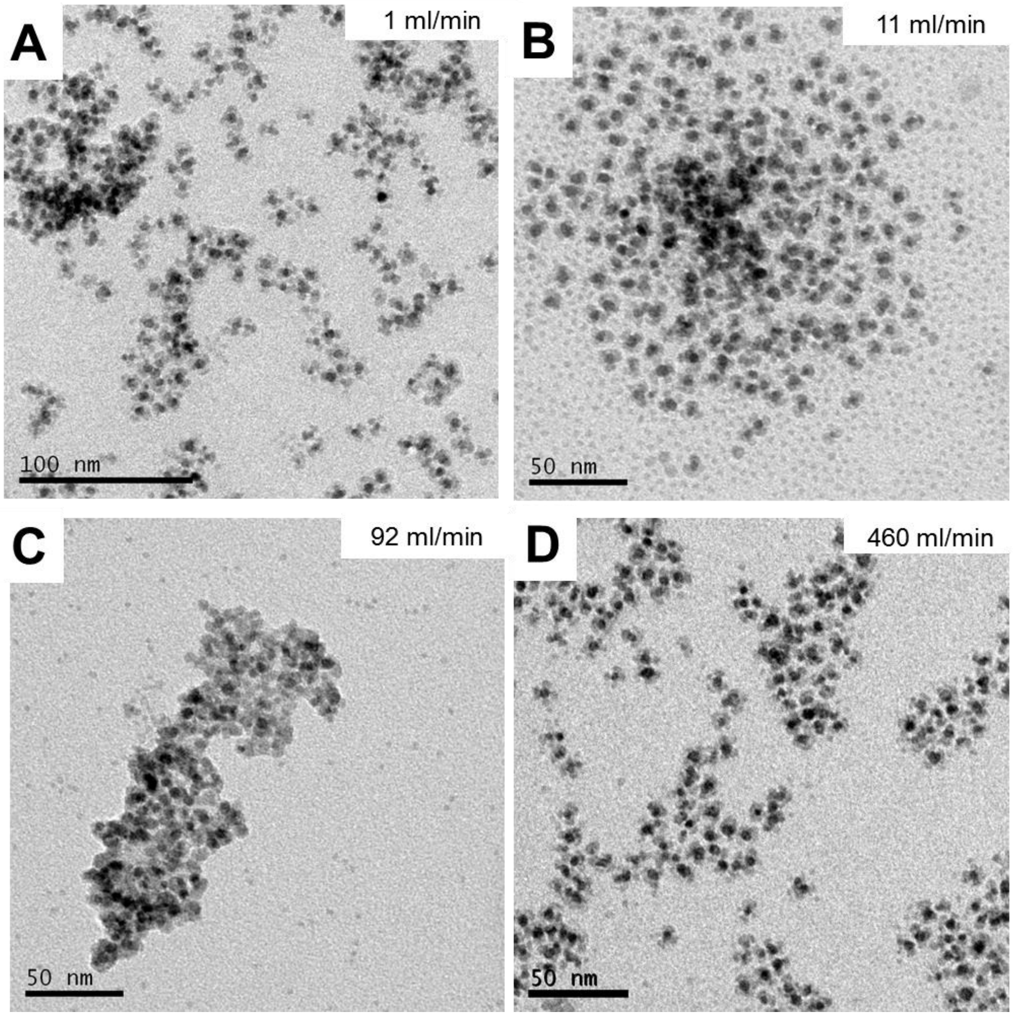

Figure 2.14. Ru-CdSe grown using postpartum oxidized Ru@Ru_xO_y formed from (A) 1 ml/min (B) 11 ml/min (C) 92 ml/min (D) 460 ml/min of a 20% O_2/Argon gas at 100 ^{0}C.

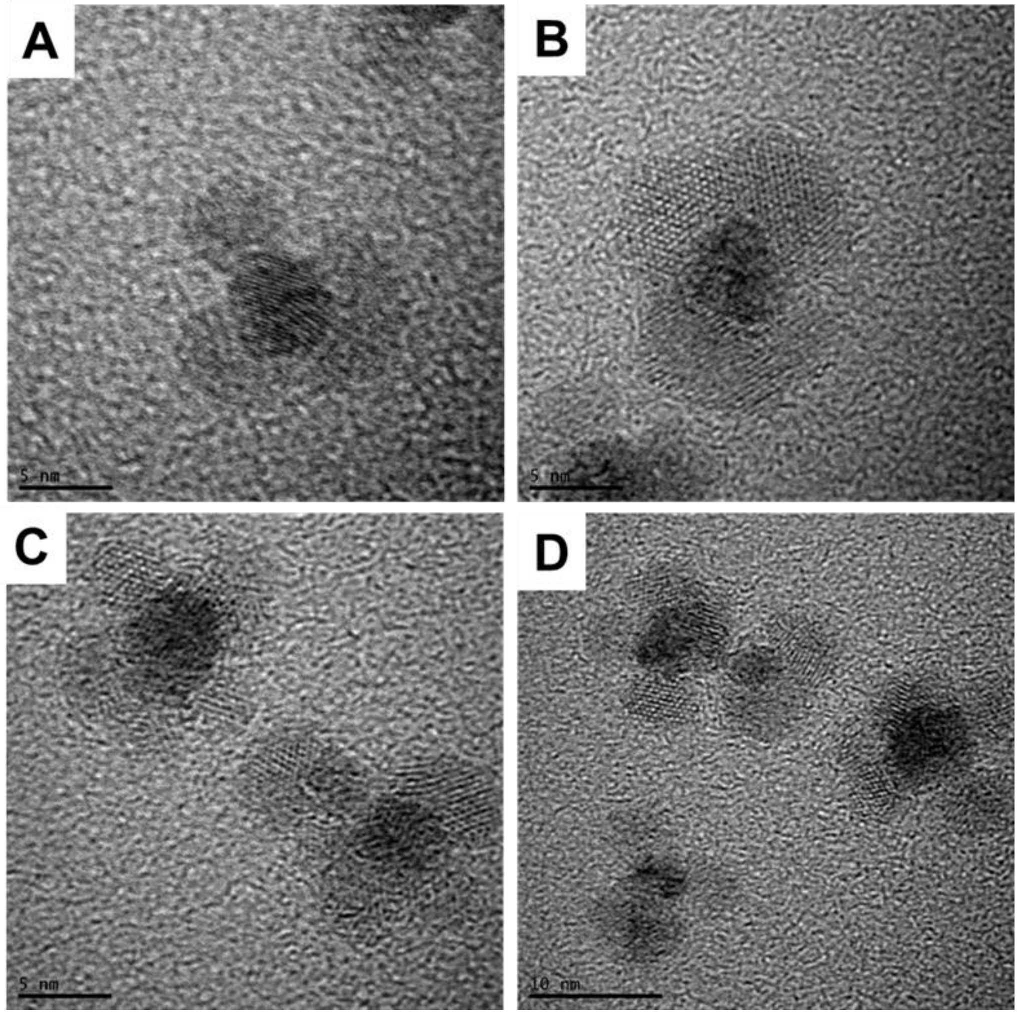

Figure 2.15 (A-D). HRTEM of Ru-CdSe flowers using 460 ml/min postpartum oxidized Ru@Ru$_x$O$_y$

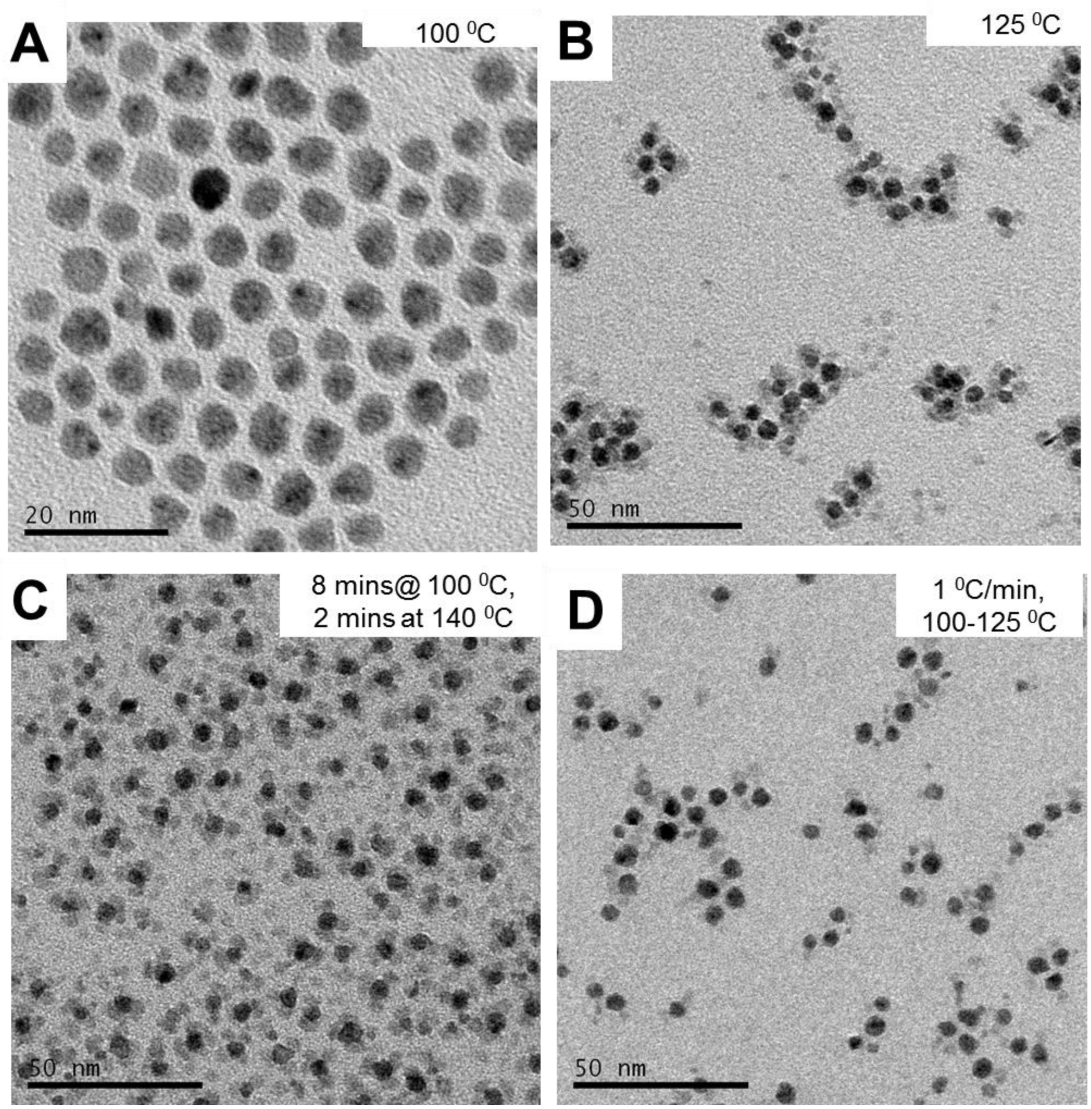

Figure 2.16. Ru-CdSe synthesis at (A) 100 ^{0}C (B) 125 ^{0}C (C) 8 minute soak at 100 ^{0}C followed by 2 minute soak at 140 ^{0}C (D) Temperature ramp of 1 ^{0}C/min from 100 ^{0}C- 125 ^{0}C. (All with 460 ml/min Ru@Ru$_x$O$_y$ under postpartum oxidation)

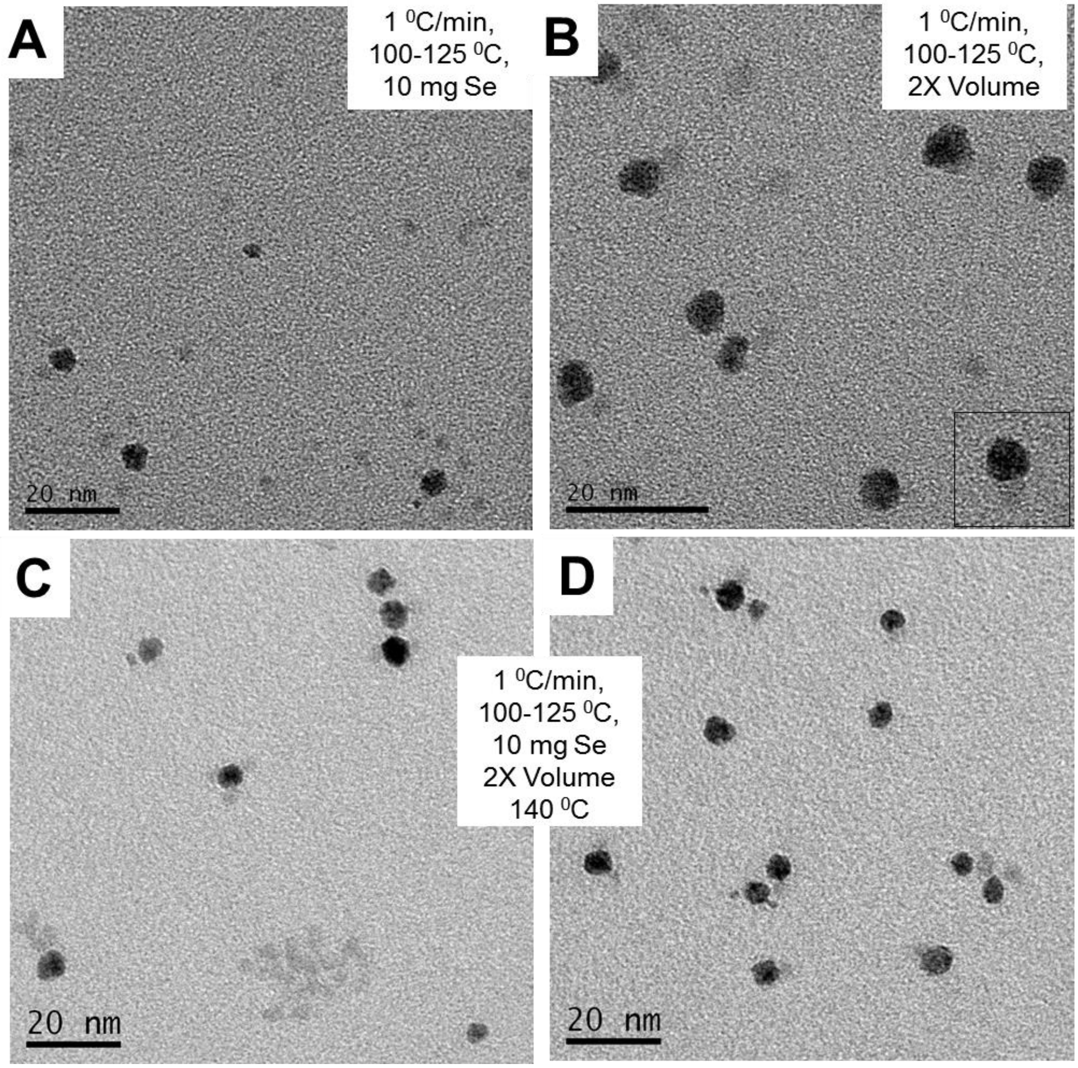

Figure 2.17. Ru-CdSe synthesis using temperature ramp of 1 ^{0}C/min from 100 ^{0}C- 125 ^{0}C and (A) 10 mg Se (B) 10 ml OE (C-D) 10 mg Se and 10 ml OE followed by an abrupt temperature soak at 140 ^{0}C. (All with 460 ml/min Ru@Ru_xO_y under postpartum oxidation)

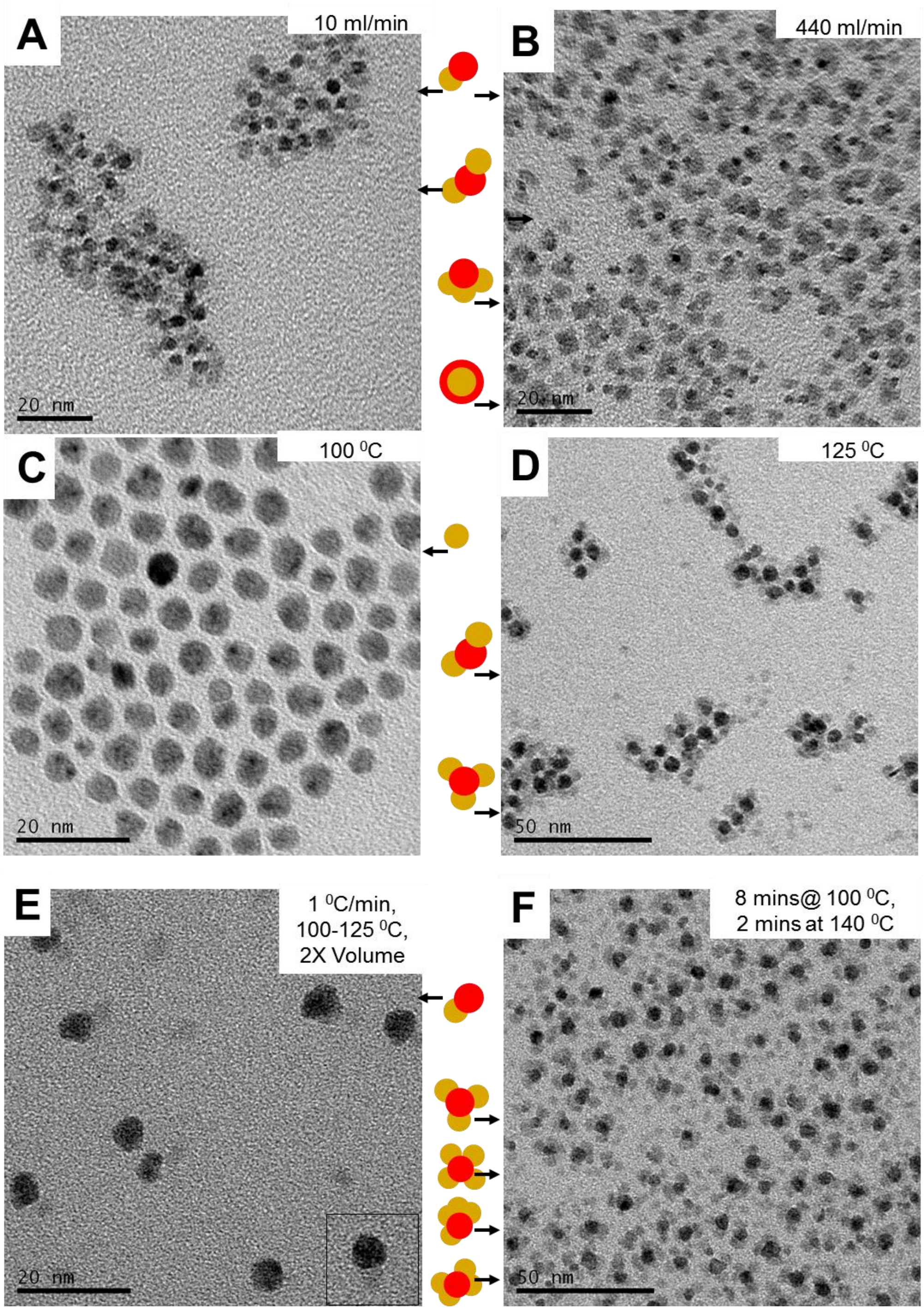

Figure 2.18. Top-down projection summary of different CdSe coverages using Ru@Ru_xO_y from (A) 10 ml/min *in-situ* oxidation, CdSe growth at 200 ^{0}C (B) 440 ml/min *in-situ* oxidation, CdSe growth at 200 ^{0}C (C) 460 ml/min postpartum oxidation, CdSe growth at 100 ^{0}C (D) 460 ml/min postpartum oxidation, CdSe growth at 125 ^{0}C (E) 460 ml/min postpartum oxidation, CdSe growth at temperature ramp of 1 ^{0}C/min from 100 ^{0}C- 125 ^{0}C and 10 ml OE (F) 460 ml/min postpartum oxidation, CdSe growth at 8 minute soak at 100 ^{0}C followed by 2 minute soak at 140^{0}C.

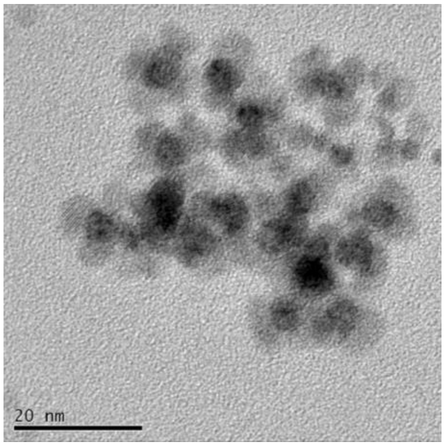

Figure 2.19. Ru-CdSe synthesized using metallic Ru nanoparticles

When CdSe deposition occurred on postpartum Ru@Ru$_x$O$_y$ nanoparticles under similar conditions to the *in-situ* oxidized counterpart, flower-like decoration of the Ru with CdSe occurred (Figure 2.14 a-d). As seen by the HRTEM images (Figure 2.15 a-d), multiple CdSe nuclei were deposited onto the Ru@Ru$_x$O$_y$, though occasionally more closely resembling a complete core-shell architecture. The lattice mismatch of either w-CdSe or zb-CdSe ((110) and (220) respectively) with (002) Ru is calculated to be < 1% but more than 8% for other facets (w-CdSe (102) and zb-CdSe (220) with (100) Ru). Thus, the flower like decoration could be due to facet dependent CdSe deposition, where γ_i played an important role. In addition, larger sizes of the Ru@Ru$_x$O$_y$ domain could allow for more CdSe deposition. To maximize the number of dimers with only one CdSe domain on post-partum oxidized Ru@Ru$_x$O$_y$ nanoparticles, low temperature deposition of CdSe was used to decrease the nucleation rate and number of CdSe nuclei deposited onto the Ru surface.

The minimum temperature for any nucleation of CdSe was between 100 and 125 ^{0}C (Figure 2.16 a-b). Even after a 10 minute soak at 100 ^{0}C, no CdSe was formed until the temperature was increased (Figure 2.16 c) further to 140 ^{0}C. A narrow window of dimer formation was discovered by using a temperature ramp between 100 and 125 ^{0}C, with far less flower-like decoration of CdSe (Figure 2.16 d). This slow increase in temperature proved to be a useful parameter in controlling the nucleation rate such that it only permitted typically one or two CdSe nuclei to be deposited. Further tuning of the nucleation and growth kinetics [75]–[77] was done by modifying the reactant concentration. Halving the [Se] and doubling the reaction volume (Figure 2.17 a and b respectively) or combining these two parameters further restricted CdSe deposition (Figure 2.17 c, d). The number of CdSe nuclei deposited does not change if the temperature is further increased (Figure 2.17 c, d) after CdSe nucleation has occurred. The limiting step in this technique was maximizing the yield of Ru that had CdSe attached, as many bare Ru@Ru$_x$O$_y$ nanoparticles were seen in these TEM.

In summary, a greater percentage of Ru-CdSe dimers is preferentially produced using either a medium flow rate, *in-situ* oxidized Ru@Ru$_x$O$_y$ nanoparticles or a slow, low temperature ramp on postpartum oxidized Ru@Ru$_x$O$_y$ nanoparticles. This transitioned to higher occurrences of flower-like and core-shell Ru-CdSe structures when using high flow rate, *in-situ* oxidized Ru@Ru$_x$O$_y$

nanoparticles and postpartum oxidized Ru@Ru$_x$O$_y$ nanoparticles under the same experimental conditions. The nucleation of CdSe was also found to occur as low as 125 ^{0}C. In the absence of the oxide shell, growth on metallic Ru nanoparticles also resulted in flower-like and core-shell structures (Figure 2.19). Thus, our findings suggest that a less oxidized surface restricts the CdSe nucleation. It should be noted that attempts to grow Ru onto preformed CdSe proved unsuccessful. Organic solvents of different polarity were also tested and found to have no effect on the final morphology of the Ru-CdSe heterostructures.

C. Controlled morphology of CdSe portion of Ru-CdSe heterostructure

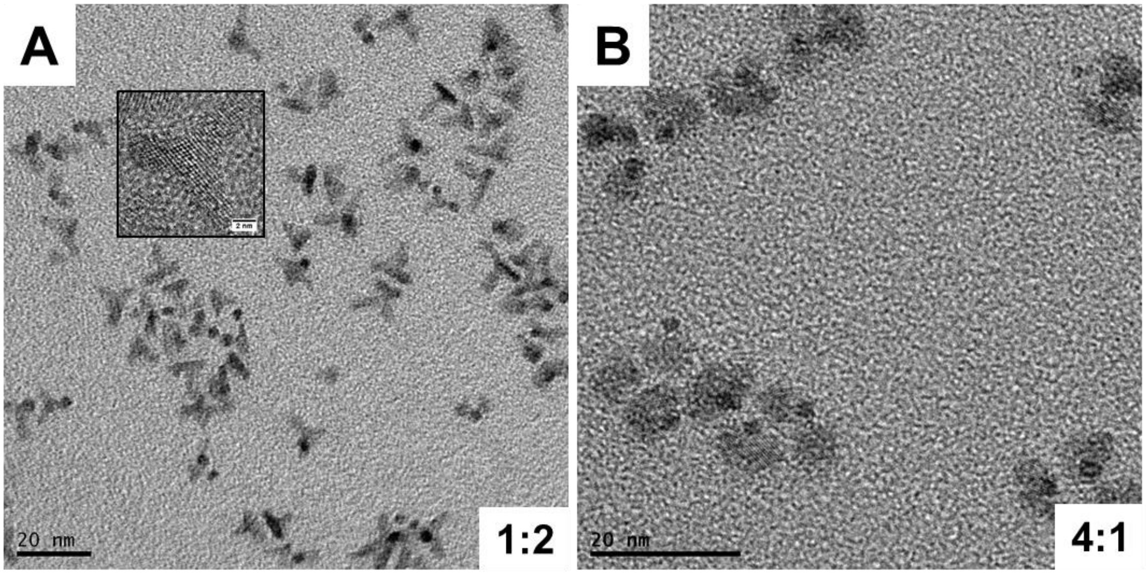

Figure 2.20. Ru-CdSe synthesized using ratios of OAc: OLAm of (a) 1:2 (b) 4:1 on *in-situ* oxidized Ru@Ru$_x$O$_y$

The shape of the CdSe was further tuned by varying the concentration of the oleic acid (OAc) and oleylamine (OLAm) ligands (Figure 2.20). The zb- and w- CdSe phases differ in energy by 1.4 meV/atom, so polytypism is often seen at ambient temperatures [78], [79]. The differences in the CdSe shape result from differences in the ligand binding strength [80] on certain facets which induce either rapid and uniform growth in the case of carboxylic acids or anisotropic growth in high concentrations of amines. Growth is slower on facets with strongly bound ligands, leading to anisotropy. As seen in Figure 2.20, excess oleylamine leads to the growth of CdSe rods but excess oleic acid leads to larger, spherical CdSe growth onto Ru due to its weaker binding in comparison to oleylamine. Furthermore, oleylamine has been shown to favour either a complete zb- to w-crystalline transition for small (2.2 nm) CdSe nanoparticles or a partial transition for 3 nm CdSe nanoparticles [78]. Mahler examined this effect with primary amines on zb-CdSe. Thus, higher concentrations of oleylamine could have also stabilized the CdSe in the w-phase, adding to anisotropic nanorod growth.

2.1.4 Synthesis of Ru-CdSe@CdS Heterostructures

This procedure was adapted from Talapin [50] with modifications. A 25 ml three-neck round bottom flask containing of 1.6 mmol (201 mg) CdO, 1.08 g ODPA, 60 mg PPA* and 3.35 g TOPO was heated to 120 ^{0}C under Ar using standard schlenk line technique. The mixture was then degassed for 30 minutes, then under Ar, the temperature was raised to 320 ^{0}C to form an optically colorless complex. The temperature was cooled to 120 ^{0}C and degassed for 2 hours. Three injection solutions were prepared: 1.5 g TOP, 0.65 g of TOP:S (1:1 mol), and 10^{-8} mol dimers dissolved in 0.5 g TOP. The reaction solution was heated to 340^{0}C and 1.5 g TOP slowly injected into the reaction over 2 minutes. Once the temperature was allowed to reach 340 ^{0}C again, it was cooled to 310 ^{0}C and the TOP:S rapidly injected. After 60 seconds, a 10^{-8} mol Ru-CdSe dimer in 0.5 g TOP solution was rapidly injected and the temperature set to 300 ^{0}C. After 20 minutes, the heating mantle was removed and the reaction allowed to cool to room temperature. Between 90 ^{0}C and 100 ^{0}C, 2 ml of toluene was injected into the solution. Approximately 1.5 ml of both octylamine and nonanoic acid was added to the mixture, followed by a 1:1 volume ratio of isopropanol. The particles were precipitated by centrifuging for 15 minutes at 5000 rpm. The particles were subjected to two more cycles of redispersion and precipitation using a 1.3:1 volume ratio of either chloroform/acetone or toluene/isopropanol, while alternating the addition of either 1.5 ml of octylamine or nonanoic acid. The final dispersion was in toluene.

*PPA can be substituted for HPA or OPA, as was done in the case when exploring the variation of the placement of Ru-CdSe within CdS nanorods. When the chain length of R-PhAcid used at this step was changed in conjunction with the R-PhAcid used to quench the dimers, the location of the dimer within the rod changed.

The concentration of Ru@Ru_xO_y and Ru-CdSe dimer nanoparticles was determined using a combination of ICP-OES and UV-VIS spectrometry. A Perkin Elmer 5300 DV optical emission ICP with auto sampler was used for the analysis. The nanoparticles were dissolved in commercial sodium hypochlorite (bleach) over night. The high temperature Argon plasma used in ICP allows for elemental concentrations in liquid solutions to be analyzed. A serial dilution of 10 mg/L Ru ICP standard was used to make five stock solutions ranging from 0.05 to 50 ppm Ru. Emission at 240 nm and 349 nm were used to determine the concentration of elemental Ru and correlated to the mass of Ru in the dissolved nanoparticle solution. The concentration of Ru nanoparticles was then calculated using its density and size as determined from TEM. A Beer's Law plot (Figure 2.21 a) was used to determine the extinction coefficient of the Ru nanoparticles at 700 nm. This is illustrated as seen below:

The #Ru NPs was calculated according to the following equation:

$$\frac{Mass_{sample} \times Volume_{sample} \times MW_{Ru}}{\rho_{Ru} \times Volume_{dot}} \qquad (2.4)$$

where MW is the molecular weight, and ρ is the density. Ru-CdSe dimers: Assuming the CdSe does not absorb at 700 nm and that every Ru nanoparticle has only one CdSe dimerized to it, the concentration of dimers in the solution was determined using the extinction coefficient of Ru at 700 nm and the corresponding absorption of a Ru-CdSe dimer sample at 700 nm (Figure 2.21 b).

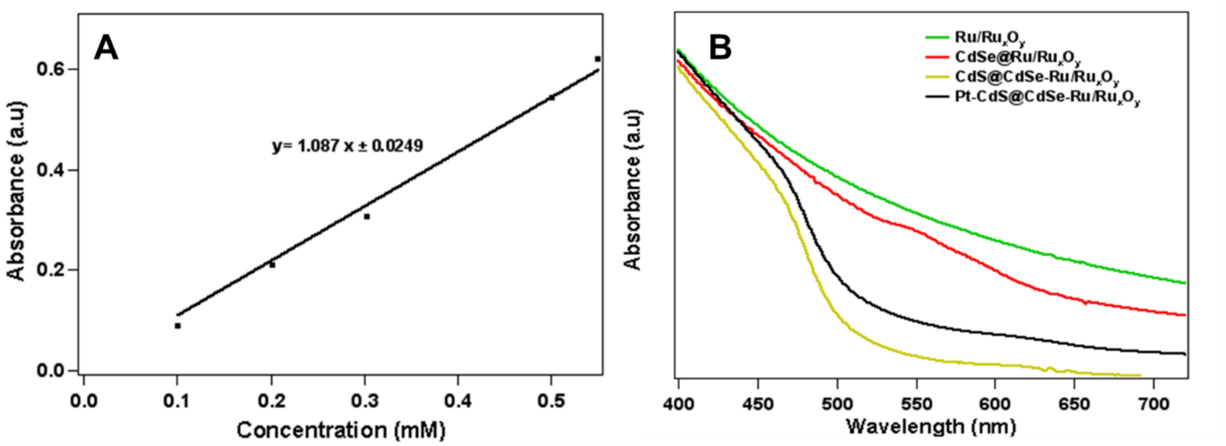

Figure 2.21 (A) Beer's Law Plot for determining the concentration of Ru (B) UV-VIS spectra after each synthetic step

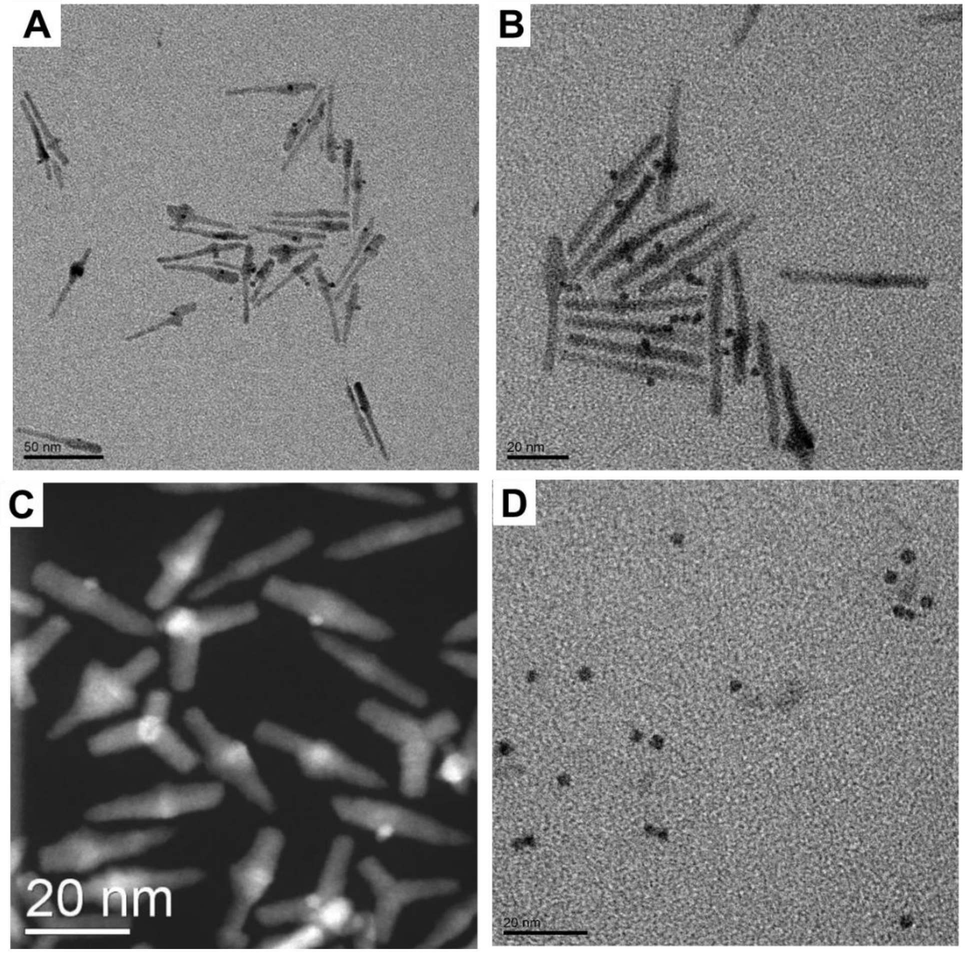

Figure 2.22 (A-B, D) TEM of CdS grown on Ru-CdSe and corresponding (C) HAADF image with (D) detached Ru nanoparticles in the supernatant

CdS growth on the CdSe portion of the dimer was easy to achieve (Figure 2.22 a-c, 2.27 c). However, initial yields of Ru-CdSe@CdS were extremely low. When using dimer hybrids as seeds, rather than simple quantum dots, separate attention should be given to how the subsequent deposition process affects each of the dimer's components. A delicate balance must be attained between the optimized conditions of the CdSe and CdS growths, in order to allow for selective deposition on the Ru-CdSe dimer. Thermal mechanistic aspects of a selective deposition are intertwined with maintaining the stability of the individual components of the dimer. Ligand compatibility considerations convolute their mutual effect on the growth kinetics. One particular challenge in using dimers was seeds was the dimer's stability under CdS growth conditions. TEM images of the black supernatant often seen during the purification revealed small, high contrast, round nanoparticles which were presumably Ru (Figure 2.22 d).

Stronger binding phosphonic acids seemingly displaced the original ligands [80], [81] on the Ru-CdSe dimers during the CdS rod growth, potentially causing widespread separation and dissolution of the CdSe dots attached to the Ru nanoparticles. Displacement of the native ligands on the dimers prior to their purification in a controlled and gradual fashion was found to stabilize them in preparation for the CdS growth. Hence, a solution of phosphonic acid was directly added to the dimers prior to the CdS rod growth. This issue of ligand compatibility was a key parameter for increasing the yield of rods with Ru-CdSe dimers incorporated in them (Figure 2.23 a, b). Flooding the system with Ru-CdSe seeds led to CdS overgrowth of a few nm, along with separate, elongated, homogeneous CdS nanoparticles.

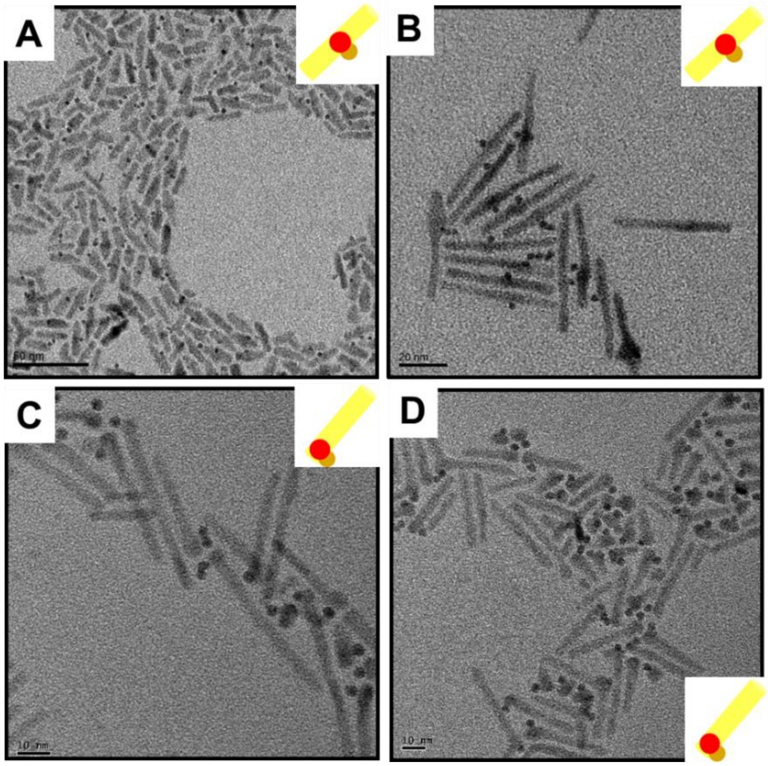

Figure 2.23. Ru-CdSe@CdS with Ru located (A, B) near the centre and (C, D) terminally of the CdS. R-PhAcids were added to Ru-CdSe prior their cleaning as follows: (A) PPA (B) none (C) HPA (D) ODPA. In synthesis of CdS, A and B used 60 mg PPA while C and D used 60 mg OPA

The Ru component of the seed served as a facile visual marker for the location of CdSe within the CdS rod. Its presence enabled us to attain and confirm control over the location of the CdSe (dimerized to Ru) within the CdS rod. The kinetics of CdS growth on the CdSe seed was tuned by replacing the short PPA ligand for longer phosphonic acids both during the dimer quench and CdS growth (Figure 23 c, d). In these instances, the yield of rods with Ru-CdSe dimers incorporated in them was low, as CdS growth on some dimers was not obvious by TEM (Figure 23 d).

Alternatively, if Ru-CdSe hybrids synthesized using a low temperature ramp on postpartum Ru@Ru_xO_y were used as seeds (Figure 2.17), different placements of the CdSe within the CdS were observed, with no obvious preference (figure 2.24). This observation was seen without the use of any PhAcids to quench the dimers post synthesis. Its yield is therefore quite low, as free Ru nanoparticles can be seen in the TEM micrographs as well (Figure 2.24 e). In some cases, the dimer is located near the centre of the CdS rod, but in other cases it is located at the very end. Evidence of branched CdS growth is also seen (Figure 2.24 b)

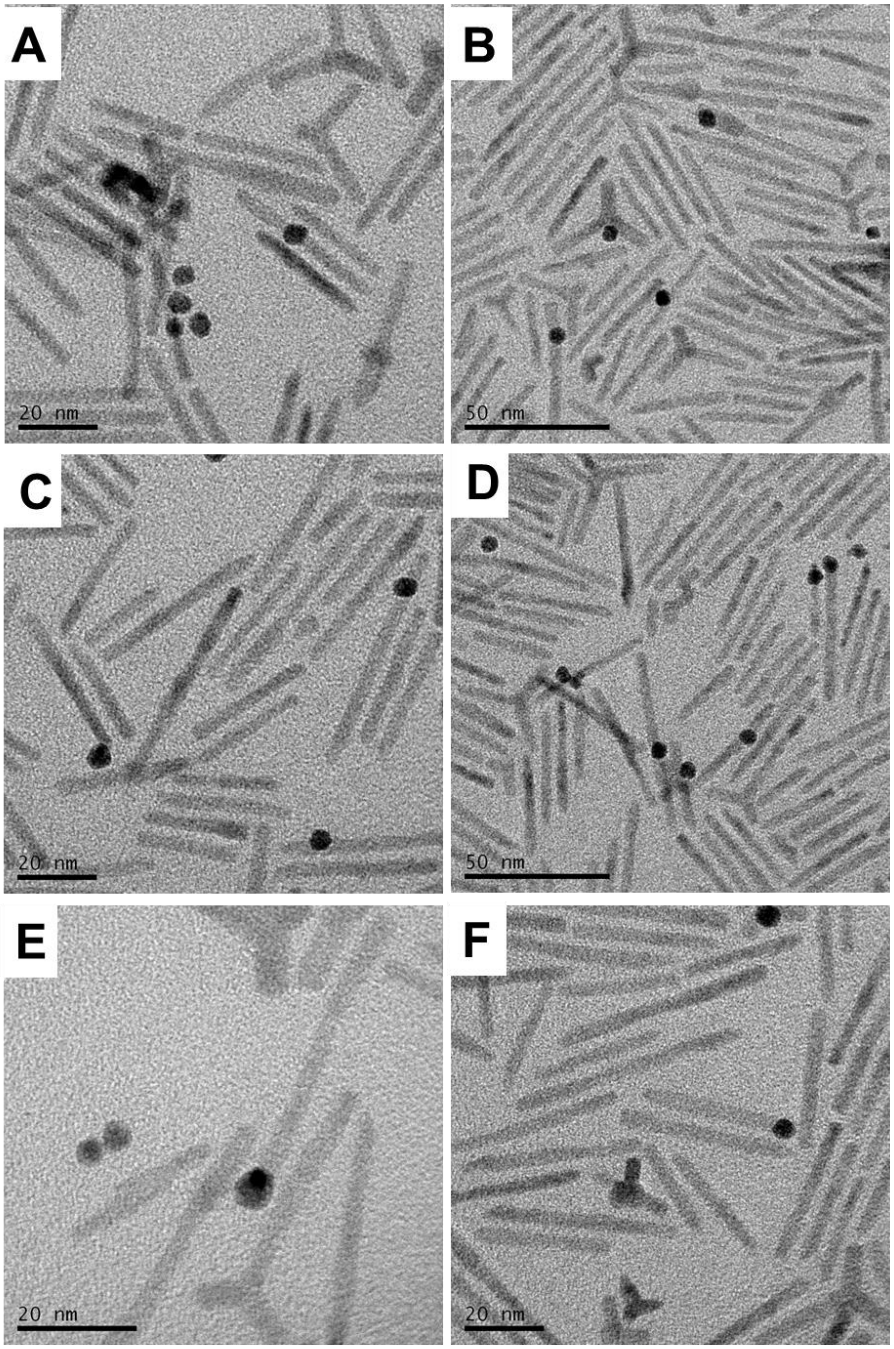

Figure 2.24 (A-F). CdS grown onto Ru-CdSe hybrids synthesized at low temperatures with a temperature ramp and using postpartum oxidized Ru@Ru$_x$O$_y$

The design of the Ru-CdSe hybrid nanoparticles strongly affected the final CdS morphology. Utilization of Ru-CdSe nanoparticles with more than one CdSe dot attached resulted in multiple CdS arms (Figure 2.25).

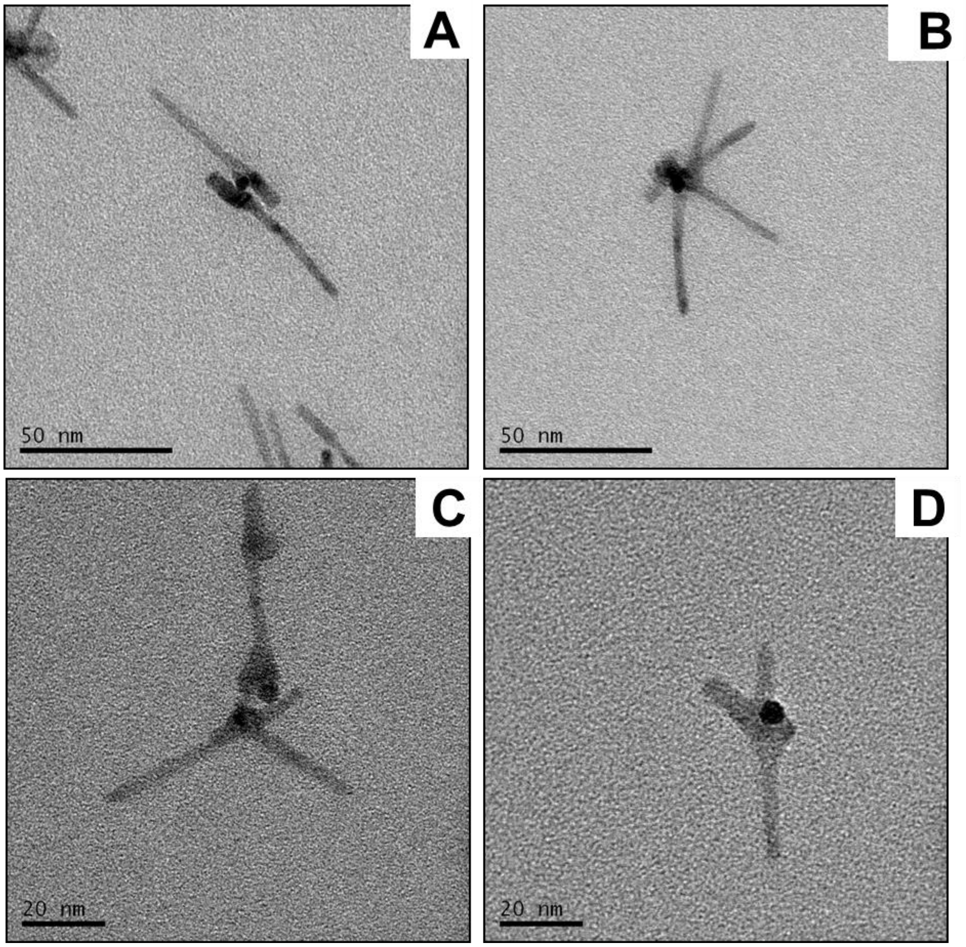

Figure 2.25. (A-D) CdS growth onto Ru-CdSe flowers

2.1.5 Synthesis of Ru-CdSe@CdS-Pt Heterostructures

This procedure was adapted from Mokari [19]. A 25 ml three-neck round bottom flask containing 43 mg 1, 2-hexadecanediol, 0.2 ml of both oleylamine and oleic acid and 10 ml diphenyl ether was heated to 80 ^{0}C under vacuum for 30 minutes. A mixture of 20 mg Pt(acac)$_2$ and Ru-CdSe@CdS rods redispersed in 2 ml o-DCB was heated to 50 ^{0}C under sonication to dissolve the Pt precursor. The reaction mixture was then heated to 200 ^{0}C under Ar, and the Pt precursor solution rapidly injected. After 3-5 minutes, the reaction was rapidly quenched in a water bath and 2 ml chloroform added at about 60 ^{0}C. After addition of 2 ml octylamine, the particles were precipitated with a 1:1 volume ratio of acetone. This was centrifuged at 4000 rpm for 30 minutes. The particles were subjected to two more cycles of redispersion and precipitation with a 1.3:1 volume ratio of either chloroform/acetone or toluene/isopropanol, and finally redispersed in toluene.

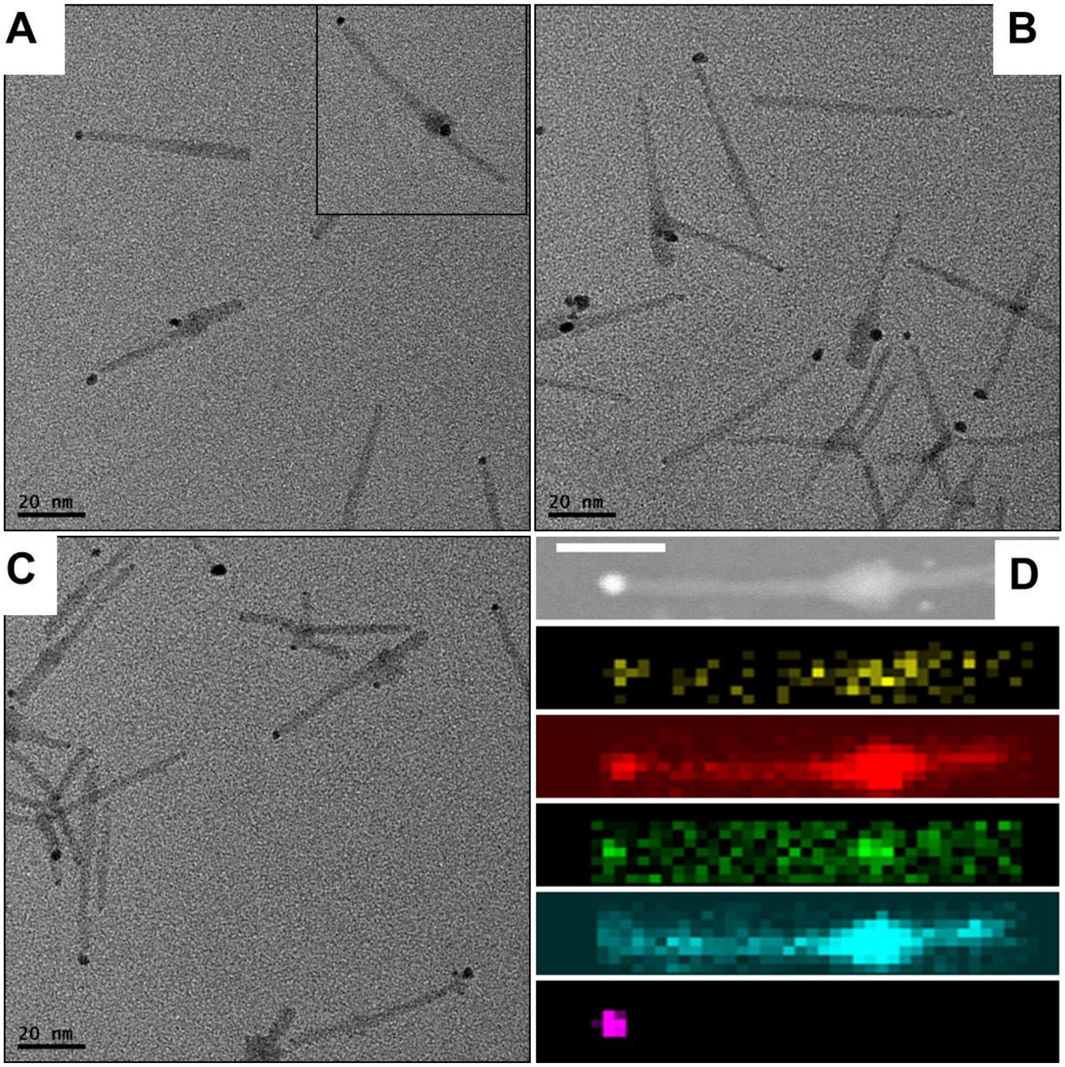

Figure 2.26. (A-C) TEM of Pt tipped Ru-CdSe@CdS nanorods and corresponding (D) HAADF and EDS. In D, Ru L is yellow, Cd L is red, Se L is green, S K is turquoise and Pt M is purple

In the final stage of forming Ru-CdSe@CdS-Pt, Pt was loaded onto one end of the CdS nanorod using an established protocol of thermally decomposing Pt(acac)$_2$ with 1,2-hexadecanediol (HDD) as a reductant (Figure 2.26). The vast majority of Ru-CdSe@CdS-Pt nanoparticles seem to have a localized Pt nanoparticle grown selectively at one end of the rod (Figure 2.26 d). A clear example of such a structures was shown early on in Figure 6 d. Evidence of Pt deposition onto the Ru was found for a minority group of Ru-CdSe@CdS-Pt rods, as determined by EDS (Figure 2.27). This secondary metal deposition is a sensitive parameter, as one can easily lose control over distinct metal nanoparticle placement within a multicomponent structure.

Confirmation that all four materials (Ru, CdSe, CdS and Pt) are present in distinct positions of the hybrid heterostructure was seen in the elemental analysis (Figures 2.27, 2.28). The original design schematic was successfully executed with several tailored synthetic steps. Similarly to advanced organic synthesis, this multistep assembly of colloidal building blocks suffered from low yields. The limiting step overall appeared to be the successful growth of CdS rods on the Ru-CdSe dimers. Nevertheless, this structure represents an advancement in the controlled assembly of hybrid heterostructures.

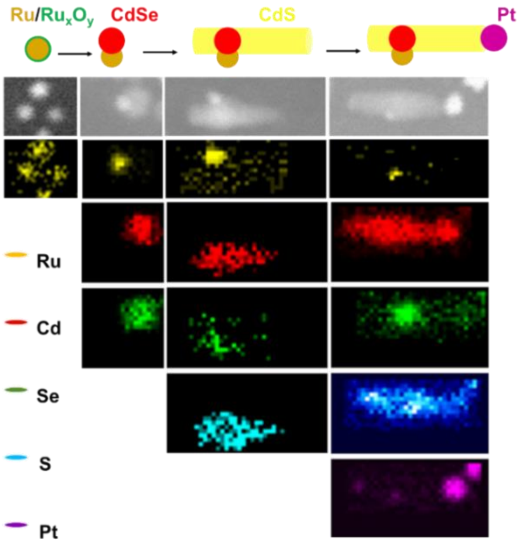

Figure 2.27. Elemental confirmation of each component in Ru-CdSe@CdS-Pt using EDS

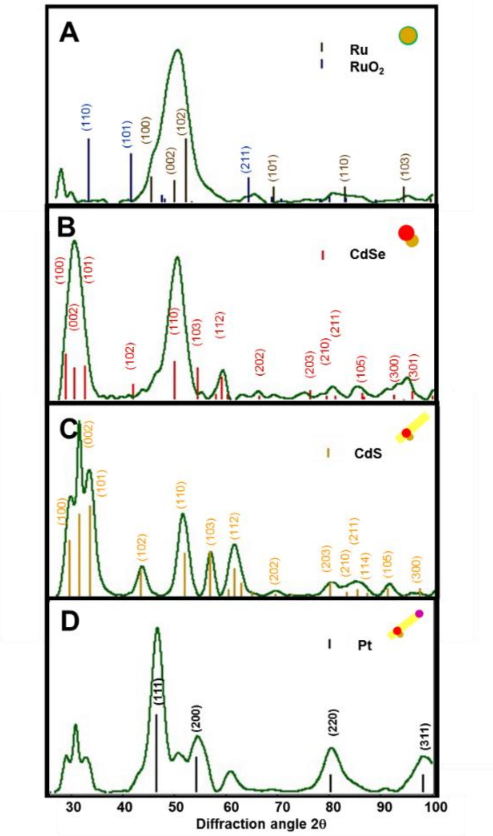

Figure 2.28. XRD of (a) Ru@Ru$_x$O$_y$ (b) Ru-CdSe (c) Ru-CdSe@CdS (d) Ru-CdSe@CdS-Pt

2.2 Photocatalytic Applications of Ru-CdSe@CdS-Pt heterostructures

2.2.1 Applications in Solar Water Splitting.

Photocatalytic studies of Ru-CdSe@CdS-Pt nanoparticles were carried out using procedures reported by Amirav [54]. Briefly, after using 11-mercaptoundecanoic acid (MUA) to water solubilize Ru-CdSe@CdS-Pt nanoparticles, they were loaded into a gas tight reaction cell without scavengers of any kind in solution. The solution was left under 420 nm irradiation for almost 11 days, checking for H_2 evolution throughout using a GC equipped with a thermal conductivity detector. No H_2 was detected throughout the experiments, but a TEM of the final product revealed some particles survived the long reaction (Figure 2.29). This suggests some measure of enhanced stability was attained, though there was no sign of oxygen evolution and only trace amounts of hydrogen were detected. It is quite likely that the photogenerated h^+ do not have enough energy to drive water oxidation or the charge carriers were lost to alternative transfer processes.

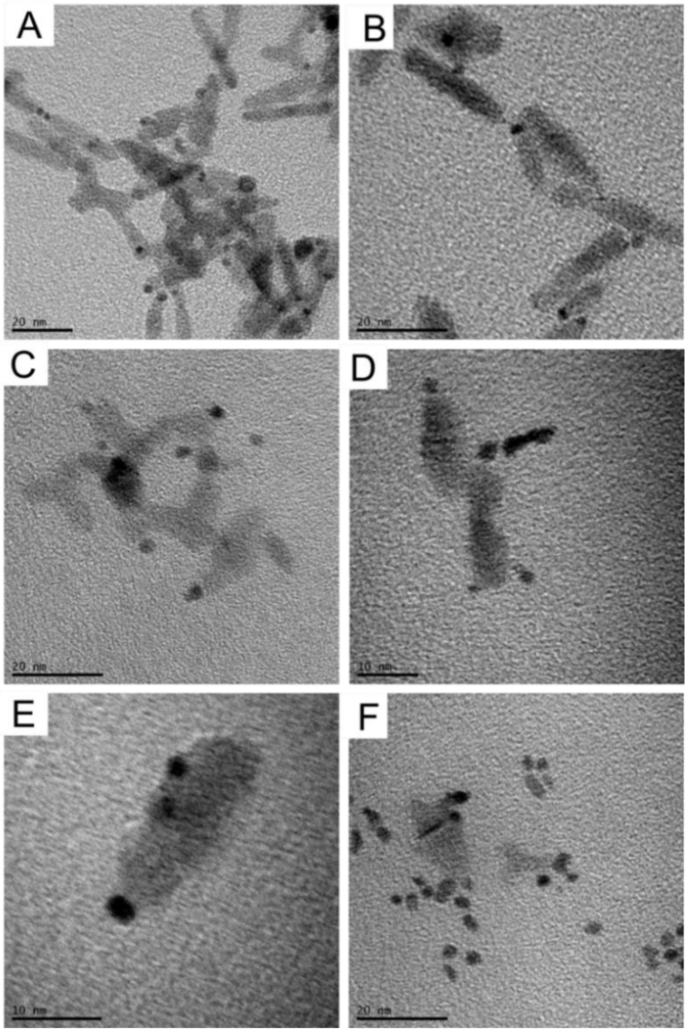

Figure 2.29. TEM after 11 days of irradiation of Ru-CdSe@CdS-Pt

2.2.2 Hole transfer to Ferrocyanide/Ferricyanide system

A 100 mM stock solution of potassium ferrocyanide, $K_4Fe(CN)_6.3H_2O$, was prepared in water, along with a 10 mM potassium borate (KBi) buffer solution at pH 9.2. Ligand exchange of Ru-CdSe@CdS-Pt nanoparticles with MUA was performed using a procedure reported in reference 29 of Banin's protocol [82] (faster than Amirav's procedure). The same ligand exchange was done on Ru-CdSe@CdS nanorods and both nanorod samples were then redispersed in a 1-10 mM KBi buffered solution of 1-10 mM $K_4Fe(CN)_6.3H_2O$. The target optical density for each sample was less than 0.5 at 420 nm after stirring the mixture in the dark, prior to initiating the reaction.

$$[Fe(CN)_6]^{4-} \Leftrightarrow [Fe(CN)_6]^{3-} + e^- \qquad (2.5)$$

The ferrocyanide/Ferricyanide system, $Fe(CN)_6^{4-}$/ $Fe(CN)_6^{3-}$ is a one electron, electrochemically reversible redox couple in which the Fe^{2+} centre is oxidized to an Fe^{3+} state upon h^+ transfer (Equation 2.5) [81]. It has been shown to be an effective electron transfer mediator in Z-scheme water splitting systems [83]–[85]. Initial attempts were made to study the effectiveness of this mediator using Ru-CdSe@CdS and Ru-CdSe@CdS-Pt nanorods. The production of Ferricyanide was tracked by measuring the difference in the onset of absorption at 420 nm, *in-situ*, once the sample was exposed to light (Figure 2.30). Over time, the concentration of the Ferricyanide produced increased, but not without any degradation to the chalcogenide. TEM micrographs reveal partial degradation of the nanorods occurred (Figure 2.31), with some nanorods retaining either Pt or Ru. This suggests using this redox couple to monitor hole transfer to an inorganic molecule in solution has great potential. This may also be applicable in integrating this II-VI system into a Z-scheme water splitting system.

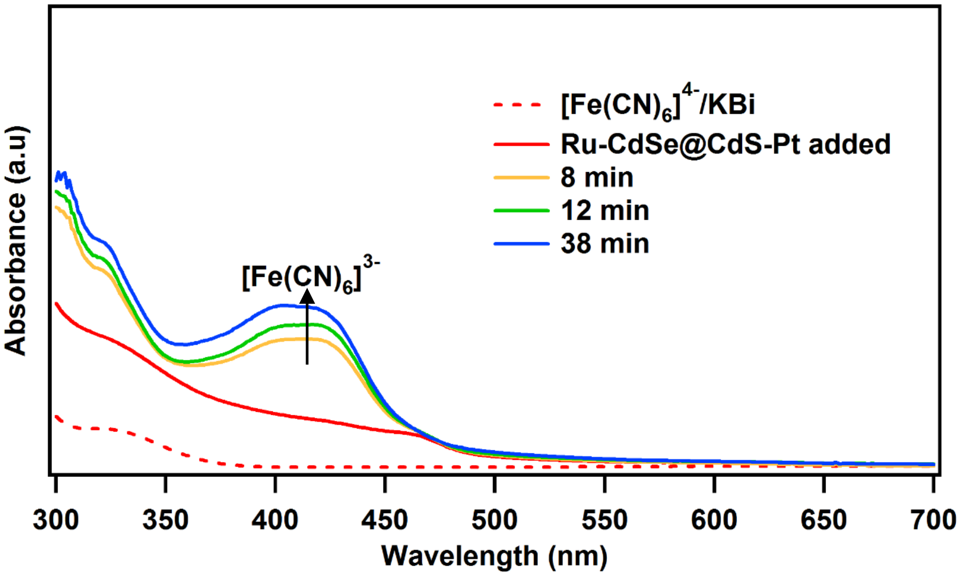

Figure 2.30. Representative *in-situ* UV-VIS showing growth of Ferricyanide at 420 nm. The extinction coefficient for Ferricyanide was determined to be 1062.9 $cm^{-1}M^{-1}$ at 420 nm.

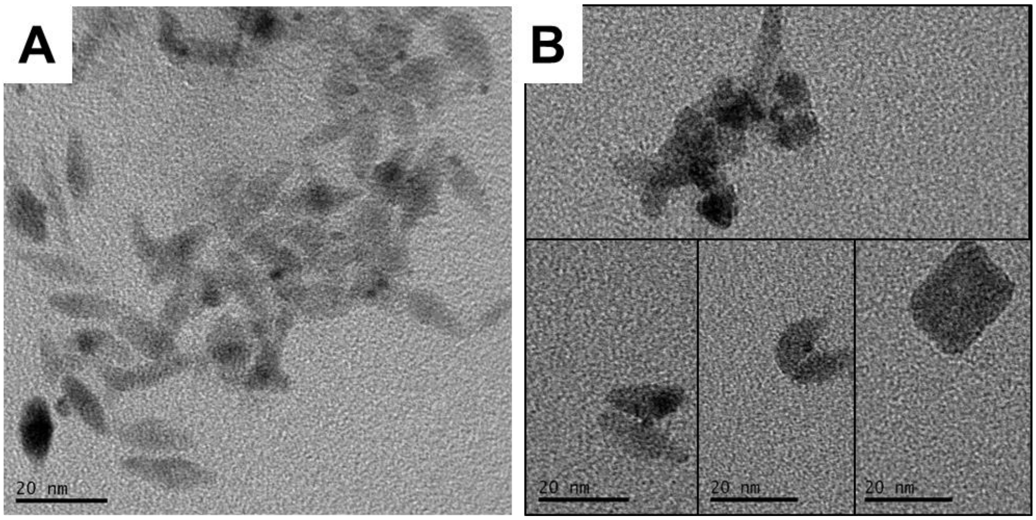

Figure 2.31. TEM after Ferricyanide production using (A) Ru-CdSe@CdS-Pt and (B) Ru-CdSe@CdS nanorods

2.3 Substitution of Ru@Ru$_x$O$_y$ with non-precious metal oxidation catalysts

Since Ru is a noble metal, it is of interest to replace the water oxidation catalyst with an abundant, cheaper non-precious metal. Thus, replacing Ru with two alternative water oxidation catalysts was briefly investigated. A summary of initial efforts using iron oxide and cobalt oxide is presented in this section. In the case of Co_3O_4-CdSe, a type II band alignment already exists, so this system is particularly interesting as it can potentially be used for photochemical oxidation reactions. This would be a simpler way to see if h^+ can be funnelled out of the CdSe and into an adjacent metal oxide.

2.3.1 Chemicals

Iron (III) acetylacetonate, HDD, cadmium acetylacetonate, TOPO, Se powder, tributylphosphine, OLAm, OAc, dioctyl ether (OE), toluene, acetone, octylamine, chloroform, ODPA, TOP.

2.3.2 Synthesis of γFe_2O_3-CdSe heterostructures

Fe_2O_3-CdSe heterostructures were synthesized using a procedure developed by Shim [86] with modifications. A mixture of 1.48 mmol Fe(acac)$_3$, 7.4 mmol HDD, 4.44 mmol OLAm and 4.44 mmol OAc, in 14.8 mL OE was vacuumed for 1 hour at 100 ^{0}C. It was then heated to 200 ^{0}C under Ar for 2 hours (color changed from brown to black) and the temperature raised to 270 ^{0}C for one hour. After reducing the temperature to 100 ^{0}C, 20 mg Se dispersed in 0.5 mL OE was injected and the temperature reset to 80 ^{0}C. Separately, a cadmium precursor solution formed from a one hour degas of 0.123 mmol Cd(acac)$_2$, 300 mg HDD, 400 mg TOPO and 1 ml OE at 100 ^{0}C was made. This Cd solution was added drop wise to the Fe-Se solution over 6.5 minutes and stirred for 10 additional minutes. The reaction mixture was then heated to 270 ^{0}C for one hour and quenched with 10-12 mL toluene at 90 ^{0}C. A 1:1 v/v addition of acetone was used to precipitate the nanoparticles after centrifuging at 9500 rpm for 15 minutes. To the pellet, 7.5 mL chloroform and

2.5 mL octylamine was used to redissolve the pellet, followed by a 1:1 v/v addition of acetone. To the supernatant, 25 mL acetone was added. Both portions were centrifuged and the nanoparticles collected after an additional wash.

The ratio of precursors was also modified for Fe:Cd (6:1 instead of 12:1), Cd:Se (1:1 instead of 1:2) and Se/TBP complex substituted for Se powder.

This protocol was initially developed for overgrowth of CdS (yield of 51 % γFe_2O_3-CdSe dimers), which has a lattice mismatch of 4.6 % with the γFe_2O_3. This mismatch is much higher in the case of CdSe deposition, so may account for the extremely low yields of γFe_2O_3-CdSe heterostructures (Figure 2.32). In the mechanism proposed by Shim, preformed seeds should form an intermediate aggregated phase where the seeds are wetted by Se, followed by Cd precursors. In the subsequent annealing, γFe_2O_3-CdSe heterostructures should form. Aliquots taken during this synthesis however do not show wetting of the γFe_2O_3 with Se prior to addition of the Cd precursor. A different CdSe deposition method might prove more successful [87].

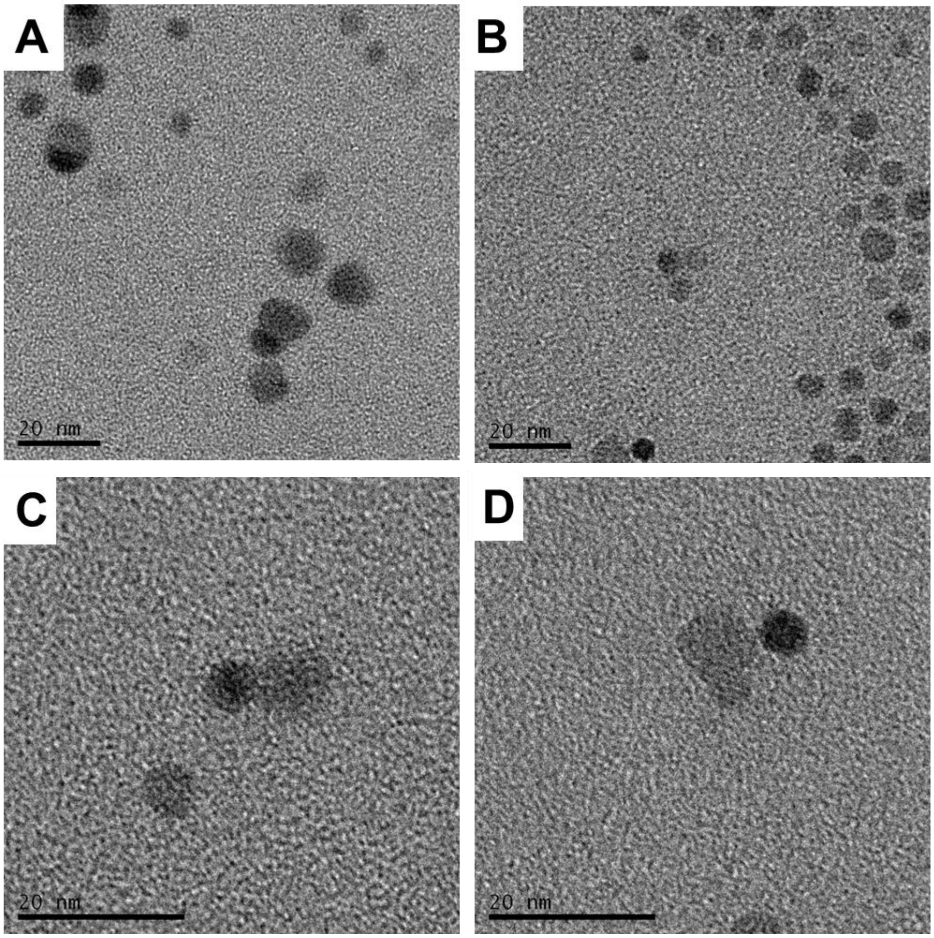

Figure 2.32. (A-D) TEM of Fe_2O_3/CdSe heterostructures

2.3.3 Synthesis of Co_3O_4-CdSe heterostructures

Co_3O_4 was synthesized as described by Frei [88] and redispersed in ethanol to form a 4.3 mg/mL solution (ethanol was evaporated from the seeds prior to use). An attempt to synthesize Co_3O_4-CdSe heterostructures was made using two approaches based on the Ru-CdSe synthesis developed. First, a cadmium oleate solution was formed in the same way as that formed during the Ru-CdSe synthesis, except the Co_3O_4 seeds were added prior to complexation. All other steps were held the same and no R-PhAcids were used. In the second approach, Co_3O_4-CdSe heterostructures were synthesized using the same procedure as for Ru-CdSe, except the Co_3O_4 seed injection solution was not filtered prior to use and no R-PhAcids were added at the end of the reaction. Aliquots were taken at 70 seconds and 150 seconds. All samples were purified as previously described for Ru-CdSe nanoparticles. For the first approach, a purplish solution was recovered in the supernatant, while a reddish supernatant was recovered for the second approach.

The R-PhAcid ligand system was also explored as an alternative to the OAc/OLAm system used in the Ru-CdSe growth. Briefly, 65 mg of CdO, 280 mg ODPA and 3 g TOPO was degassed for one hour at 100 ^{0}C. After formation of a Cd-ODPA complex at 320 ^{0}C, a Co_3O_4:TOP mixture was injected, followed by a quick injection of a 360 mg TOP and 60 mg Se solution at 340 ^{0}C. After 2 minutes from injecting the seeds, the solution turned to a deep navy blue solution before TOP:Se could be introduced.

In each case, complete or partial Co_3O_4 dissolution from the dimer is thought to have occurred. In the TOP:Se case, a blue solution gradually formed within seconds of injecting the Co_3O_4 seeds. This color has been noted in cases where decomposition of a Co precursor did not lead to any separable crystalline product and was seen in the early stages of Co nanoparticle growth, where the solution color changed from blue to black over time. In the OAc/OLAm cases, a similar process is suspected. All TEM for these conditions indicate a reduction in the presence and size of Co_3O_4 seeds, with homogenous CdSe nanoparticles predominantly seen (Figure 2.33). Thus, like the case with Ru, the oxide seed is not stable under the CdSe deposition process, resulting in low yields of Co_3O_4-CdSe heterostructures (Figure 2.33).

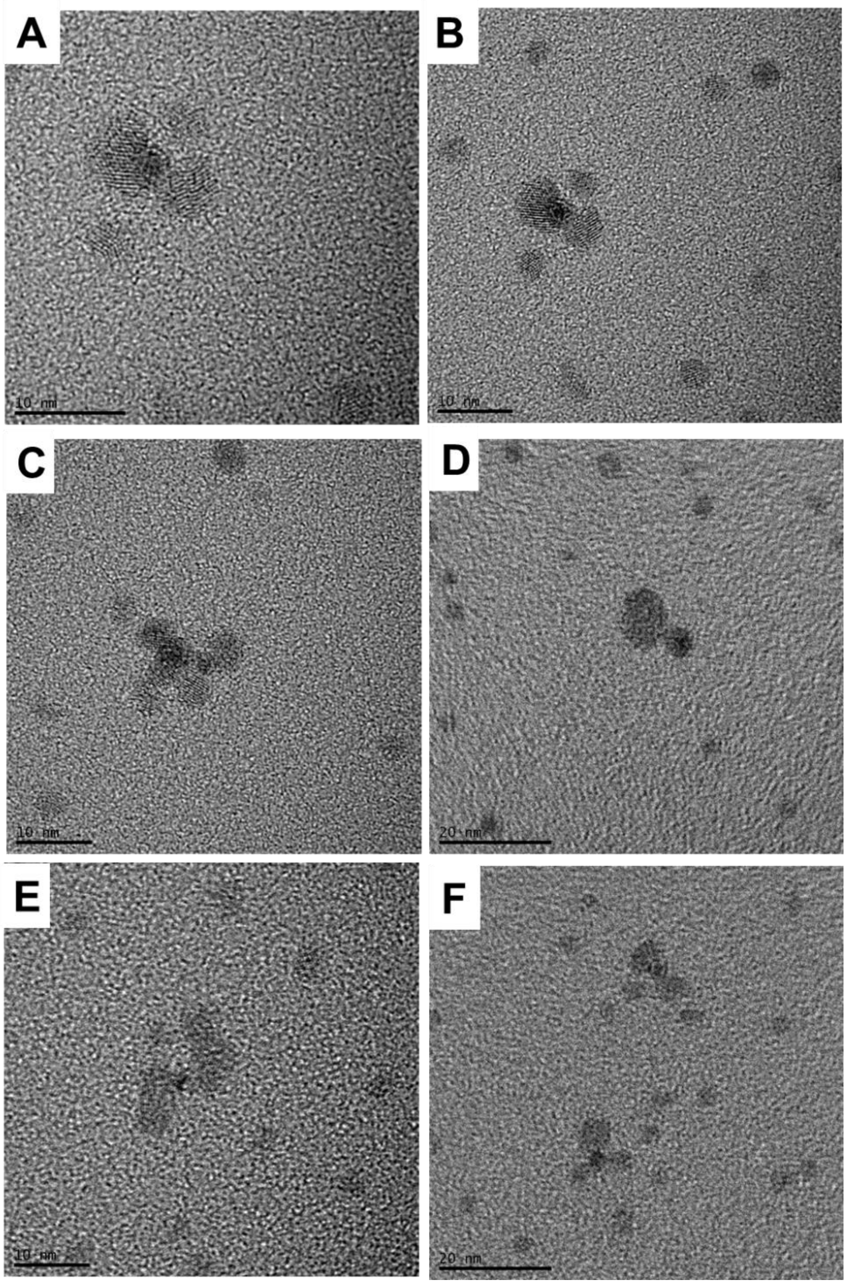

Figure 2.33. (A-D) TEM of Co_3O_4-CdSe heterostructures

2.4. Conclusions

When using sequential colloidal deposition techniques to construct multicomponent nanoparticles, special attention must be given to possible ligand induced degradation of individual components. This parameter is key to achieving high yields of complex nanoheterostructures with controlled placement of its individual components while maintaining their respective composition and morphology. The Ru-CdSe@CdS-Pt system is not perfect, and has room for improvements in the yield of the final architecture. One potential solution to eliminating the need for additional free R-PhAcids in the CdS nanorod growth is to use a chalcogenide precursor that leads to anisotropic CdS growth based on its reaction with a Cd-ODPA complex. Guo [89], [90] reported dichalcogenide molecular precursors which tailor the nucleation and growth kinetics and produce II-VI nanoparticles with morphologies ranging from dots to rods to tetrapods. This could be an alternative way to approach the CdS growth while addressing the stability of the Ru-CdSe dimer under experimental conditions.

While initial hydrogen evolution studies on Ru-CdSe@CdS-Pt were inconclusive, this structure did not fully corrode in water under prolonged irradiation in the absence of h^+ scavengers. Thus, it would be interesting to study different combinations of the individual components for studying oxidation and reductive reactions separately, to understand the charge transfer kinetics across the different interfaces. Its integration into Z-schemes would provide a wealth of information regarding the oxidative and reductive half reactions. Furthermore, other systems besides water splitting can be exploited to develop this understanding. The successful placement of Ru at the CdSe seed in Ru-CdSe@CdS was a formidable synthetic challenge which opened the door to exploring photochemical oxidative reactions on a system which on its own, would normally degrade without the use of fast h^+ scavengers.

Chapter 3. Metal Nanocrystals: Fundamentals, Synthesis Applications in Heterogeneous Catalysis

3.1 Metal nanocrystals

3.1.1 History and Introduction

Metal nanocrystals can be either mono-metallic or multi-metallic, where the composition includes two or more metallic elements. Use of these nanocrystals dates back many centuries, initially due to their tunable optical properties. Whether it was fully understood then or not, colored glass developed by the Romans were stained using alloy nanocrystals. One famous example is the Lycurgus Cup, a fourth century dichroic glass cup stained with Ag-Au nanoparticles, which changes color when light passes through it [91]. Lustre, a thin metallic film which includes Ag, Cu and iron oxide applied under reducing conditions on a glazed ceramic, was a technique used during the Renaissance period to decorate majolica (glazed pottery). Later studies on majolica produced with this technique revealed the presence of Ag and Cu nano-clusters [92].

It was not until 1857 when Michael Faraday identified finely divided metal particles as the source of color in metal colloids that these metal nanocrystals' existence was confirmed [93]. In 1908, Mie [94] followed up with work that showed the colors of these colloids were due to light absorption in the visible region due to plasmons, resonant collective oscillations of conduction electrons. Nowadays, metal nanocrystals have amassed a major track record as interesting materials for catalytic [95], [96], optical [97], [98], biomedical [99] and magnetic [100] applications due to the novel physicochemical properties which arise from quantum confinement effects (Figure 3.1) [101]. They thus exhibit size dependent characteristics such as melting point depressions (scales inversely proportionally to the particle radius) and absorption frequency.

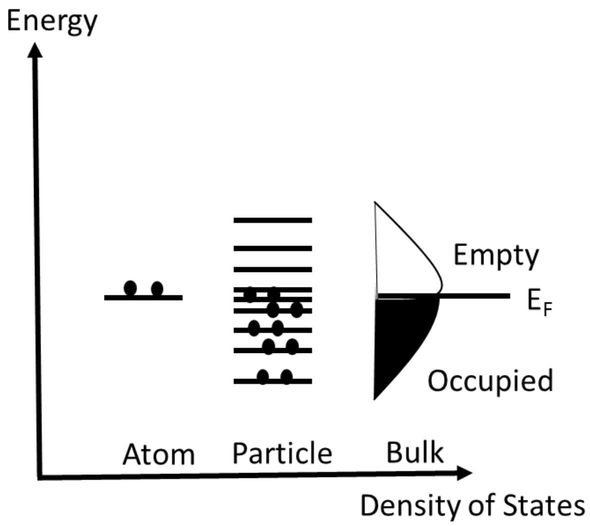

Figure 3.1 Change in electronic energy states as bulk metal transitions to nano-sized crystal

The atomic arrangement (random or ordered intermetallic) in a multi-metallic nanoparticle can directly impact its catalytic performance through a combination of electronic and geometric effects

[12], [102]–[105]. Dilution of the surface of a monometallic nanocrystals with another metal reduces the size of the original monometallic ensembles. This commonly called ‘ensemble’ or ‘geometric’ effect can affect the activity of reactions that call for large ensembles. If large ensembles constitute the active site, then dilution of the ensembles results in lower activity. However, if the reaction only requires a single site, then the activity is only moderately affected. ‘Ligand’ or ‘electronic’ effects refer to changes in the chemical properties of the material at the surface due to alloying. These also have an effect on the catalytic performance, as it can modify the binding strength to different surface adsorbate species.

Researchers have correlated the activity of different reactions to the d-band center of a metal, where a shift in the d band center of the metal away from the Fermi level results in weaker adsorption of surface species [103], [106], [107]. The Sabatier principle examines the correlation between a catalytic reaction rate and the adsorption energy of a reactant or intermediate [108]. A plot of this reaction rate vs adsorption energy produces a volcano plot, so termed because of its shape. The optimal catalyst, found at or near the center of a volcano plot, will have the best balance between the activation rate of reactant adsorbate species and desorption of product molecules. This is a very useful and preliminary way to predict and screen potential catalysts for a targeted catalytic reaction. If the adsorption of a reactant species is too weak, then no reaction occurs because of the absence of surface bound reactants. If the product or intermediate is bound too tightly, it can permanently block all active sites on the surface, leading to a loss of catalytic activity. This effectively poisons the catalyst surface.

Heterogeneous catalysis is at the forefront of many industrial reactions today. They often take advantage of the large surface area and novel physicochemical properties present in metal nanoparticles. Alloys generally have distinct binding affinities with different reactants, in contrast to their monometallic counterparts. This allows for tunability over the bonding between the catalyst surface and reactant, thereby stabilizing or destabilizing products and/or intermediates and maximizing selectivity to a preferred product. Manipulation of the size and shape of nanocrystals can translate into facet and size dependent chemistry [109]. Furthermore, metal nanocrystals can be dispersed onto a supporting material, enhancing these desirable characteristics through synergistic effects and allowing for the development of bi-functional catalysts [110]. While the synthesis of monometallic nanocrystals has become quite sophisticated [97], the synthesis of alloys composed of metals with very different electronegativity (noble metal plus non-precious metal) has room for improvement.

3.1.2 Challenges of Bimetallic Alloy Nanocrystal Synthesis

A variety of bimetallic architectures have been reported as alloy, porous, hollow or heterostructures such as dimers, core-shell and dendrites [95], [111]. Variation of the reductant, concentration of precursor or its injection rate has been used to tune the reaction kinetics to obtain different structures. E.g. Xia reported that Pd-Ag dimers result from a slow injection of Ag precursor, but evolve to eccentric particles with selective deposition of Ag on Pd facets at moderate injection rates, and finally core-shell Pd-Ag at high injection rates [112]. In general, alloys can be synthesized by either using a strong reducing agent that will simultaneously co-reduce all [113] metal precursor, or first tuning the redox potential of the metals using appropriate ligands to modulate the reactivity [114]–[116]. Otherwise, different heterostructures might result as opposed to alloy formation if one element reduces much earlier. They have also been synthesized using ion sputtering, laser ablation/vaporization**,** gas-phase reactions involving organometallic precursor vapors or electrochemically [95], [96]. Thermal decomposition routes have also been explored [117] .

The degree of mixing and extent of chemical ordering in bimetallic alloys, denoted M-N, depends on the relative strengths of the M-M, N-N and M-N bonds, surface energies of the bulk monometallic counterparts, relative atomic sizes, charge transfer, electronic or magnetic effects and surface-ligand binding strength. These parameters are discussed in a detailed review on nanoalloys by Johnston [100]. M-N mixing is favored in the case where the M-N bond strength is highest, leaving the metal with the strongest homonuclear bonds at the nanocrystal core. Segregation of an element to the surface can occur when it has the lowest surface energy or is strongly bound to ligands used in surface passivation. Furthermore, smaller atoms preferentially occupy the core, which is more sterically confined and can experience compressive strain. Mixing of M-N is favored when charge transfer from the less to more electronegative element occurs. Electron spin interactions and the electronic shell structure may also stabilize a certain size or composition.

While several synthetic protocols have been developed for the preparation of alloy nanocrystals, the simultaneous achievement of homogeneous composition and size remains a challenge for many alloy systems. The size and structure dependent catalytic activity of alloy nanocrystals means careful thought should be given to how they are synthesized. In practice, the majority of existing supported alloy nanocrystals are synthesized using impregnation or co-reduction techniques. These techniques often result in alloy nanocrystals with dimensional, compositional and structural inhomogeneity, making it difficult to elucidate the catalyst's structure-activity relationship [118]–[120]. Furthermore, it is often difficult to extract these differences due to particle inhomogeneity. Colloidal nanoparticle synthesis provides an advantage over conventional methods of catalyst preparation in that it may allow for the tailored control of the composition of bimetallic nanoparticles. While structural changes are expected under experimental conditions, these changes can be mapped from a well characterized initial state of known composition.

Large differences in the reduction potentials of the individual elements make co-nucleation in a desired ratio difficult. As the difference in the reduction rate of individual components increases, simultaneous co-nucleation becomes more difficult. If one element is reduced faster than the other, core/shell or distinct monometallic nanoparticles may form. Thus, synthetic parameters should be chosen such that the reaction is mainly diffusion limited. If the reduction rate is determined primarily by the rate of mixing of the reactants, rather than the electron transfer kinetics, this issue of co-nucleation can be addressed. Strong reducing agents would also be required to achieve the simultaneous co-reduction necessary to control the nucleation and growth kinetics with different metal precursors.

Colloidal synthesis of intermetallic nanoparticles composed of at least one non-precious metal component with a negative reduction potential has been reported, such as Pt-Zn [121], Pt-V [113], Pt-Ti [113] and Pt-Pb [122]. Non-agglomerated intermetallic nanoparticles are desirable for easy post-synthetic surface treatments and subsequent deposition of other materials. Many reports indicate formation of intermetallic structures only after thermal annealing of as-synthesized alloy nanocrystals at elevated temperatures. However, this can cause sintering and catalyst deactivation due to loss of active metal sites. This, coupled with the difficulty in achieving co-nucleation, has made synthetic protocols of intermetallic nanoparticles of different sizes and composition quite challenging. Olesiak has reported the colloidal synthesis of various Pt-Sn intermetallic nanoparticles [123], [124] while Kovalenko has developed a general procedure to producing alloys of non-precious metals (e.g. Cu-Sn, Cu-Sb, Bi-Sb) [117], [125]. Work by Skrabalak [114]–[116] has shown that the local ligand environment plays a role in the nucleation of bimetallic nanocrystals and their final architecture. Their protocols are relatively simple and the principles therein can be adopted and modified for other systems.

3.1.3 Deactivation in Metal Nanoparticle Catalysts

Nanocrystals are inherently unstable under many industrially relevant conditions. Surface reconstruction or phase segregation is known to occur when nanoparticles are exposed to different gaseous environments. This reactant gas induced segregation has been observed in the Rh-Pd system [126], where surface energies dictate the surface composition. Furthermore, nanocrystals may also sinter and grow into larger crystals at high temperatures, where this reduction in surface area leads to rapid catalyst deactivation over time. Use of a ligand shell around the nanocrystals is not always a viable solution, as these capping agents (organic) may either decompose at temperatures exceeding 300 ^{0}C or block active metal sites if not removed prior to the reaction. General approaches to improving the stability of metal nanocrystals include alloying with a higher melting point element and anchoring the particle onto a supporting material, thereby restricting migration of atomic and/or crystallite species [127].

Li developed an atomistic theory describing Ostwald ripening of metal nanocrystals anchored on a support in the presence of reactant molecules based on Rh/TiO_2 system under CO [128]. He proposed that strong reactant-metal adatom bonding on the support is critical for formation of a metal-reactant complex. For exothermic adsorption, this complex is the dominant monomer, as opposed to metal adatoms. Ostwald Ripening is favored when the total activation energy of such complexes is less than the metal adatoms without any reactants. Furthermore, metal nanocrystals will disintegrate into reactant-adatom complexes when the complexation is exothermic versus the supported metal nanocrystal. Thus, suppression of Ostwald ripening would occur for supports that provide a higher total activation energy of both the adatoms and complexes. Disintegration and redispersion of sintered catalyst would occur for an exothermic Gibbs free energy of disintegration, which can be modulated by careful selection of reactant gases under controlled conditions.

Prior work has shown core/shell nanocrystal catalysts are beneficial for improving their thermal stability at high temperatures. Porous metal oxide coatings can provide a physical barrier between individual nanoparticles, thereby hindering sintering in comparison to bare, uncoated nanoparticles. A thermally stable, model catalytic system consisting of a Pt metal core encapsulated by a mesoporous silica shell (Pt@mSiO_2) was reported by Somorjai, exhibiting thermal stability up to 750 °C in air [129]. The Pt surface was still accessible through the silica and as catalytically active as bare Pt metal for ethylene hydrogenation and CO oxidation. When these structures were also tested in n-hexane reforming [130] and cyclohexane decomposition [131], enhanced thermal stability was also evident. Pd nanoparticles coated with alumina via atomic layer deposition resisted sintering at high temperatures for ethane dehydrogenation [132]. Propane dehydrogenation was chosen as the catalytic reaction of interest and is discussed in the following section.

3.2. Propane Dehydrogenation: An Industrially Relevant Reaction

3.2.1 Overview of Propane Dehydrogenation

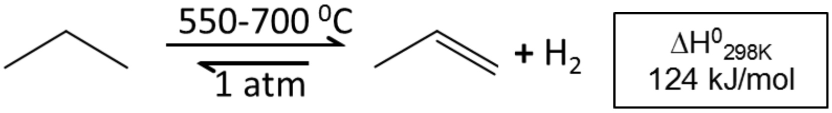

(3.1)

Scheme 3.1. Propane Dehydrogenation reaction

One of the most important industrial petrochemical building blocks is propene, with over 50% of it used in polypropylene for plastics [133], [134]. Ever increasing propene demands have outgrown the classical routes of propene production, which include steam cracking and fluid catalytic cracking. These routes produce propene as a byproduct, so recent attention has been given towards increasing on-purpose propene production routes. This has especially been fueled by the onset of shale gas exploitation, which for the United States, translates into a feedstock advantage. The shift of feedstock used in naphtha fed steam-crackers to ethane further serves as an impetus to commercializing on-purpose technologies. Propane dehydrogenation has become more and more attractive with the abundance of cheap propane.

Propane dehydrogenation (PDH) is a highly endothermic, equilibrium-limited reaction (Equation 3.1). High temperatures and low pressures are required to drive appreciable conversion; propane feeds may be diluted with inert gases (e.g. N_2, steam) or the H_2 produced combusted to make the overall reaction exothermic [133]. Oxidative dehydrogenation routes face the challenge of minimizing consecutive oxidations to unwanted oxygenate by-products. At these high operating temperatures, the catalyst is susceptible to deactivation via coking and sintering. Chromia [135] or platinum loaded onto alumina are traditional catalysts used in the propane dehydrogenation industry. In a typical PDH process, the catalyst first undergoes a pretreatment in an oxidizing or reducing atmosphere prior to dehydrogenation. Thereafter, the catalyst must be regenerated to remove carbon build up from the surface before undergoing another pretreatment and dehydrogenation cycle.

Pure Pt, while very active for alkane dehydrogenation, suffers from rapid deactivation due to coking and low olefin selectivity [133]. Promoters, or secondary metal components (Figure 3.2) introduced via alloying, are thought to facilitate the transfer of coke precursors to the support, thereby freeing active metal sites and slowing down the deactivation rate. Cracking and polymerization reactions produce graphitic and polycyclic aromatic carbon layers that block active metal sites. Furthermore, promoters can improve the olefin selectivity through a combination of ligand and geometric effects. There have been many reports that validate the use of alloys for PDH. The Pt-Sn system is well studied and gives good insight on how alloys are beneficial for PDH

[120], [136], [137]. Chen performed density functional theory calculations investigating the effect of Sn on the PDH activity and selectivity [106]. He showed that higher Sn contents lead to a downward shift in the d-band center, lowering the bonding strength of propyl and propene on the surface. This corresponded to a decrease in the energy barrier to propene desorption and simultaneous rise in activation energy for propene dehydrogenation. Pt-Sn alloy surfaces thus had improved propene selectivity (at the expense of the catalytic activity) over pure Pt, which favored propene dehydrogenation.

In this work, particular attention was paid to the use of Ga, a promising but infrequently studied [138]–[141] promoter that has a standard reduction potential of -0.592 V and a Pauling electronegativity of 1.81 (Figure 3.2). One noted benefit of Ga is the recombinative desorption of hydrogen adatoms as H_2 [142], [143], which inhibits undesired side reactions such as cracking.

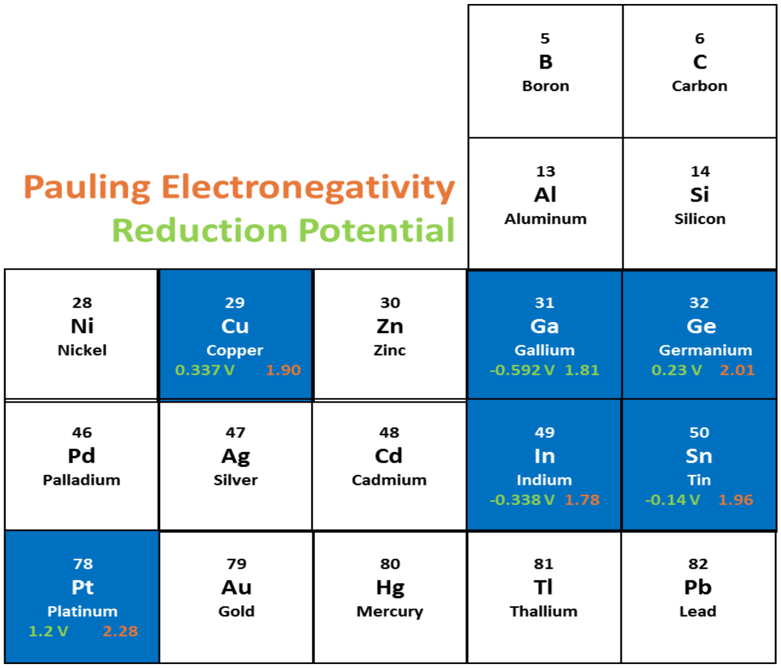

Figure 3.2. Promoters of interest as a Pt alloy catalyst for PDH. The standard reduction potential and Pauling electronegativity are provided for comparison.

3.2.2 Overcoming Challenges Encountered in Propane Dehydrogenation

One commercial technology for propane dehydrogenation is the Oleflex process [144], developed by UOP. In this process, catalyst (Pt-Sn on K modified γ-Al_2O_3) must be regenerated every few days due to deactivation from coking. Typically, the catalyst is heated in air with a flow of hydrogen chlorine to aid in Pt redispersion. Subsequent activity is diminished with each successive cycle due to sintering. As previously mentioned, the use of promoters in an alloy can reduce the effect of coking. Furthermore, encapsulation of the catalyst in a porous oxide shell can improve the thermal stability and prevent sintering. Thus, this work seeks to combine these advantages into a single system comprised of Pt-Ga alloy core nanoparticles encapsulated within a porous oxide shell (Figure 3.3).

Part two of this thesis explores the role of Ga precursor reactivity in the final composition of alloy platinum-gallium (Pt-Ga) nanoparticles and gives insight into structural changes that occur under different gaseous environments. Four Ga precursors were used: gallium chloride, acetylacetonate, bis(trimethylsilyl)amide and dimethylamino gallium. The Pt precursor of choice was platinum acetylacetonate. The effect of two reducing agents of different reducing powers was also tested. It serves to inform the reader of the compositional inhomogeneity often present in bimetallic nanocrystal synthesis and the challenges associated with developing novel alloy systems comprised of a non-precious metal. The long term overall goal of this work is to develop thermally stable Pt-Ga nanoparticle cores encapsulated within a porous metal oxide shell for applications in propane dehydrogenation. Initial results are shown for the PDH activity over bare but supported Pt-Ga alloys.

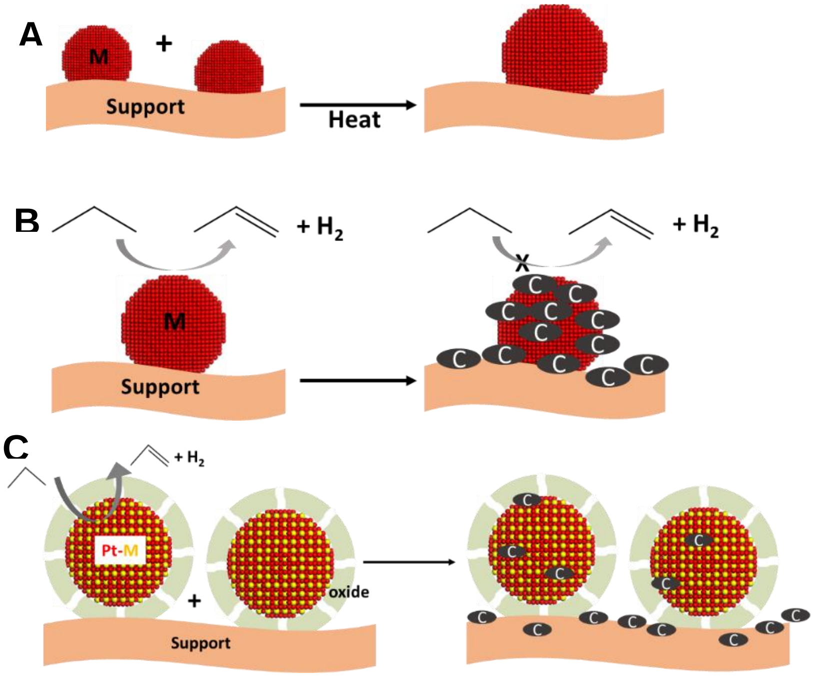

Figure 3.3. (A) Sintering in bare metallic nanoparticles (B) Coking of monometallic catalyst (C) Core-shell bimetallic alloys encapsulated within a porous oxide shell resist sintering and hinder coke build up on catalyst surface

3.3.3. Developing a Pt-Ga Alloy Synthetic Protocol

A variety of synthetic procedures was first tested to determine the best approach toward synthesizing Pt-M nanoparticles, starting with Pt-Sn as a model system. While the synthesis of Pt-Sn bimetallic nanocrystals directly onto a support has been widely reported [145]–[148], general routes to structurally controlled colloidal synthesis of unsupported Pt-Sn nanoparticles have been limited. Thermal decomposition of Pt and Sn precursors often lead to a variety of Pt-Sn phases. Injection of one precursor solution into a hot solution of the other metal precursor led to the same issue, with massive uncontrolled aggregation occurring. Solution mediated interconversion of PtSn to Pt_3Sn and $PtSn_2$ intermetallics has also been reported [149]**.** However, these nanoparticles suffered from an extremely broad size distribution of 10-100 nm and poor uniformity from massive aggregation and sintering. Other works have reported the synthesis of PtSn nanoparticles, PtSn@Pt core/shell structures and sub 10 nm Pt_3Sn nanoparticles [148], [150], [151].

Olesiak's procedure [123] based on the gradual co-reduction of precursors slowly injected into a hot solution was chosen for further optimization. PtSn and Pt_3Sn intermetallic nanoparticles were successfully reproduced using his procedure, with some modifications (Appendix A1). Olesiak reported the first shape controlled colloidal synthesis of Pt-Sn intermetallic nanoparticles using a versatile hot injection method and mild reducing agent. High injection temperatures (300 ^{0}C) were found to affect the formation of shape controlled Pt-Sn intermetallics, while the bimetallic composition affected the morphology. One key modification to this recipe was the solvent chosen to disperse the metal precursor. Benzyl ether was chosen instead of 1-octadecene because of the higher solubility across a variety of metal precursors.

Thus far, to the best of my knowledge, no protocol exists for the synthesis of unsupported Pt-Ga nanoparticles. As previously mentioned, Bell, Marin and Weckhuysen [138]–[141] have studied the catalytic activity of Pt-Ga catalysts which were synthesized using conventional impregnation techniques. The novel colloidal synthesis of Pt-Ga nanoparticles is discussed in the following chapter 4. What impact does manipulating the local ligand environment in metal complexes have on the reduction kinetics? How might this in turn affect the final architecture of the bimetallic nanocrystals? Might the final architecture be composition dependent for specific Ga precursors? Such questions were considered when selecting Ga precursor candidates.

Chapter 4. Synthesis of Pt-Ga Nanoparticles for Propane Dehydrogenation

4.1 Chemicals, Materials and Equipment

Benzyl ether, 90% 1,2-hexadecanediol, platinum acetylacetonate, gallium acetylacetonate, anhydrous gallium trichloride, anhydrous bis(μ-dimethyl amino)tetrakis(dimethyl amino)digallium, 1.6 M n-butyl lithium (nBuLi), lithium bis(trimethylsilyl)amide, anhydrous diethyl ether, hexamethyldisilazane, gallium tris(trimethylsilyl)amide, 90% oleic acid, 90% oleylamine, 90% 1-octadecene, hexane, ethanol, octylamine, dioctylamine, trimethylamine N-oxide, chloroform, tin acetylacetonate. Benzyl ether, dioctylamine and octadecene were dried under vacuum separately using standard schlenk line techniques for 90 minutes at 150 ^{0}C.

Pt_3Ga, Pt_2Ga, PtGa and $PtGa_2$ were chosen as potential candidates for applications in PDH as the Pt-Ga phase diagram suggests they are stable at the high temperatures required (Appendix A2.1).

Nanoparticles and Ga precursors were characterized using a combination of electrochemical and x-ray based techniques. These are described in detail later on. XRD patterns were taken on a Bruker GADDS Hi-Start D8 diffractometer with a Co anode at 45 kV/35 mA (λ=1.79 A).

4.2 Synthesis of Ga Precursors and Li- Reductant

4.2.1 Synthesis of lithium bis (trimethylsilyl) amide

$$[(\mathrm{CH_3})_3\mathrm{Si}]_2\mathrm{NH} + \mathrm{nBuLi} \rightarrow \mathrm{LiN}[(\mathrm{CH_3})_3\mathrm{Si}]_2 + \mathrm{BuH}$$

Hexamethyldisilazane (80.4 mmol) was added to a dry schlenk flask in the glove box. It was then placed in an ice bath and stirred moderately, and n-butyl lithium (50.24 mL) slowly added to the cold solution, which stays colorless. (Note: Since nBuLi is pyrophoric, appropriate cannula transfer techniques under Argon should be used. All apparatus should be quenched with anhydrous methanol prior to exposure to air). After one hour of stirring, the mixture was removed (by now, a white precipitate should be seen) and warmed to room temperature, at which point the solution became colorless. The solution was evacuated to isolate dry powder, which was collected in the glove box and stored in the fridge of the glove box.

4.2.2 Synthesis of gallium tris (trimethylsilyl) amide

$$3\mathrm{LiN}[(\mathrm{CH_3})_3\mathrm{Si}]_2 + \mathrm{GaCl_3} \rightarrow 3\mathrm{LiCl} + \mathrm{Ga}(\mathrm{N}[(\mathrm{CH_3})_3\mathrm{Si}]_2)_3$$

A metathesis reaction is typically used to synthesize silyl amide complexes. Gallium chloride (1.15 g or 6 mmol) was dissolved in 80 mL diethyl ether in a schlenk flask inside the glove box. The schlenk flask was then removed and set on a stir plate set to 60 ^{0}C. Lithium bis (trimethylsilyl) amide (20 mmol) was separately dissolved in 40 mL diethyl ether and slowly added to the mixture at 60 ^{0}C using two 24 mL syringes. The mixture was left for 24 hours and covered in aluminum foil. The cloudy mixture was then filtered using a syringe filter and the solution dried to obtain gallium tris (trimethylsilyl) amide. It was then collected and stored in the fridge inside the glove box.

4.3 Synthesis and Characterization of Pt-Ga nanoparticles

4.3.1 Pt-Ga Architectures

A. Alloy nanocrystals

A 2 mL benzyl ether solution of 0.075 mmol PtAc and 0.0025 mmol Ga-X (X=Ac, N, NSi or Cl) was prepared under argon. A 3 ml solution of 1-octadecene, 1.15 mmol of OAc, OLAm and 0.38 mmol of HDD was heated to 100 ^{0}C under Argon and vacuumed for 60-90 minutes. It was subsequently heated to 300 ^{0}C under argon and the PtAc-GaX in benzyl ether solution was injected into this hot mixture at 0.2 ml/min using a syringe pump. After 20 minutes, the heat source was removed. Care must be taken during the reaction, as octadecene is heated near its boiling point and severe bumping of the reaction occurs occasionally during the gradual injection. The reaction was then cooled to room temperature and hexane added near 70 ^{0}C. It was purified through repeated dispersions of hexane and acetone in a 1: 0.6 ratio.

Alternatively, Pt-Ga nanoparticles could be synthesized using a stronger reductant, lithium bis (trimethylsilyl) amide, with all other conditions kept constant.

B. Pt-Ga Heterostructures

Platinum was deposited onto Ga nanoparticles via a one pot reaction. First, Ga nanoparticles were synthesized according to a protocol reported by Kovalenko [152], using 25 mg GaN. Then, the temperature was decreased to 180 ^{0}C while still under Argon, and a Pt solution of 8 mg PtAc dissolved in 0.4 mL dry benzyl ether was added at 0.1 mL/min using a syringe pump. The reaction was left for 12 minutes and then quenched. After repeated dispersions in hexanes and ethanol, the final product was redispersed in toluene.

C. Using Ga and Ga_xO_y nanoparticles

Ga nanoparticles were synthesized according to the protocol reported by Kovalenko [152]. Briefly, 75 mg of GaN was dissolved in 3.39 mL dry dioctylamine and 3.75 ml dry octadecene. This was quickly injected into a hot solution of dry octadecene at 290 ^{0}C and the temperature immediately reset to 240 ^{0}C. After 2 minutes, the reaction was quenched, cleaned and redispersed in chloroform and oleic acid. After repeated centrifuging, it was dispersed in hexanes. As reported by Kovalenko, an observable color change of colorless to orange-brown occurred at about one minute, and subsequently turned black, indicative of nucleation of Ga nanoparticles.

Hollow Ga_xO_{1-x} were synthesized using a post-synthetic treatment. After two minutes of reaction time for synthesis of Ga nanoparticles using 25 mg GaN, 100 mg trimethylamine-N-oxide was added at 200 ^{0}C. The temperature was then cooled to 180 ^{0}C and left overnight. The nanoparticles were cleaned in a similar fashion and left for 2-3 days.

In order to examine decomposition of the Ga precursors in the synthetic protocol developed, 0.1 mmol of Ga precursor alone was dissolved in 0.5 ml benzyl ether and quickly injected into the same mixture, as described earlier, of octadecene, OAc, OLAm and HDD. GaN, GaNSi, GaAc and $GaCl_3$ were used and the reaction mixture was left for 15 minutes. No observable color change occurred at 300 ^{0}C after this time. $GaCl_3$ and GaNSi were left for an additional 85 minutes, at which no further color change was observed. The same was observed for a one hour decomposition of GaAc at 300 ^{0}C.

4.3.2 Energy Dispersive Spectroscopy and X-Ray Diffraction of Pt-Ga alloys

A. Background and Theory of Energy Dispersive Spectroscopy

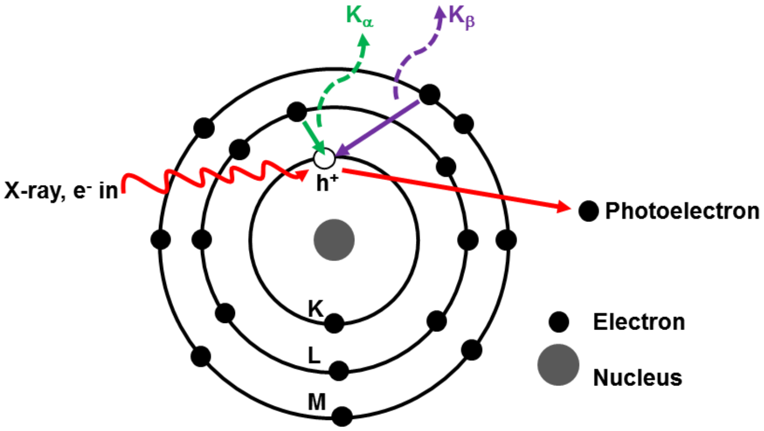

Figure 4.1 Core-level Energy Transitions upon Illumination with an X-Ray or Electron beam

When an atom is ionized by an electron, an inner shell electron is ejected, leaving an outer shell electron to fill the vacancy. Thus, characteristic X-ray energies (e.g. K_α, K_β Figure 4.1) unique to the ionized atom are emitted. The other type of X-rays which can be emitted are Bremsstrahlung X-rays, which result when beam electrons are slowed down from interaction with the coulomb field of the nuclei in the sample. Thus, characteristic X-rays typically appear as Gaussian-shaped peaks which are superimposed on a background of a continuum of Bremsstrahlung X-rays, also known as braking radiation. This X-ray background must be carefully subtracted in order to perform quantitative analysis of the EDS peaks. The fluorescence yield (ω) of electrons is a strong function of Z, the atomic number, according to the following equation:

$$\omega = \frac{Z^4}{\alpha + Z^4} \quad \alpha \approx 10^6 \; for\; K\; shell \qquad (4.1)$$

The detector in EDS is a silicon-lithium reversed biased p-i-n diode. When it interacts with X-rays, thousands of electron-hole pairs are generated in the intrinsic Si and separated by an applied bias. A charge pulse proportional to the X-ray energy results, as the number of electron-hole pairs is proportional to the energy of the incident X-ray. Collection of these pairs allows for the distinguishing of elements. The charge pulse is converted to a voltage and the signal amplified though a field effect transistor. It is isolated from other pulses and electronically identified as resulting from an X-ray of a specific energy after further amplifying. The detector must be cooled with liquid N_2 to avoid thermal energy activation of electron-hole pairs, resulting in a S/N ratio that would wash out the X-ray signal of interest. Furthermore, Li atoms would diffuse under the applied bias, destroying the intrinsic properties of the detector.

EDS mappings are done in Scanning Transmission Electron Microscopy (STEM) mode, where the beam is focused onto the sample and scanned in a raster. This allows for formation of an image of each element in the sample as the e^- beam is scanned across it. In conventional TEM mode, the signal results from forward scattered electrons that go through the sample. In z-contrast (or High Angle Annular Dark Field) imaging, heavier elements appear brighter.

All HAADF/EDS imaging was done on the FEI TitanX 60-300 microscope at NCEM. Images were acquired using a HAADF detector for STEM. The accelerating voltage was set to 200 kV, with an extraction voltage of 4100 V, spot size of 4 and camera length of 130 mm. The convergence angle in this case was 10 mrad. The probe size is limited to ~ 1 nm and the EDS resolution is roughly 2.5 nm. The beam current was between 0.6 and 0.7 nA and the exposure time varied from 4 to 10 minutes, depending on the sample stability under the beam and counts per second. An 80 keV energy range was chosen. HRTEM imaging was done on the 200kV FEI monochromated F20 UT Tecnai at NCEM and low magnification TEM images were taken on a 200kV LaB_6 FEI Tecnai G2 20. Samples were prepared by drop casting nanoparticle solutions in hexane onto lacey carbon grids or holey carbon grids (NCEM only).

Pt_xGa_{1-x} nanoparticles were analyzed at the Pt L (green, unless otherwise stated) and Ga K (red unless otherwise stated) edges, which overlap at ~ 9.5 keV (Appendix A2.6). All data analyses were performed using software developed by Bruker in the Esprit application, to determine the atomic % of Pt and Ga. Then, the composition of nanoparticles were analyzed and an average atomic % of Ga tabulated using the standard deviation from the fitted data and taking the heterogeneity within the sample into account. This propogated deviation per sample was calculated as the square root of the average variance for a given sample size. All reported standard deviations for EDS are for a 95% confidence interval while all other standard deviations reported are for σ.

The particle diameter was determined using the HAADF image of each nanoparticle EDS was performed on. The area of each region in the particle analyzed was estimated to be a circle and the diameter extracted based on the area (in pixels) given by Esprit for each particle. These sizes were cross checked using TEM to verify the size distribution obtained made sense.

B. Results

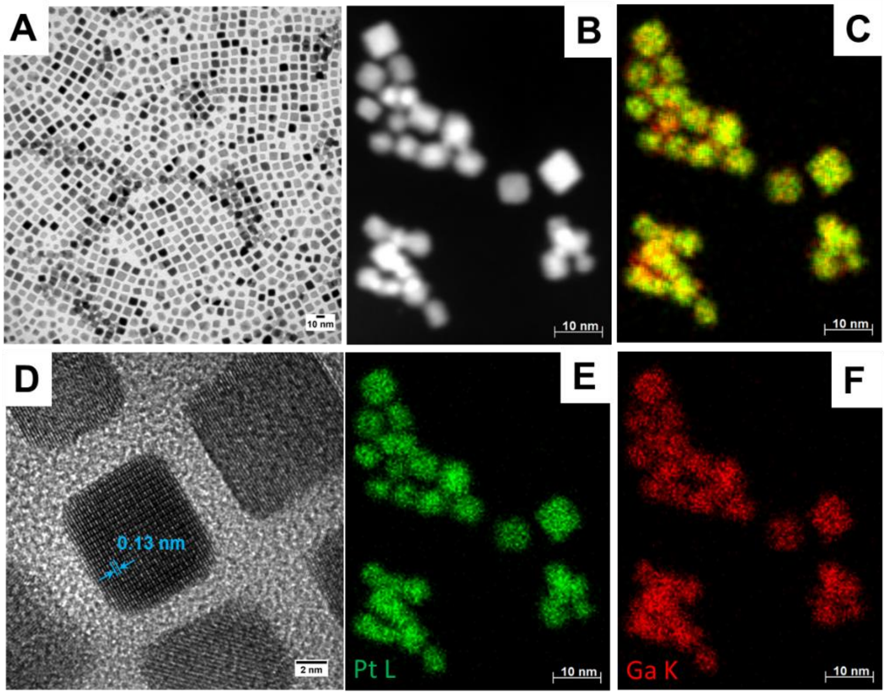

Figure 4.2. (A, D) Representative TEM of Pt_3Ga nanoparticles synthesized with GaAc precursor and corresponding (B) HAADF and (C-F) EDS mapping.

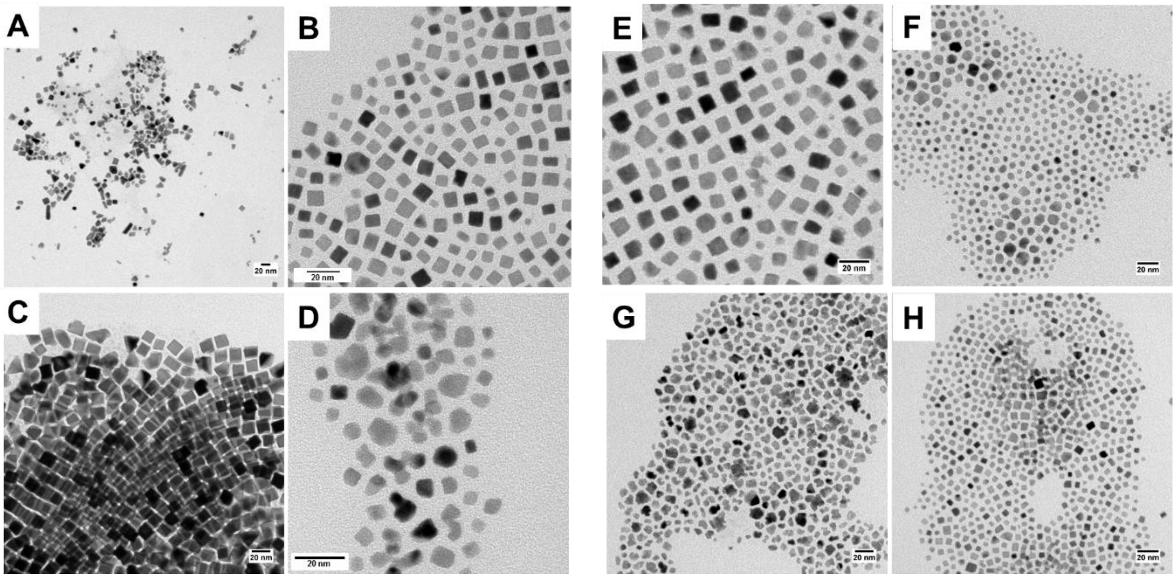

Figure 4.3. 3:1 Pt:Ga nanoparticles synthesized with (A) GaN (B) GaAc (C) GaNSi (D) $GaCl_3$ and 2:1 Pt:Ga nanoparticles synthesized with (E) GaN (F) GaAc (G) GaNSi (H) $GaCl_3$

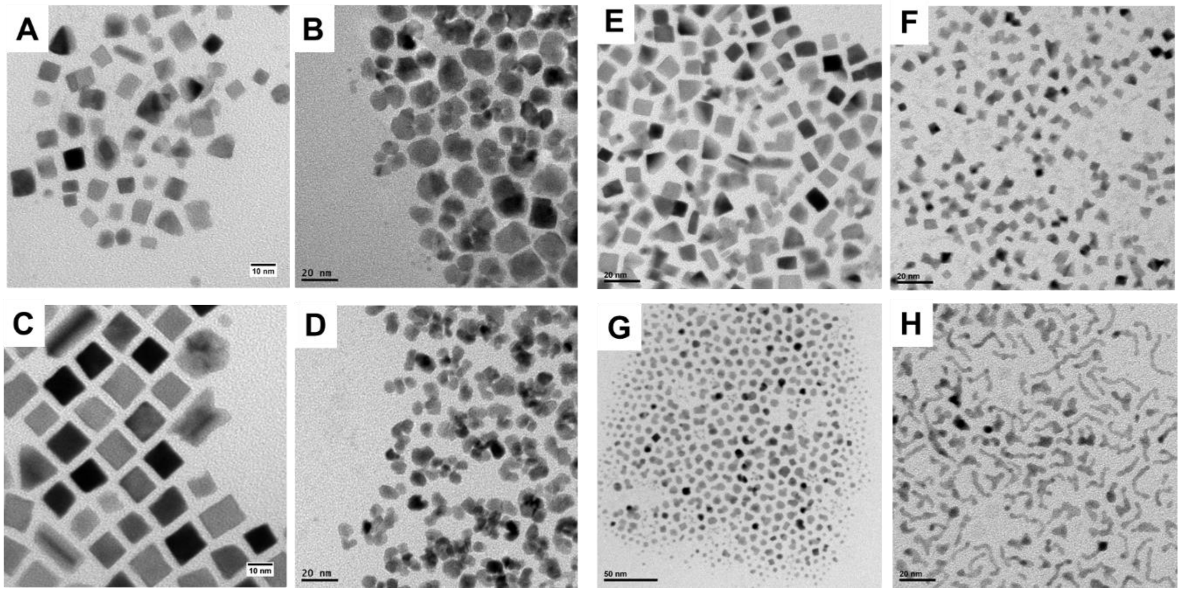

Figure 4.4. 1:1 Pt:Ga nanoparticles synthesized with (A) GaN (B) GaAc (C) GaNSi (D) $GaCl_3$ and 1:2 Pt:Ga nanoparticles synthesized with (E) GaN (F) GaAc (G) GaNSi (H) $GaCl_3$

Pt-Ga nanoparticles were synthesized using different ratios of Pt:Ga precursor (3:1, 2:1, 1:1, 1:2) and HDD as a reductant (Figures 4.3 and 4.4). Morphological differences were seen as the ratio of Ga was varied, most notably in the use of $GaCl_3$ in 1:2 Pt:Ga where worm-like nanowires resulted (Figure 4.4 h). Qualitative trends in the Ga reactivity can be discerned from the elemental analysis using EDS. The EDS of these samples shows that the Ga incorporation for Pt rich alloys is higher when using the alkylamine and silylamide Ga precursors (Figure 4.5). In the case of excess Ga precursor, the opposite is seen, where the chloride and carboxylate Ga precursors have a higher Ga content in the Pt-Ga alloy. 1:1 Pt:Ga is not shown for comparison since the experimental conditions of GaN and GaNSi were slightly different (synthesized at 270 ^{0}C). They are however included in other results for the reader's knowledge.

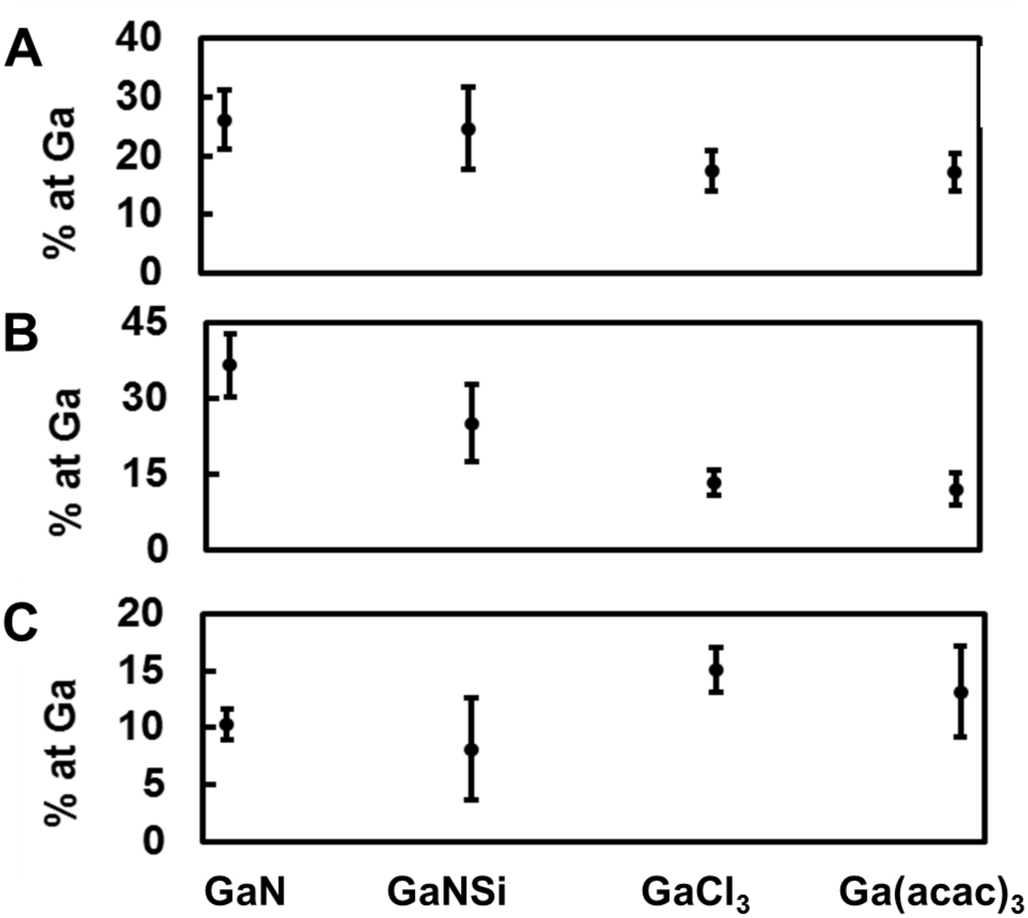

Figure 4.5 Comparison of % atomic Ga incorporation in alloys of Pt:Ga (A) 3:1 (B) 2:1 (C) 1:2 determined from EDS

The heterogeneity in Ga incorporation can be seen by examining several individual Pt-Ga alloy nanocrystals using EDS. The representative raw data of the Pt L and Ga K edge overlay signals for different ratios of Pt:Ga (3:1, 2:1, 1:1, 1:2) are presented in Figures (4.6-4.9 A, D, G, J). The EDS data is also presented in reference to the size of the Pt-Ga alloy analyzed as a scatter plot of nanoparticle diameter vs % atomic Ga incorporation, to determine whether or not there is a correlation in the size and composition of the nanoparticles.

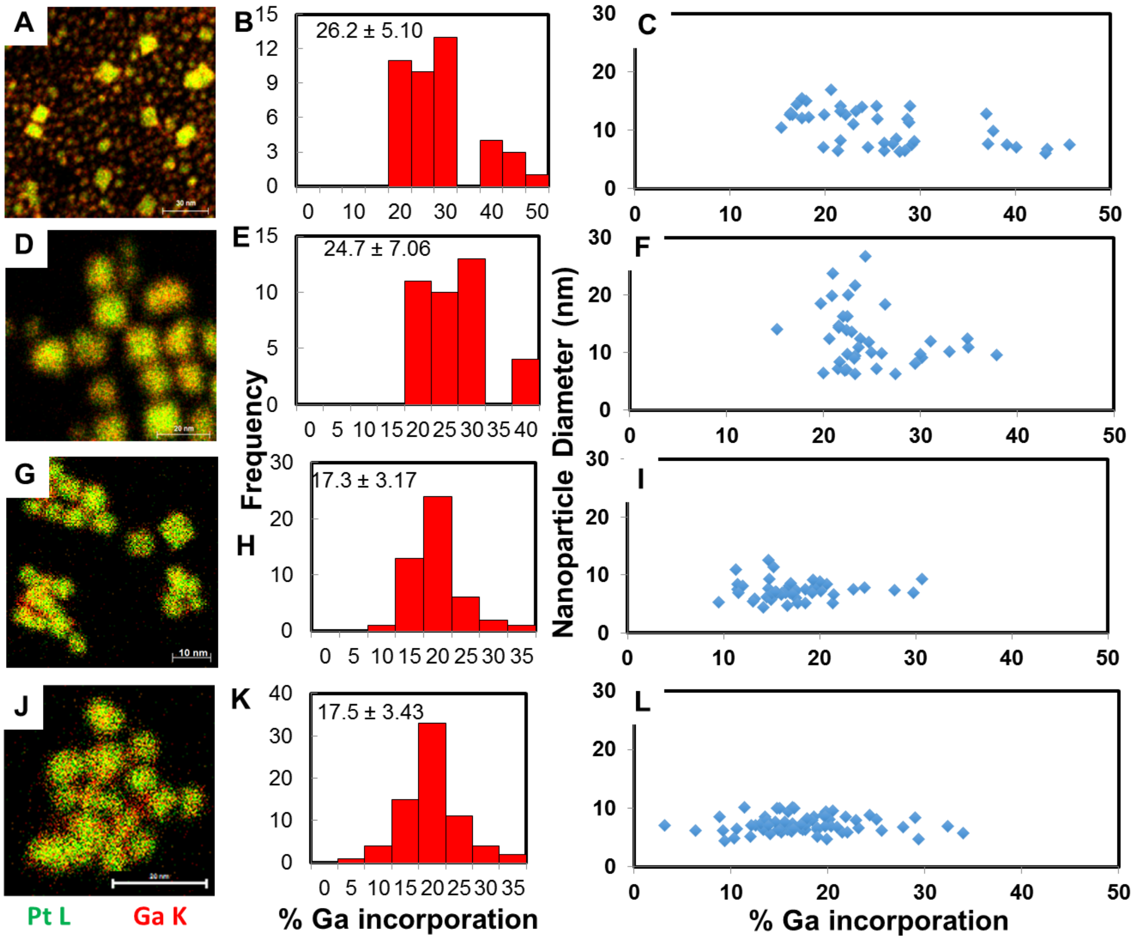

Figure 4.6. 3:1 Pt:Ga nanoparticles and their corresponding EDS map, % atomic Ga incorporated and their correlation to the nanoparticle diamater when synthesized with (A- C) GaN (D- F) GaNSi (G- I) GaAc and (J-L) $GaCl_3$ respectively

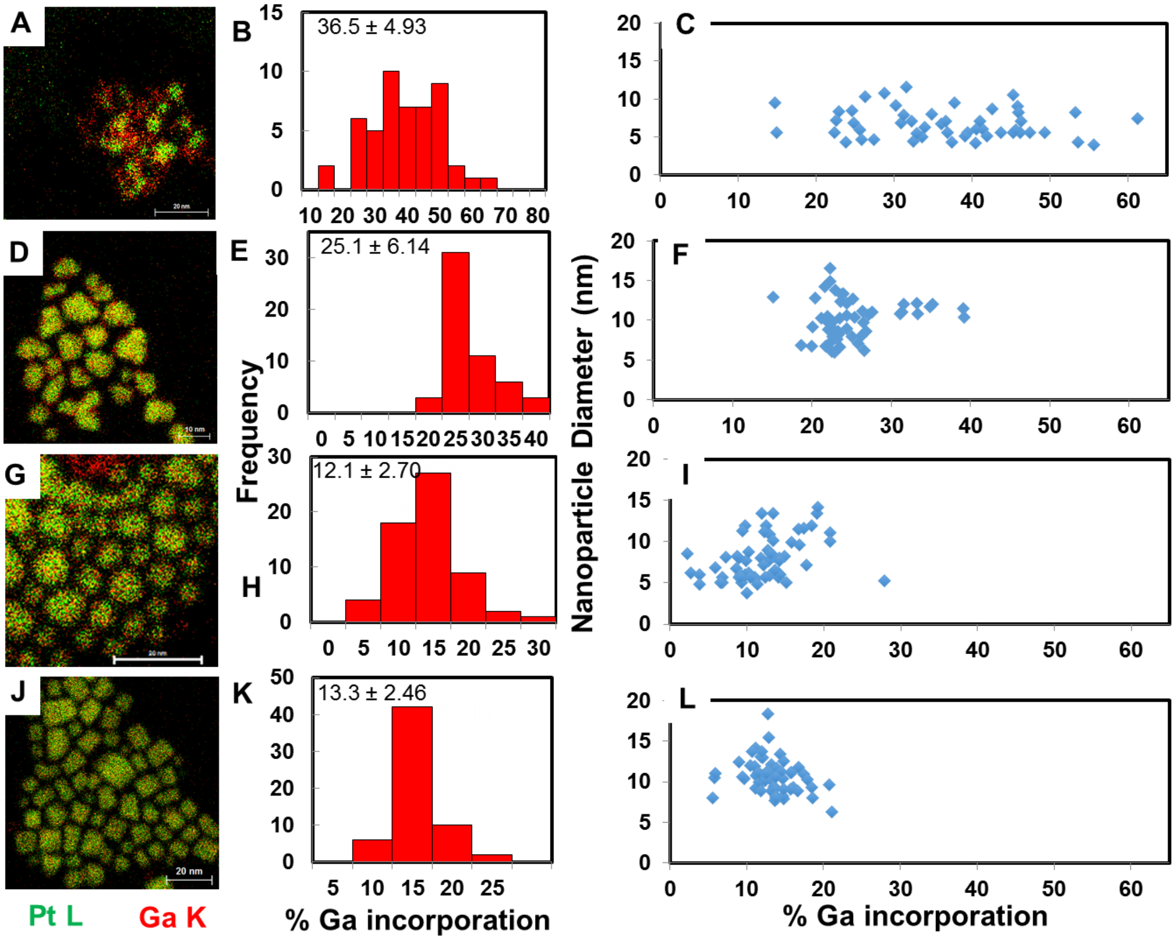

Figure 4.7. 2:1 Pt:Ga nanoparticles and their corresponding EDS map, % atomic Ga incorporated and their correlation to the nanoparticle diamater when synthesized with (A- C) GaN (D- F) GaNSi (G- I) GaAc and (J-L) $GaCl_3$ respectively

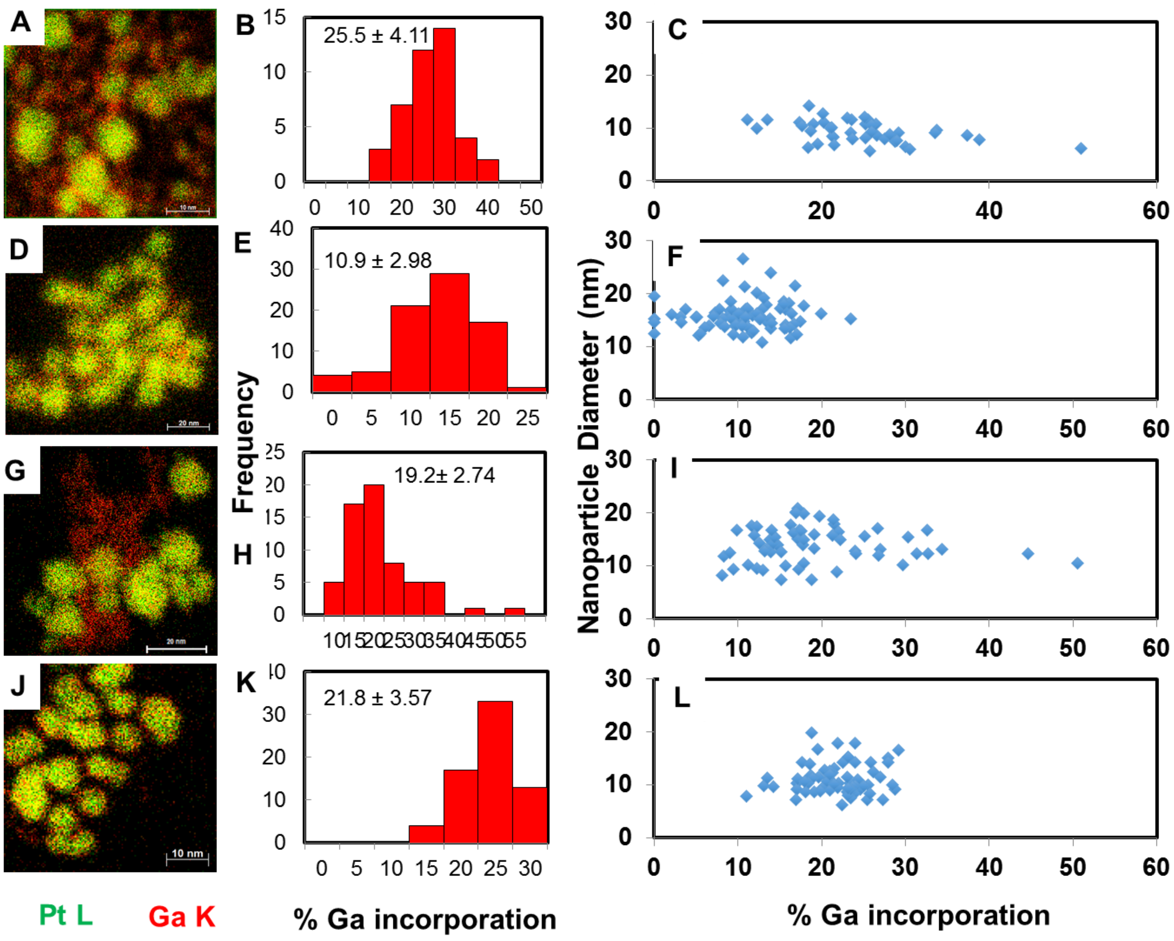

Figure 4.8. 1:1 Pt:Ga nanoparticles and their corresponding EDS map, % atomic Ga incorporated and their correlation to the nanoparticle diamater when synthesized with (A- C) GaN (D- F) GaNSi (G- I) GaAc and (J-L) $GaCl_3$ respectively

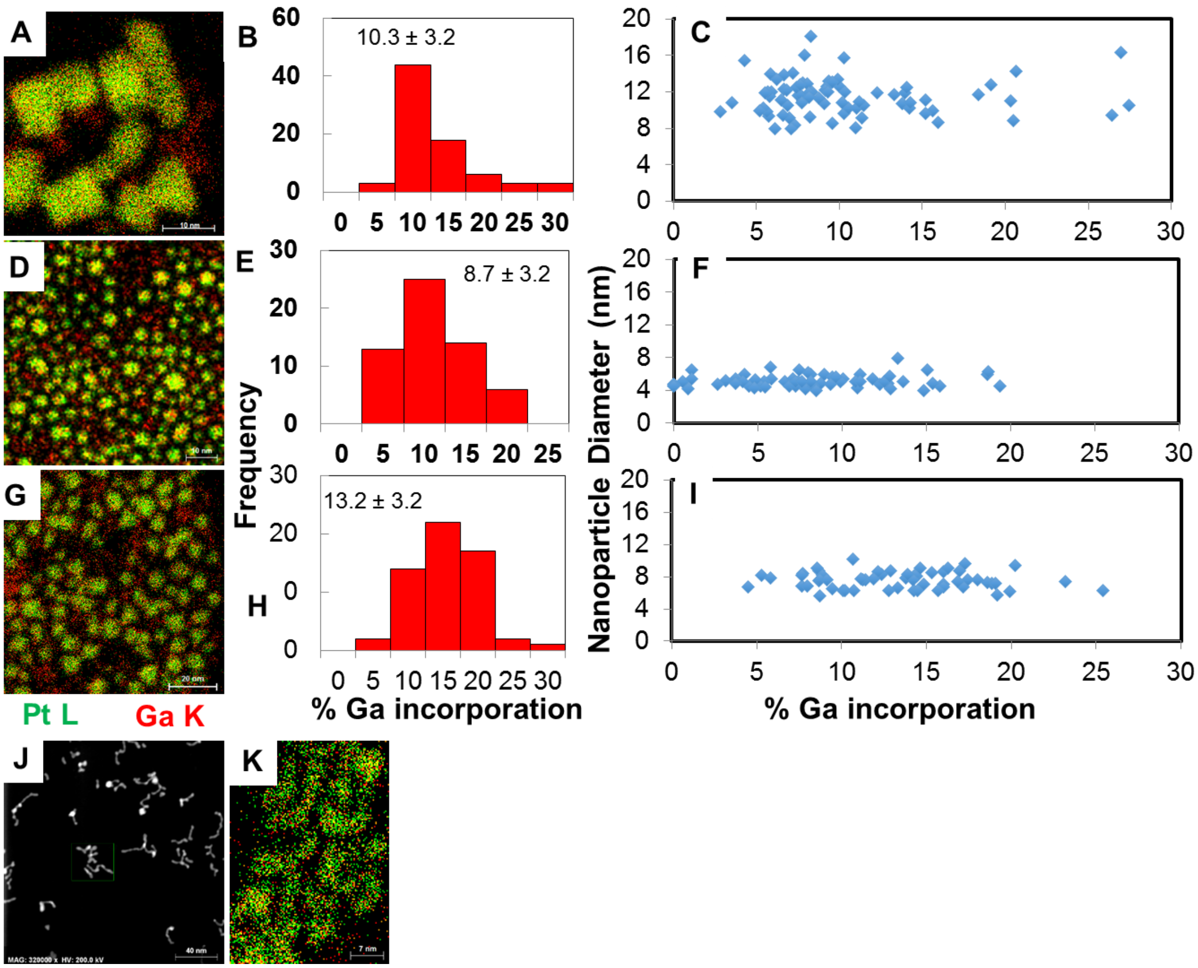

Figure 4.9. 1:2 Pt:Ga nanoparticles and their corresponding EDS map, % atomic Ga incorporated and their correlation to the nanoparticle diamater when synthesized with (A- C) GaN (D- F) GaNSi (G- I) GaAc and (J, K) $GaCl_3$ respectively

The EDS results for the % Ga incorporated are summarized in Table 4.1 while the particle diameters determined from the HAADF images are sumarized in Table 4.2.

Pt:Ga used:	3:1	2:1	1:1	1:2
Ga precursor	% atomic Ga	% atomic Ga	% atomic Ga	% atomic Ga
GaAc	17.3 ± 3.17	12.06 ± 2.7	19.17 ± 2.74	13.2 ± 4.05
$GaCl_3$	17.47 ± 3.43	13.27± 2.46	21.76 ± 3.57	15.08 ± 1.93
GaNSi	24.7 ± 7.06	25.06 ± 6.14	10.87 ± 2.98	8.09 ± 4.50
GaN	26.17 ± 5.10	36.49 ± 4.93	25.47 ± 4.11	10.29 ± 1.40

Table 4.1. Summary of % atomic Ga ± 2σ of nanoparticles characterized by EDS

Pt:Ga used:	3:1	2:1	1:1	1:2
Ga precursor	Diameter (nm)	Diameter (nm)	Diameter (nm)	Diameter (nm)
GaAc	8 ± 1.6	7.9 ± 2.6	14.1 ± 3.3	7.6 ± 1.1
$GaCl_3$	7.4 ± 1.4	5.6 ± 3.1	11.1 ± 2.9	
GaNSi	12.4 ± 5.1	10.1 ± 2.5	15.8 ± 2.8	5.2 ± 0.8
GaN	10.6 ± 3.1	6.8 ± 1.9	9.2 ± 2.1 nm	11.5 ± 2.0

Table 4.2. Distribution of particle diameters ($D \pm \sigma$) of nanoparticles characterized by EDS taken from HAADF images

When a stronger reducing agent, LiNSi, was used as opposed to the HDD, the final morphology and growth mode was markedly different (Figure 4.10 a-c) for the GaNSi precursor. Oriented attachment of individual nanoparticles when LiNSi was used as a reductant formed a mixture of worm-like and dendritic structures over time. In contrast, HDD results in nanoparticles that have well defined shapes (Figure 4.10 d-f), as seen in the example of 3:1 Pt:Ga alloy nanocrystals. Representative EDS maps are shown in Figure 4.11 a-c and d-g for 3:1 Pt:Ga and 5:3 Pt:Ga respectively.

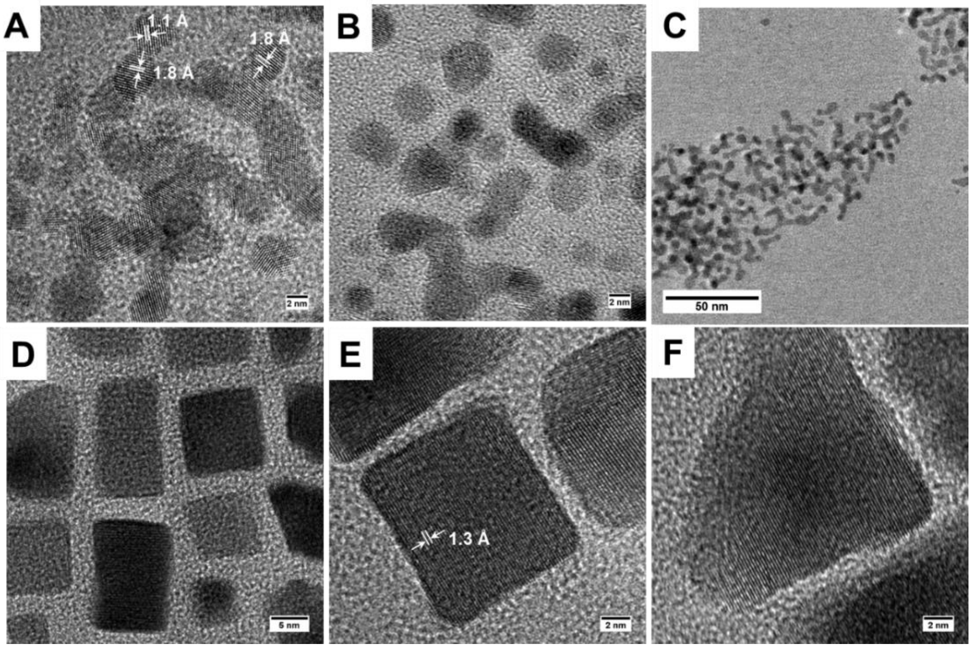

Figure 4.10. TEM of 3:1 Pt:Ga nanoparticles synthesized using GaNSi and LiNSi after (A, B) 20 minutes (C) 40 minutes. LiNSi was also replaced by HDD (D-F)

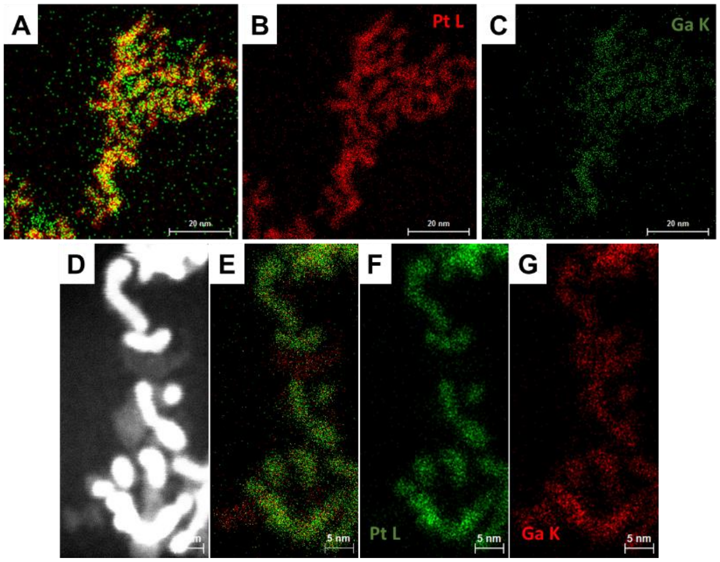

Figure 4.11. 3:1 Pt:Ga nanoparticles synthesized using GaNSi and LiNSi and representative corresponding EDS mapping (A-C). (D) HAADF of 5:3 Pt:Ga and corresponding EDS (E-G)

Slow, partial decomposition of the Ga precursors in the absence of Pt is observed and shown in Figure 4.12 for reference. The alkyl amide and silyl amide precursors seem to produce some hollow nanoparticles as well.

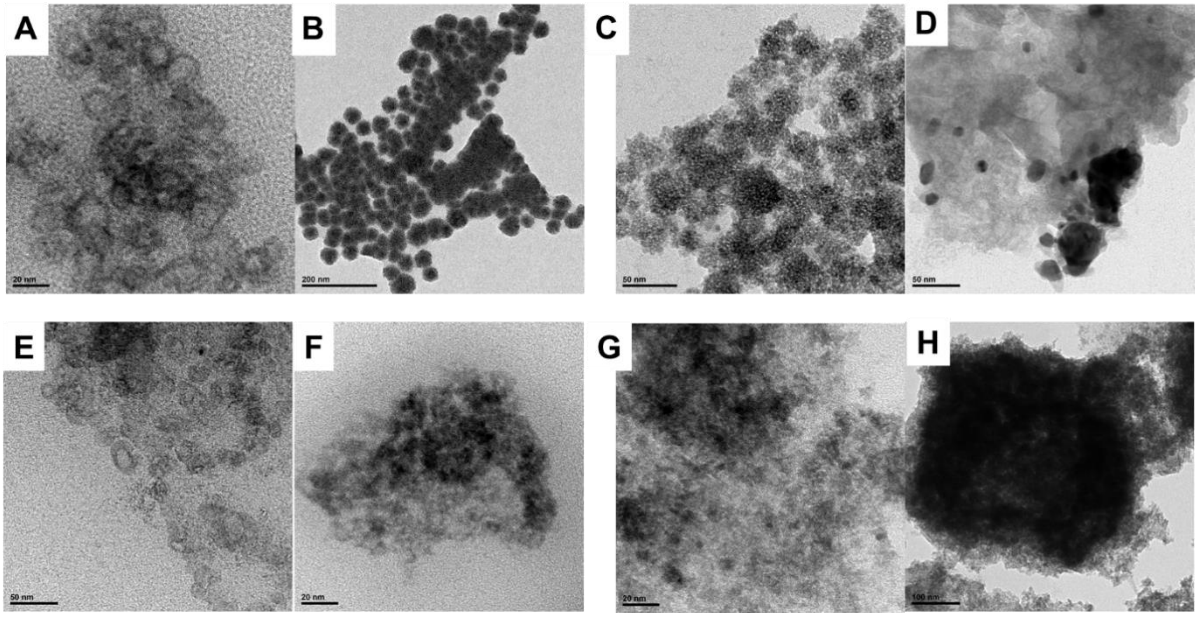

Figure 4.12 Thermal decomposition of Ga precursors (A, B) GaN (C, D) GaAc (E, F) GaNSi and (G, H) $GaCl_3$

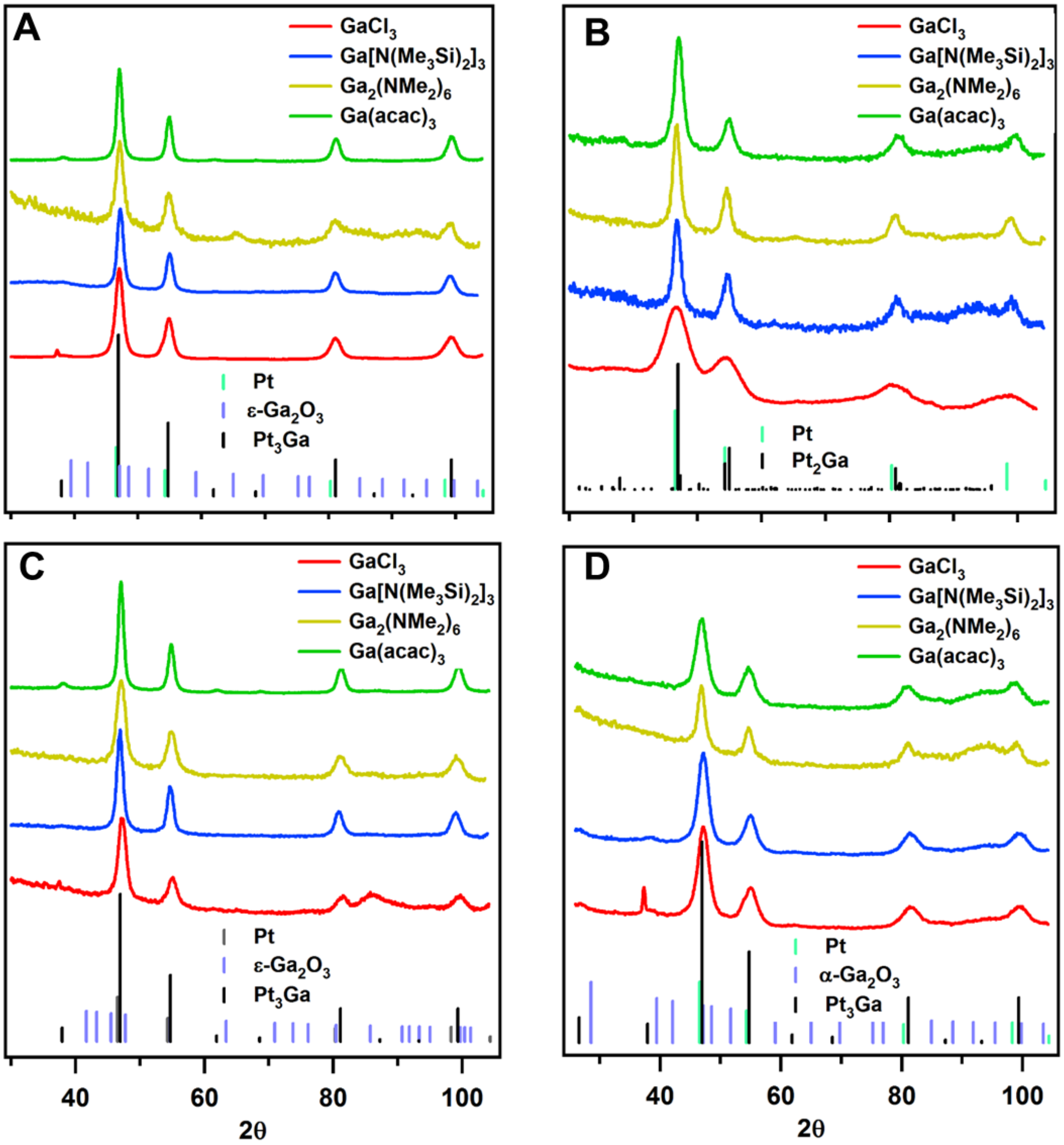

Figure 4.13 XRD of Pt:Ga alloy nanocrystals synthesized with (A) 3:1 (B) 2:1 (C) 1:1 (D) 1:2 ratios. Reference files are Pt #01-088-2343, Pt_3Ga #03-065-9177, ε-Ga_2O_3# 01-082-3196 and α-Ga_2O_3 #00-006-0503

C. Discussion

Pt-Ga alloy nanocrystals of different morphology and composition were synthesized using four different Ga precursors (GaN, GaAc, GaCl, GaNSi). As Figures 4.3 and 4.4 show, the morphology of the Pt-Ga alloys varies from well defined cubes and tetragonally shaped nanoparticles to wires, dendrites and irregular shapes, and finally, small nanoparticle clusters. The strength of the reducing agent was also found to play a role in determining the final morphology of the nanoparticles. For the targeted Pt-rich alloys of 3:1 and 2:1 Pt:Ga, the % atomic Ga incorporated determined from EDS decreases as $Ga_2(NMe_2)_6$ > $Ga[N(Me_2)Si)\ _2]_3$ > $GaCl_3$ > $Ga(acac)_3$. How can this be understood? From a general approach, precursors which have a more electron withdrawing substituent, such as acetylacetonate or chloride, can be easily reduced and lead to a higher Ga incorporation. Electron withdrawing substituents would destabilize the metal center and lower its reduction potential. In contrast, electron donating substituents of the GaN and GaNSi would make it harder to reduce. This trend has been studied using Pt(IV) complexes by Spaulding. They examined the reduction of a series of Pt^{IV} complexes with chloro substituents by ascorbic acid and found that the cathodic reduction potentials were strongly influenced by the electron withdrawing power and steric hindrance of the ligands. They determined reduction rates and showed that reduction potentials decreased with increasing electron withdrawing power as $OH<OCOCH_3<Cl<OCOCF_3$ [153].

In this work, Ga precursors with electron withdrawing substituents are less reactive than the alkylamide and silylamide Ga precursors. These precursors are hypothesized to be so because of the neutral ligand environment, and hence neutral Ga metal center. Since these Ga centers are nuetral, they would react via a decomposition route as opposed to a co-reductive route. This could account for the higher Ga incorporation seen in Pt rich Pt-Ga alloys made from these precursors. While thermal decomposition of the other precursor occurs to some extent at these high temperatures (Figure 4.12), it is minor in comparison. Kovalenko has done molecular simulations to show that these amide precursors readily decompose at high termperatures while the carboxylate analogue does not.

Kovalenko has studied the use of metal alkylamides and silylamides as element-nitrogen bonded metal precursors [117], [125], which are highly reactive in reduction reactions. The M-N bond is polar and is senstive to reducing and oxidizing agents. In their theoretical studies on the thermal stability of these types of precursors, the C-H bonds were found to be susceptible to cleavage above 180 ^{0}C. Molecular dynamics calculations of the GaNSi precursor revealed C-H cleavage at 250 ^{0}C, leading to formation of a four center intermediate of configuration Ga-N-Si-C. This is in stark contrast to M-O bonded precursors such as GaAc. When moelcular dynamic simulations were run for a Sn^{II} hexanoate as a model to compare to Sn-NSi, decomposition of the silylamide occurred above 180 ^{0}C, while no decomposition was observed for the Sn carboxylate species. Instead, Kovalenko reported that Sn-O bonds lengthened and only stretching and bending modes of C-H bonds were activated. Since no breaking of the Sn-O bond was observed, this proved the higher reactivity of M-N over M-O bonded precursors. High temperature decomposition of the Ga precursors in the absence of Pt produced minute amounts of a separable product after several cycles of centrifuging. TEM of the products revealed nanoparticles with different structures (Figure 4.12).

Thus, in line with Kovalenko's findings, a thermal decomposition route gave higher atomic % Ga incorporated in the 2:1 and 3:1 Pt:Ga cases when compared to the GaAc and GaCl precursors. 3:1 Pt:Ga using GaNSi, GaN, GaAc and GaCl yielded average atomic % Ga of 24.7, 26.2, 17.3 and 17.5, while 2:1 Pt:Ga yielded average atomic % Ga of 25.1, 36.5, 12.1 and 13.3, respectively (Table 4.1). For the Pt-rich alloys, GaN consistenly gave the highest Ga incorporation, followed by the silylamide GaNSi. It also gave a broad size distribution, as EDS of 3:1 Pt:Ga shows a combination of large and small nanoparticles while 2:1 Pt:Ga shows some Ga rich regions are present (Figure 4.6 and 4.7). These may be due to residual unreacted Ga precursor or some Ga oxide species. Based on the HAADF images, the average size of 3:1 Pt:Ga analyzed with EDS using GaNSi, GaN, GaAc and GaCl yielded average diameters of 12.4, 10.1, 8.0 and 7.4 nm while 2:1 Pt:Ga yielded average diamaters of 10.1, 6.8, 5.6 and 7.9 nm respectively (Table 4.2). GaNSi yielded 3:1 Pt:Ga nanoparticles with cubic and tetragonal shapes and irregularly shaped 2:1 Pt:Ga nanoparticles. GaAc gave fairly uniformly shaped 3:1 Pt:Ga and 2:1 Pt:Ga nanoparticles, while $GaCl_3$ gave a variety of morphologies for 3:1 Pt:Ga and 2:1 Pt:Ga. While cubic nanoparticles were seen for both these cases of $GaCl_3$, some shaped branched and quasi-spherical particles were also seen. There does not seem to be any clear trend in the nanoparticle diameter vs % atomic Ga incorporated of any Pt-Ga sample size analyzed.

In the case of starting with excess Ga precursor, different trends are observed for the % atomic Ga incorporated. For 1:2 Pt:Ga, the % atomic Ga incorporation determined from EDS decreases as $GaCl_3$ > $Ga(acac)_3$> $Ga_2(NMe_2)_6$ > $Ga[N(Me_2)Si)_2]_3$, corresponding to 15.1> 13.2> >10.3>8.1 respectively (Table 4.1). While this is the opposite of the trend seen for Pt-rich alloys, it is worth mentioning that unreacted $GaCl_3$ was detected in its XRD, and EDS and TEM revealed the presence of much lighter contrast, splindle-like nanoparticles for the other Ga precursors. These are presumably gallium rich nanoparticles, and may partially account for the drop in Ga incorporation of the alloys. 1:2 Pt:Ga analyzed with EDS using GaNSi, GaN and GaAc and GaCl yielded average diameters of 5.2, 11.5 and 7.6 nm (Table 4.2). GaCl produced nanowires with an average wire diameter of 4 nm.

Excess Ga led to quasi-cubic and faceted morphologies, producing wires in the case of $GaCl_3$. This is presumably due to oriented attachment [154], [155] of individual nanoparticles, as the HAADF and TEM images clearly show wires with a few individual nanoparticles present (Figure 4.4 h and 4.9 j, k). For the equimolar and excess Ga cases, the morphological changes were more sensitive to the Ga precursor used. For 1:1 Pt:Ga, cubes are the predominant morphology, with some tetragonal and elongated cubic structures for the GaN and GaNSi precursors. However, GaAc seems to have formed either large nanoparticles due to calescence and sintering of smaller nanoparticles or small clusters of individual Pt-Ga nanoparticles. GaCl formed a variety of structures, with smaller clusters of dendritic nanoparticles. 1:1 Pt:Ga using GaNSi, GaN, GaAc and GaCl yielded average atomic % Ga of 10.9, 25.5, 19.2 and 21.8 with corresponding average sizes of 15.8, 9.2, 14.1 and 11.1 nm, respectively (Table 4.2). Initial attempts to control the size using different ratios of organic ligands OAc and OLAm were unsuccesful (Appendix A2.4 and 2.5).

The strength of the reducing agent used had a big influence on the final morphology of Pt-Ga nanoparticles (Figure 4.10, 4.11) synthesized using GaNSi. In the case of using a strong reducing agent, LiNSi, a mixture of worm-like nanowires and dendritic structures were formed. This was in stark contrast to using HDD, a mild reducing agent. Use of a mild reducing agent can provide control over the nucleation and growth kinetics, leading to well controlled morphologies. Strong reducing agents often lead to very fast and uncontrolled nucleation and growth, leading to massive aggregation when there is not enough time for ligands to stabilize facets during growth or nanowires [156]. Such was the case when GaAc was used, as no wire or dendrite formation was seen. For these reasons, HDD was the reductant of choice, where modulation of the nucleation rate and growth kinetcs led to a well defined nanoparticle morphology overall.

XRD suggests intermetallic phases of Pt-Ga were synthesized in certain cases, while other spectra resembled bulk Pt (Figure 4.13). The line phase of Pt_3Ga was mapped in the 3:1 Pt:Ga using GaAc case. Pt_3Ga was dstinguished from Pt by three weak reflections at 37.9 ^{0}, 61.8 ^{0} and 68.3 ^{0} (Figure 4.13 a). Rietveld refinement of the 3:1 Pt:Ga for GaAc and GaCl suggest the bulk of the nanoparticle is an intermetallic phase (Appendix A2.2 and 2.3). In the case of 3:1 Pt:Ga with $GaCl_3$, the sharp peak below 40 ^{0} sugests there was some unreacted precursor, while the peak at 63.4 ^{0} in the GaN case suggests some Ga_2O_3 was present. The formation of intermetallic Pt_2Ga was inconclusive and the peak at 63.4 ^{0} in the GaN case was also present. The 1:1 Pt:Ga for GaAc seems to have formed Pt_3Ga nanoparticles, as indicated by three weak but unique reflections of Pt_3Ga in comparison to Pt (Figure 4.13 c). In the case of $GaCl_3$, ε-Ga_2O_3 seems to have formed as a byproduct due to decomposition of the Ga precursor. This was not observed when a 1:2 Pt:Ga was used due to the sharp peak below 40 ^{0}, indicative of unreacted $GaCl_3$ (Figure 4.13 d).

In order to determine a qualitative trend for the oxidizing strength of the Ga precursors, cyclic voltametry of the Ga precursors was done in organic solution. While these conditions do not reflect the experimental conditions under which the alloy nanocrystals were synthesized (high temperature, presence of ligands), they can shed some insight on how the precursor reactivity relate to each other. This is discussed in the following section.

4.3.3 Cyclic Voltammetry of Ga precursors

A. Theory and Experimental Conditions

Cyclic Voltammetry (CV) is a widely used electro-analytical technique to study redox reactions. The current is monitored when a potential is applied at a working electrode in the forward and reverse directions. The working electrode's potential is measured against a reference electrode, which maintains a constant potential; this varies linearly with time. The counter or auxiliary electrode conducts electricity from the signal source to working electrode. An electrolytic solution provides electrical conductivity between the electrodes, providing ions during oxidation and reduction processes. The cathodic and anodic peak potentials, E_{pc} and E_{pa}, respectively, are useful for determining the formal reduction potential for a reversible redox couple based on the average of the two values. Since the Ga precursors examined here are irreversible, the cathodic peaks are reported for the initial wave, relative to the ferrocene (Fc/Fc^+) redox couple.

The working electrode used was a glassy carbon electrode, which was polished with 50 μm alumina before use. A 2 mL solution of 0.01 M $AgNO_3$ in 11.8 % BE/DMF was prepared by sonicating the mixture for 3 hours. This faint yellow solution was used as a Ag/Ag^+ reference electrode. A platinum wire was used for the auxiliary electrode. All scan rates were 0.1 V/s using 300 μM of Ga precursor dissolved in a mixture of 11.8 v/v % benzyl ether/dimethylformamide (BE/DMF) mixture and 0.1 M $TBAFP_6$. All solvents were dried prior to use, and electrochemical grade $TBAFP_6$ was degased at 150 ^{0}C for 3 hours prior to use. Ga precursor was first dissolved in BE, then diluted using DMF for ease. The solution resistance typically measured between 15 and

30 Ω for CV scans. The blank solution consisted of only $TBAFP_6$ in 11.8% BE/DMF. All scans began at the open circuit potential, and were done for 3 full cycles consisting of both the forward and reverse scans. At the end of all scans for each precursor, a small amount of ferrocene was added as an internal potential reference.

B. Discussion of Results

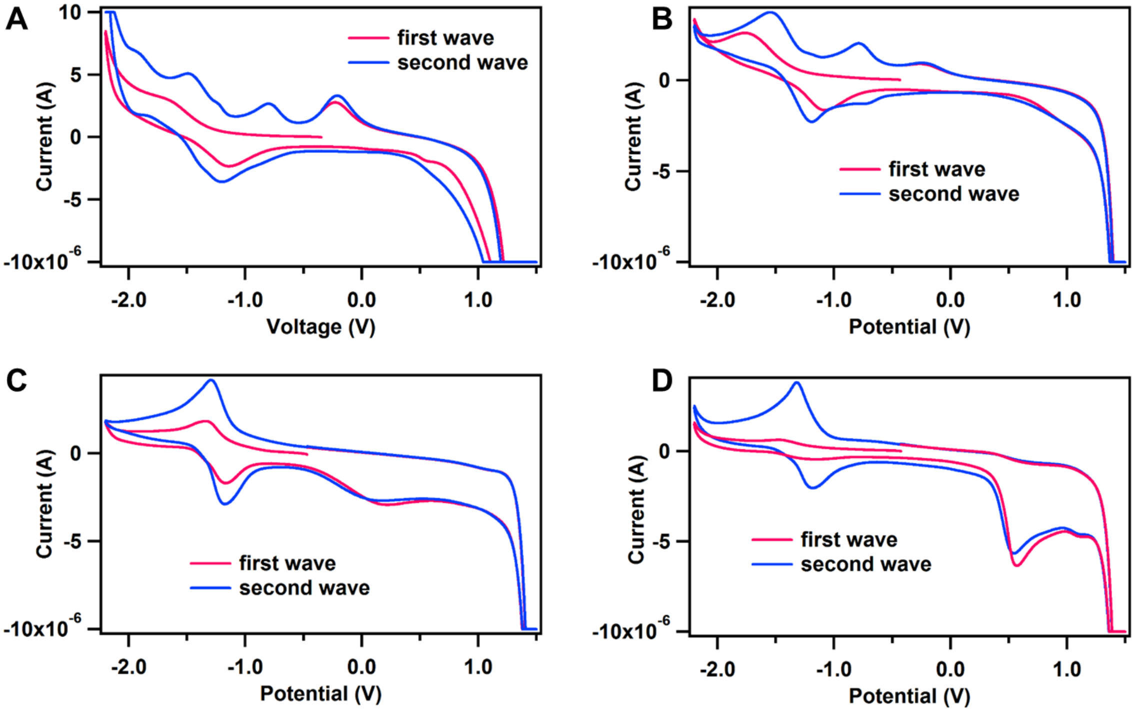

Figure 4.14. CV of Ga precursors for (a) GaAc (b) GaCl (c) GaNSi and (d) GaN showing first two waves

The first two waves of the CV for each Ga precursor are presented in Figure 4.14. In the cases of GaAc and $GaCl_3$, irreversible redox reactions occur, due to the lack of a hysteresis in the forward and reverse scans.

The onset of reduction in the first wave was chosen as the indicator of reactivity for each precursor (Figure 4.15 a). This was determined by calculating the potential at the maximum of the first derivative. While this was unclear for the $GaCl_3$ and GaAc precursors, the maximum occurred around -1.6 V. A plot of this onset potential vs the average % atomic Ga incorporation revealed a similar qualitative trend (Figure 4.15 b) of reactivity to that already observed by EDS: $Ga[N(Me_2)Si)_2]_3$ > $Ga_2(NMe_2)_6$ > $GaCl_3$ > $Ga(acac)_3$, though the alkylamide has a higher reduction onset. A table summarizing these results is presented in Table 4.3.

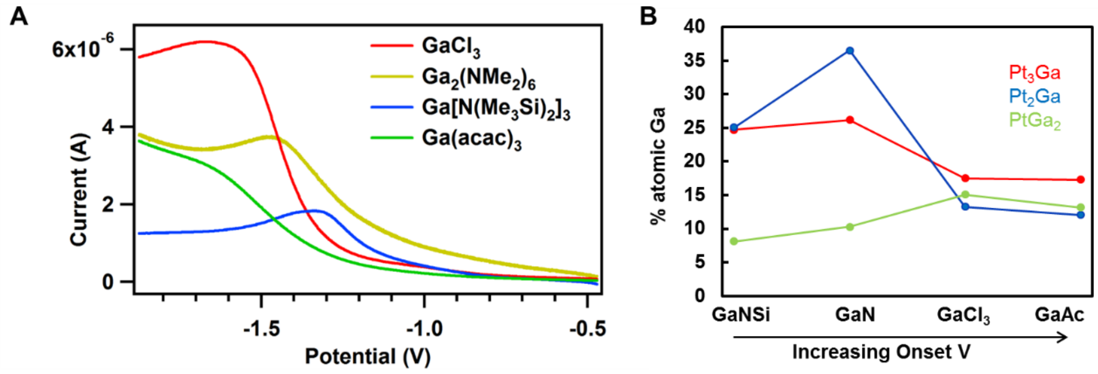

Figure 4.15. CV of (A) Ga precursors and (B) atomic Ga incorporated vs onset reduction potential

$E_{p,c}$ (V)	Fc^+/Fc (V)	$E_{p,c}$ vs Fc^+/Fc (V)	Onset vs Fc^+/Fc (V)	Ga-X (X=)
NA	0.046	NA	-1.56	Ac
NA	0.039	NA	-1.49	Cl
-1.433	0.047	-1.490	-1.35	N
-1.302	0.045	-1.347	-1.22	NSi

Table 4.3. Summary of CV results for Ga precursors relative to Fc/Fc^+. $E_{p,c}$ for Cl and Ac was estimated to be -1.6 V

As seen by the CV, the alkyl and silyl amides are more reactive overall, thus the Ga incorporation is higher for these Ga precursors. Furthermore, the Ga incorporation in the alkyl amide seems to be slightly higher than the silyl amide, presumably due to the bulkier NSi ligand on the metal Ga center, which should stabilize the metal center more. While this is not reflected perfectly in the CV, a qualitative understanding of the precursors is still possible. The standard reduction potential for $Ga^{3+/0}$ is -0.529 V vs NHE. Since the GaNSi was quasi-reversible, a standard reduction potential was calculated using the average of the cathodic and anodic peaks to see how it compared to the standard value. Relative to NHE (add 0.63 V for Fc^+/Fc), a more negative reduction potential of $E^0_{GaNSi} = -0.667\ V$ was obtained. Similarly, for GaN, $E^0_{GaN} = -0.737\ V$ was obtained. At the very least, this shows the local ligand environment of the metal center in the precursor can change the reduction potential by varying degrees.

4.4. Pt Deposition onto Ga/Ga_xO_y Nanocrystals

Another interesting form of Ga is Ga_xO_y nanocrystals with either a solid or porous framework. Oxidation of Ga nanoparticles anchored on a TEM grid under air at 200 ^{0}C led to the formation of thicker oxide shells, with smaller nanocrystals being completely oxidized (Figure 4.16). These particles do not appear to be hollow. In contrast, use of a chemical oxidant at the same temperatures led to formation of porous Ga_xO_y nanoparticles due to the Kirkendall Effect [157] and is particularly interesting as a potential metal oxide support for preformed Pt nanocrystals (Figure

4.17 b). In addition, physical mixtures of individual Pt and Ga nanocrystals can also be prepared for PDH studies.

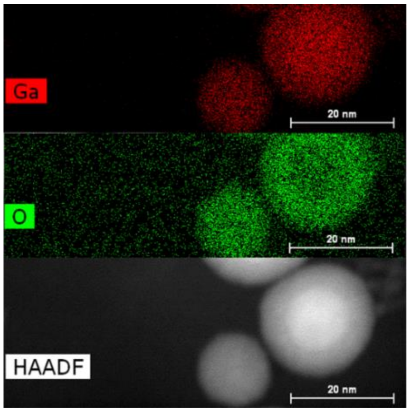

Figure 4.16. HAADF image of Ga nanoparticles heated in air at 200 ^{0}C and corresponding EDS

Another approach to synthesizing Pt-Ga nanocrystals systems is to deposit Pt onto preformed Ga or Ga_xO_y nanoparticles. In order for Pt to deposit onto the surface of the Ga, care must be exercised to avoid formation of the native oxide shell. In that case, only homogeneous nucleation and deposition of Pt was evident (Figure 4.17 d), with the Ga nanoparticles appearing to be almost completely oxidized in the process (native oxide is almost indistinguishable and overall contrast is lower). However, when the Pt deposition is done in a one pot growth without exposure to air, small Pt nanoparticles nucleate heterogeneously onto the surface of the Ga nanoparticles, leading to the formation of Pt-Ga dimer nanoparticles (Figure 4.17 c).

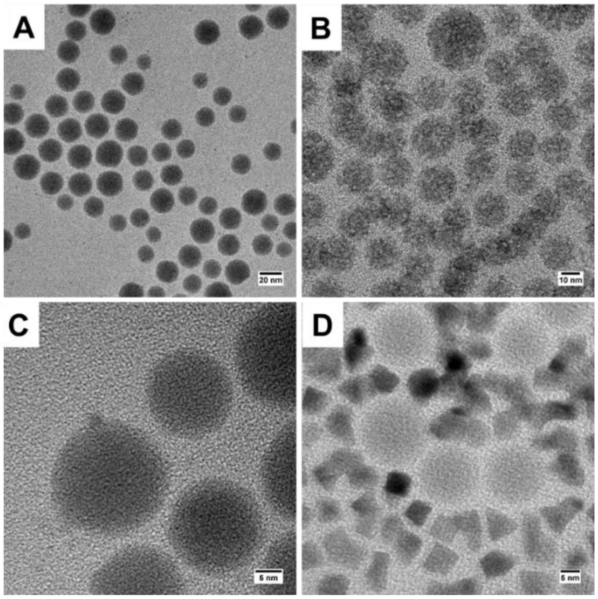

Figure 4.17. (A) Ga nanoparticles with a native oxide shell (B) Ga nanoparticles oxidized with TNO. Pt deposition onto Ga nanoparticles (C) without and (D) with initial native oxide shell

4.5 Conclusions

Colloidal synthesis of bimetallic systems comprised of a noble and non-precious metal is quite challenging. This can be mitigated through modulation of the non-precious metal precursor reactivity by varying the ligand on the metal center. Ga alkyl amide and silyl amide precursors were found to be more reactive than Ga precursors with electron withdrawing groups of chloride and acetylacetonate. Cyclic voltammetry and energy dispersive spectroscopy provided a qualitative trend of reactivity as: $Ga_2(NMe_2)_6 > Ga[N(Me_2)Si)_2]_3 > GaCl_3 \sim Ga(acac)_3$, where the Ga center in precursors with Ga-N bonds was neutral. Neutral local ligand environments of metal complexes gave higher incorporation of Ga, since the reaction is thought to proceed via decomposition instead of a co-reductive route. Also, bulkier ligand groups stabilize the metal center, making it slightly less reactive. These principles can be applied when choosing appropriate precursors for the synthesis of alloys consisting of a non-precious metal.

Initial attempts at size control via varying the ratio of OAc: OLAm, Pt^{II}: Pt^{IV} precursor, injection rate and temperature proved unsuccessful (Appendix A2.4, A2.5). These often resulted in a very broad or bimodal distribution of sizes. Furthermore, the compositional heterogeneity in Pt-Ga nanoparticles could be improved. One alternative synthetic strategy might be to develop bimetallic Pt-Ga precursors to achieve true simultaneous decomposition or co-reduction of individual elements in a stoichiometric fashion. Pt-Ga complexation was observed in Pt-Ga precursor injection solutions of benzyl after extended sonication (Appendix A2.7). Thus, it would be interesting to study the complexation behavior with different Pt: Ga ratios of precursors, and use the bimetallic product as a precursor to the direct synthesis of Pt-Ga intermetallic nanoparticles.

Another alternative and potentially quite interesting pathway to Pt-Ga nanoparticles is galvanic exchange reactions. The now established colloidal synthesis of Ga nanoparticles first reported by Kovalenko [152] opens the way for such interesting reactions. The biggest challenge of using galvanic exchange to access other alloy systems of noble and non-precious metal combinations might be the need to still develop monometallic nanoparticles of the non-precious metal, which then react with noble metal salts. Metal precursors lacking M-O bonds are particularly beneficial, as one does not have to worry as much about producing a metal oxide instead.

Chapter 5. Propane Dehydrogenation Activity of Pt-Ga Catalysts and their *In-situ* Structural Changes

5.1. Introduction

Very few studies have been reported on Pt-Ga catalysts for PDH [138]–[141]. Bell et al has studied a Pt catalyst on a hydrotalcite support, Mg(Al)(Ga)O, and found that the catalytic performance was strongly influenced by the Ga content in the starting support. The formation of a Pt -Ga alloy during reduction of the support at high temperatures was found to suppress coke formation and enhance the activity and selectivity. Marin et al. used time resolved *in-situ* XRD to study alloying between Pt and Ga on a Pt/Mg(Al, Ga)O and Pt/Ga_2O_3 catalyst to develop a rough picture of the structural changes which occur under experimentally relevant conditions. While Marin studied this alloying under consecutive isothermal reduction/oxidation cycles at 873 K, not every Pt-Ga alloy that formed was identifiable. Whether they were stoichiometric solid solutions or distinct stoichiometric phases remains unknown for most of the alloys formed. Multiple alloys were formed on the Mg(Al, Ga)O support, while a distinct stoichiometric PtGa was discernible on the Ga_2O_3. Significant partially-reversible segregation was also observed under oxidation cycles. Weckhuysen et al. studied the catalytic activity of Pt promoted Ga_2O_3 catalysts, and reported that synergistic effects between Pt and Ga result in a highly active and stable catalyst which gave 92.6% selectivity toward propene over a 14 day period on stream. He proposed, using ^{71}Ga NMR, that coordinately unsaturated Ga^{3+} species present in tetrahedral and octahedral coordination formed the active species.

It is evident from such studies that the Pt-Ga system holds much promise as a highly selective and stable PDH catalyst for commercial applications. As expected, dynamic structural changes in the Pt-Ga occur under different environments, but more work is needed to fully understand how catalysts containing Pt and Ga behave in relation to each other. This chapter discusses some initial *in-situ* observations for Pt-Ga characterized using synchrotron based techniques under experimentally relevant conditions.

5.2 PDH of Pt_3Ga supported on γAl_2O_3

5.2.1 Chemicals, Materials, and Equipment

Quartz beads (99.99 % SiO_2, 0.25 mm- 0.5 mm, purchased from Pyrosil), γ-Al_2O_3 (Sasol, Catalox SCCa 5/150, pore volume 0.4 ml/g, average particle size 90 μm, surface area 150 m^2/g), Gas Chromatograph (SRI Instruments 8610C), catalytic reactor (purchased from PID Eng & Tech, MA10000), glass wool, a ¼" tubular quartz cell (with ½" extremities and a 60 μm porous quartz frit in the middle), a quartz thermocouple sheath (3 mm outer diameter, 2 mm inner diameter) with one open end, thermal mass flow controllers (MFC; Bronkhorst, calibrated at 100 ml/min at 5 atm), five 3 mm outer diameter quartz tubes (3" long) with both ends sealed and a K-type thermocouple (1/16").

The commercial catalytic reactor is capable of reaching temperatures up to 1000 ^{0}C and pressures up to 50 bar. PDH chemistry was performed using a quartz cell and a thermocouple encased in a quartz sheath, to prevent exposure of the metal to any gases. The reactor was equipped with heated lines and an HPLC pump, so that liquids can be introduced as vapors. The temperature of the catalyst bed was measured using a quartz enclosed thermocouple embedded within. Furthermore, the temperature of the furnace wall was measured simultaneously to track any large fluctuations in temperature.

The GC is equipped with two 50 μL sample loops. The first sample loop goes to a packed column for separation of C1-3 analytes, after which the heavier molecules are separated on a Bond KCl alumina column. These products are then analyzed by a Flame Ionization Detector (FID). The second sample loop goes to a HayeSep A column for separation of light molecules, followed by a ShinCarbon column for permanent gases. These products are then analyzed by a Thermal Conductivity Detector (TCD) and FID/methanizer. The FID was calibrated using a universal gas standard for C1-C7 components. Carrier gases used were nitrogen and helium. Isothermal gas separations at 50 ^{0}C were employed as standard.

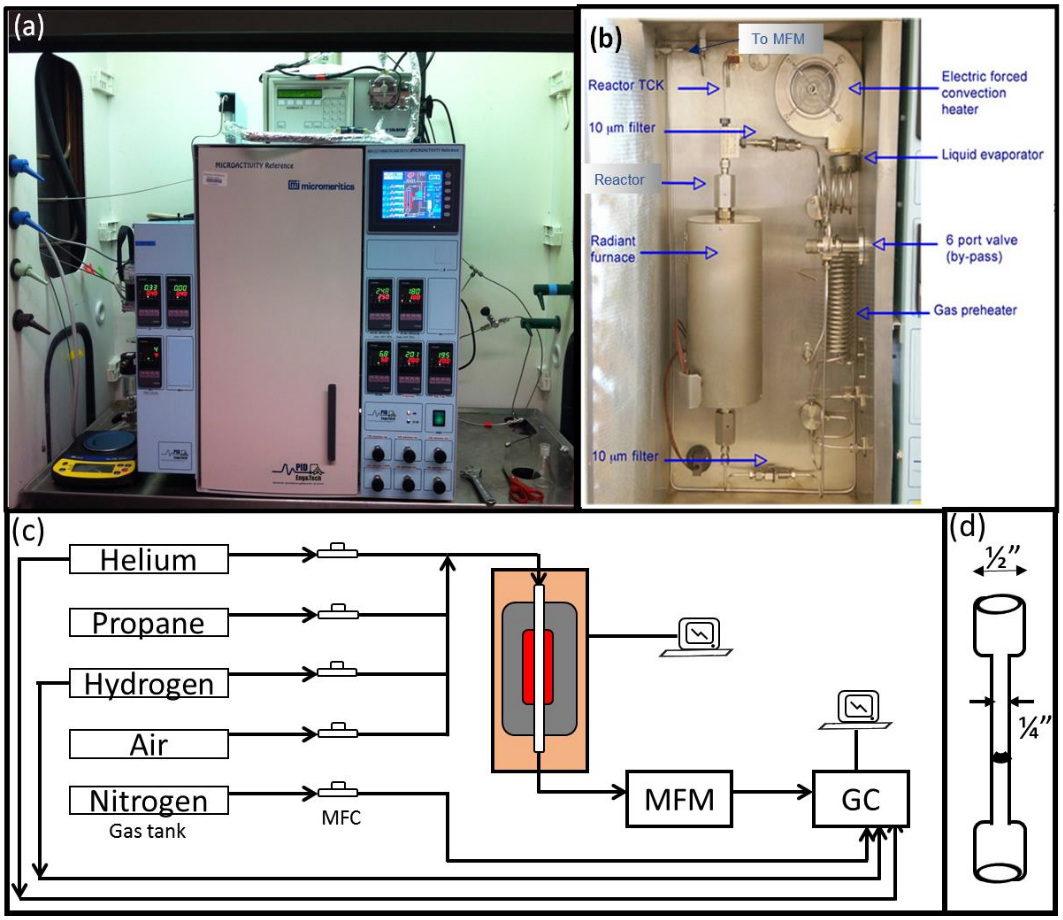

Figure 5.1 (A) Catalytic reactor housing and (B[1]) set up used for reactions. (C) Overall schematic of catalytic reactor system and gas chromatograph. Red region of furnace is hot zone around reactor cell (D) Tubular Quartz cell used for reactions

---

[1] Taken from user manual of Microactivity-Reference Reactor from PID Eng&Tech

All connections were made gas tight by using a nut on a reversed back ferrule, followed by a Viton O-ring, to make the quartz to Swagelok connections. All gas lines and connections were made with 1/8" stainless steel tubing. All flow rates used were 60 ml/min, except for the 20 % v/v C_3H_8/He mixture at 100 ml/min. All gases used for the reaction were purchased from Praxair at 5.0 ultra-high purity; extra dry grade air was used in place of oxygen. The set-up is illustrated in Figure 5.1.

5.2.2 Initial Catalytic Studies for Propane Dehydrogenation

Propane Dehydrogenation: Alumina supported catalyst was prepared by extensive sonication a dilute solution of nanoparticles with porous alumina for one hour or more, until the supernatant turned colorless. Then, the powder sample was dried overnight prior to use. The alumina supported Pt-Ga (< 2 wt. %) sample (60-70 mg) was diluted with quartz beads (0.25 – 0.5 mm) in a 3:1 (by mass) catalyst: beads and loaded into a ¼" tubular quartz reactor. The dead volume below the porous frit was filled using small 3" quartz tubes, and both ends of the tubular reactor were plugged with glass wool to trap any mobile particulates during the reaction. Gases were introduced into the reactor using the MFCs. Once the catalyst was loaded, the temperature was increased at a rate of 10 ^{0}C/min in He to 600 ^{0}C, then kept at that temperature for 10 minutes. Then, dry air was introduced for a mild oxidative pretreatment for 1 hour and the system purged in He for 1 hour thereafter. A 32.6 minute cycle of PDH was then performed, with continuous GC samplings every 6.01 minutes starting from 2.5 minutes into the PDH reaction. Following PDH, the sample was heated at a rate of 10 ^{0}C/min in He to 730 ^{0}C, then air introduced for 1 hour to combust coke deposits from the catalyst. After this cycle of regeneration was complete and confirmed by the absence of peaks from the GC, the sample was cooled to 600 ^{0}C in He and purged for 1 hour. Another 32.6 minute cycle of PDH was then performed with continuous GC samplings as before, and the entire process of PDH and regeneration was repeated several times with intermittent He purges. The propane conversion (X) and propene selectivity (S) were calculated based on the hydrocarbon product distribution (C1-C3 molecules measured by GC) according to the following equations:

$$X = \frac{moles\ of (CH_4 + C_2H_6 + C_2H_4 + C_3H_6)}{moles\ of\ (CH_4 + C_2H_6 + C_2H_4 + C_3H_6 + C_3H_8)} \times 100 \qquad (5.1)$$

$$S = \frac{moles\ of\ C_3H_6}{moles\ (CH_4 + C_2H_6 + C_2H_4 + C_3H_6)} \times 100 \qquad (5.2)$$

All values were normalized according to the carbon number in each product.

5.2.3 Discussion of Results

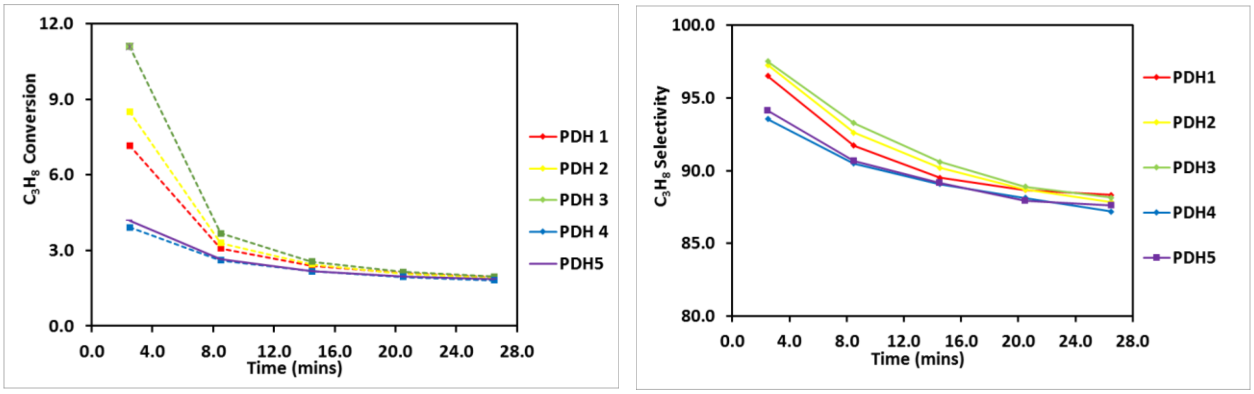

Figure 5.2. (A) PDH Conversion over Pt_3Ga supported onto γ-Al_2O_3 and (B) Propene Selectivity

The catalyst became more active in the first three cycles, presumably due to formation of gallia during the oxidative pretreatment, which is also active for PDH [158]–[161]. The initial conversion of 7.2 % increased to 8.5 %, then declined to 3.9 % after reaching a maximum of 11.1 %. After 8.5 minutes, the activity decreases by 57 %, 61%, 68% and 33 % for PDH1, PDH2, PDH3 and PDH 4 respectively (Figure 5.2A). One hypothesis for this could be that more gallia is formed after consecutive oxidative pretreatments due to segregation of Ga from the Pt-Ga alloy. This potentially creates more Ga^{3+} species, which has been proposed to constitute the active phase in gallia catalysts. Thus, the rise in activity could be because of the creation of these sites, but over time, deactivation occurs in part due to loss of some of these sites. Interestingly, the activity is markedly lower during the 4th PDH cycle, but the deactivation is not as rapid.

The Pt-Ga catalyst on alumina is quite selective towards propene production. The selectivity during the first 3 cycles of PDH is higher than the last 2 cycles overall. In PDH1, the selectivity starts at 96.5 %, then decreases to 91.7 % after 8.5 minutes and 89.5 % after 14.5 minutes. Subsequent cycles PDH2 and PDH3 have slightly higher values, but all three cycles converge to ~ 88 % selectivity after 32.5 minutes. Afterwards, the selectivity is slightly lower in PDH4 and PDH5, but converges to almost the same value near the end of a PDH cycle. (Figure 5.2B). These initial results show the promising catalytic performance of Pt-Ga alloys for PDH.

5.3 *In-situ* Ambient Pressure X-Ray Photoelectron Spectroscopy of Pt_3Ga supported on γAl_2O_3

5.3.1 Theory and Experimental Conditions

In conventional XPS, a monochromatic photon energy is used to excite core and valence electrons in a material (Figure 4.1). Electrons which overcome their binding energy and are ejected have a characteristic kinetic energy according to the following equation:

$$KE = h\nu - BE - \emptyset \qquad (5.3)$$

where hν is the input photon energy, KE is the kinetic energy, BE is the binding energy and ϕ is the work function of the analyzer. Typically, the anode choice is either a Mg Kα (1253.6 eV) or Al Kα (1486.6eV) x-ray source. XPS can be used to determine the concentration of elements near the surface, since each element has a unique set of core-level BE. The chemical shifts in binding energies can be related to differences in the oxidation state of the element, where a higher oxidation state is indicated by shifts to higher binding energies. The escape depth of the photoelectrons is limited to a few nanometers, since there is a high probability that the electron will interact with matter after being ejected, thereby limiting what is detectable. Electrons which originate within the first few nanometers from below the surface of a solid can escape without an energy loss. It is these electrons that produce signal with useful information, according to their kinetic energy. They are collected by a set of electrostatic and/or magnetic lens units, where the electrostatic field in a hemispherical analyzer allows only electrons of a certain energy to reach the detector.

In APXPS [162], electrons which are emitted can undergo elastic and inelastic collisions with gas molecules. The mean free path of an electron, λ_e, depends on its energy and gas pressure, with an inversely proportional relationship to the pressure. Thus, at 1 mbar, a 400 eV electron would only travel 4 mm before undergoing an inelastic collision. This distance reduces to 30 μm at 100 mbar, making it quite challenging to collect unscattered electrons, as their count rate (of those detected) decreases exponentially with distance. In order for APXPS to be realized, the distance an electron must travel in a high pressure region must be as short as possible. This challenge was overcome by the introduction of differential pumping. The sample is positioned near a small aperture at a distance $d \leq \lambda_e$ and the pressure on the other side lowered via this pumping to decrease the collision rate. Electrostatic lenses focus the electron trajectories into the apertures and allow for the detection of a higher fraction of electrons that would be lost otherwise. A window covered by a 100 or 50 nm membrane serves as the doorway for x-rays to enter without going into the x-ray source which is at ultra-high vacuum.

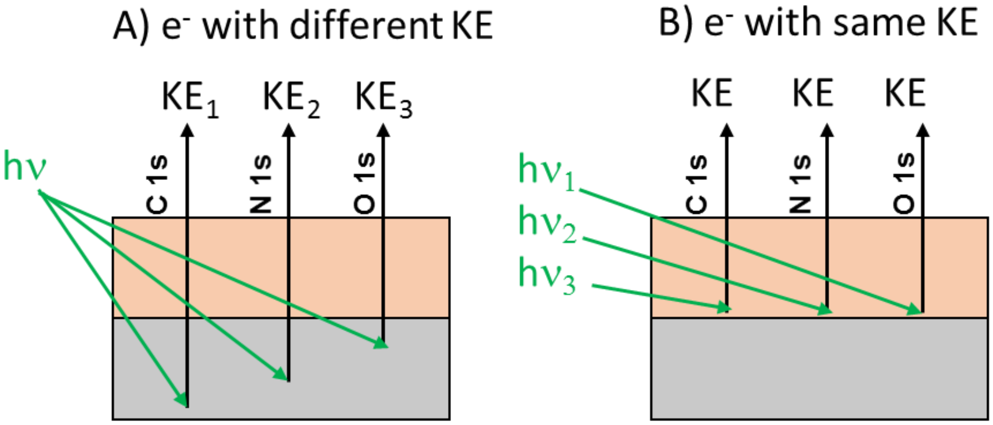

Figure 5.3. Kinetic energy of electrons using a (A) conventional x-ray source and (B) synchrotron radiation

This work was done on beam line 9.3.2 [163] at the Advanced Light Source, Lawrence Berkeley National Laboratory. Use of Synchrotron radiation as an x-ray source allows for a very high photon flux (up to 1.5 x 10^{11} photons/sec, orders of magnitude higher than Mg or Al anode) and high resolution imaging ($E/\Delta E < 10{,}000$) with 16 μm spatial resolution. Furthermore, the energy of the incident photon can be tuned to target photoelectrons from the same escape depth (same kinetic energies), as seen in Figure 5.3. A silicon wafer was coated with 50 nm Al_2O_3 using atomic layer deposition. Then, 3:1 Pt:Ga nanoparticles (synthesized using GaAc) were dip coated (~20 % coverage) onto the Al_2O_3, followed by a < 1 nm discontinuous layer of SiO_2 using an e^- beam evaporator (Figure 5.4). The overall architecture of the substrate was chosen to better imitate a core-shell configuration of SiO_2 coated Pt-Ga alloy nanocrystals supported onto an alumina support.

The substrate was placed on a holder equipped with a ceramic coated button heater and brought up to 600 ^{0}C under vacuum. Then, 50 mtorr of H_2 was introduced into the chamber, followed by 50 mtorr of C_3H_8. The Pt 4f, Al 2p, Si 2p, Ga 3d, C 1s, O 1s and Pt 4f regions were monitored throughout each condition, which was maintained for about one hour. The ratio of the Pt 4f and Ga 3d regions were used to determine the % atomic concentration of Pt and Ga in the top surface of the nanoparticles. Normalizations based on the sensitivity factors of Pt 4f and Ga 3d, 4.4 and 0.31 respectively, as well as the x-ray flux after a Shirley background subtraction were performed. A depth profile was created by choosing photon energies that produced photoelectrons from the same escape depth. The inelastic mean free path (IMFP) of the electrons was calculated using the online IMFP calculator from the NIST standard reference database. Additional details regarding the design of this beam line are described elsewhere.

All data were analyzed using the CasaXPS software. Representative deconvolutions of raw data for the Pt 4f and Ga 3d spectra prior to calibration vs the Al 2s are shown below in Appendix A2.8. The energy splitting due to spin orbit coupling of the Ga 3d region was quite small (0.45 eV) and unresolvable. A table of simulated IMFP of electrons in Pt_3Ga using the NIST IMFP calculator is included in the appendix, Table A2.1.

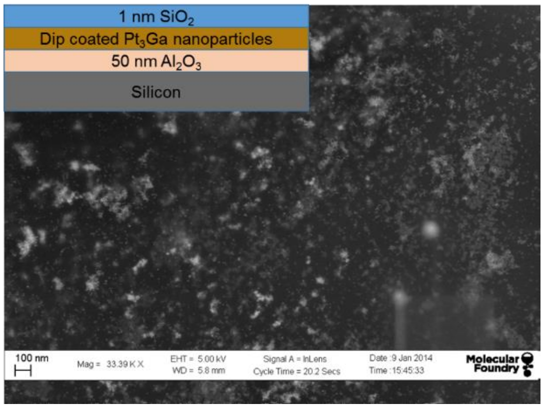

Figure 5.4. SEM of silica coated Pt_3Ga nanoparticles on alumina coated silicon substrate

5.3.2 Discussion of Results

The Ga 3d region (Appendix A2.8) was monitored using a photon energy of 330 eV when cycling from vacuum to hydrogen to propane to determine what structural changes occur in the first few angstroms from the surface (Figure 5.5 A). Once under a propane environment, the Ga 3d region was monitored using a photon energy of 560 eV, then 790 eV to create a depth profile of the Pt-Ga catalyst (Figure 5.5 B). Similarly, the Pt 4f region was monitored at a photon energy of 370 eV under the different environments, then with energies of 600 eV and 790eV for a depth profile analysis under a propane environment (Figure 5.6 A and B respectively).

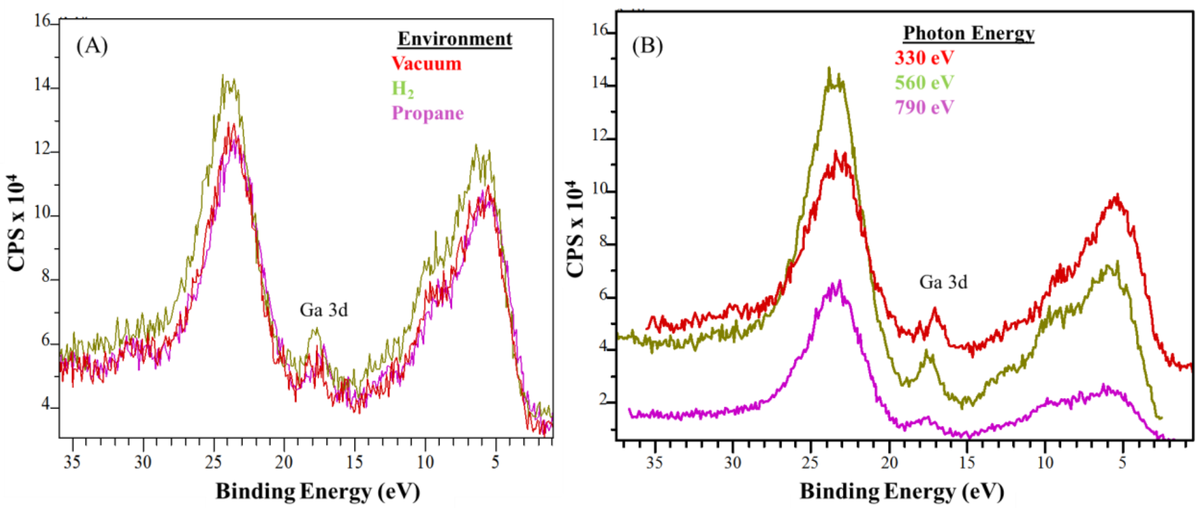

Figure 5.5 Ga 3d spectra under different (A) environments and (B) photon energy (depth profile)

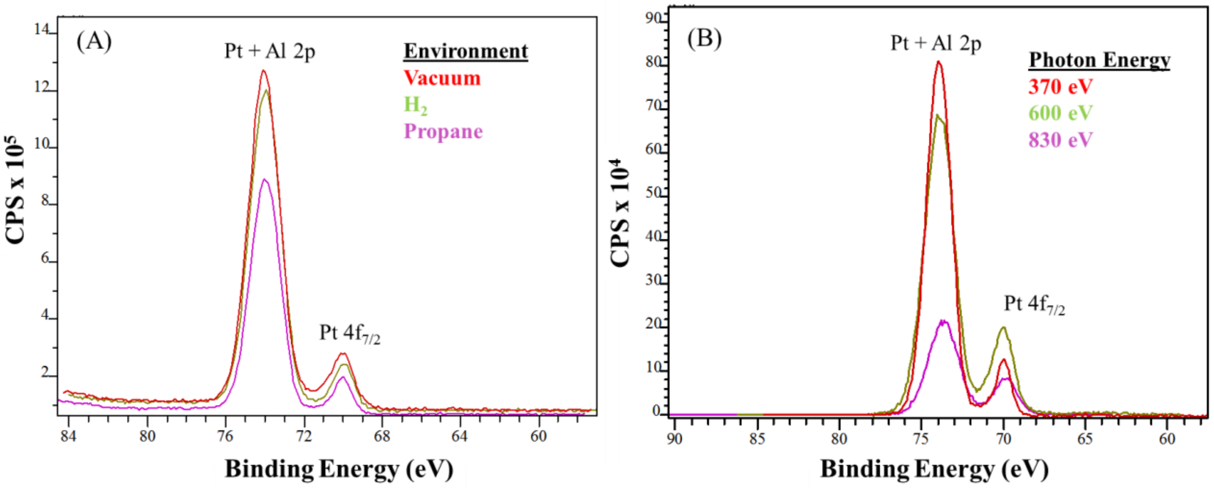

Figure 5.6 Pt 4f spectra under different (A) environments and (B) photon energy (depth profile)

The % atomic Ga determined from XPS can be plotted relative to the condition being tested. In Figure 5.5 A, a Ga enrichment on the surface is seen as the system is exposed to hydrogen followed by propane. A depth profile analysis reveals a decrease in Ga content as when probed deeper within the nanoparticle (Figure 5.5 B).

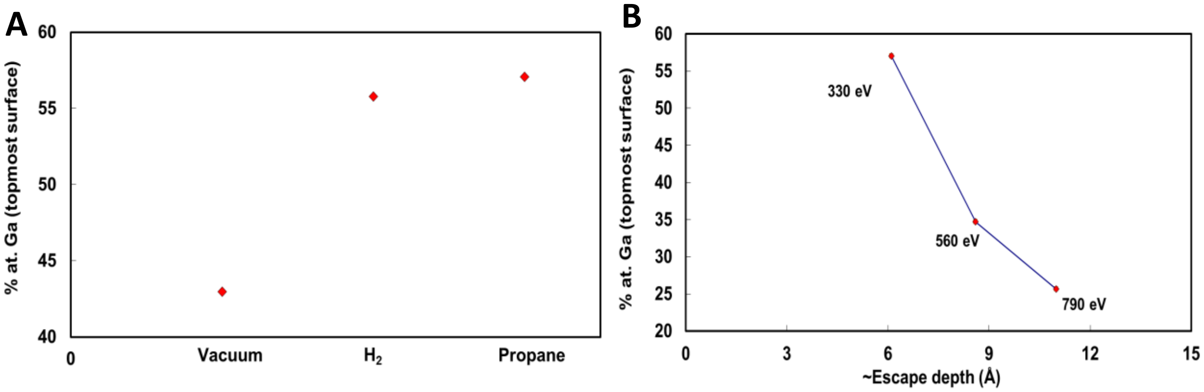

Figure 5.7. (A) Surface Ga enrichment under different environments and (B) a depth profile analysis of the Ga content

Initial APXPS analysis reveals a Ga enrichment at 600 ^{0}C to 43 % in vacuum, followed by a further enrichment to 56 % under hydrogen, which increases by about 1 % more under propane. A depth profile analysis reveals that the Ga content gradually decreases from 57 % on the topmost layers to 26 % at a 1.1 nm depth into the particle. The binding energy of both the Pt 4f and Ga 3d stayed relatively the same when cycled from vacuum to hydrogen to propane so it was difficult to ascertain whether or not any oxidation or reduction of either species occurred. Pt seemed to be fully reduced under each environment but any changes in the oxidation state of Ga remain unclear. XPS showed a very minor red shift of ~0.2 eV of the Pt 4f peak when probed 1.1 nm into the particles. While charge transfer from Ga to the Pt is quite possible, it is difficult to claim so definitively based on this small shift. A minor blue shift of ~0.5 eV was seen in the Ga 3d region when the probe depth increased to the top 0.9 nm of the particles, further suggesting charge transfer from the Ga to Pt occurred. Thus, Ga near the surface of the nanoparticle is speculated to exist more as segregated Ga rich islands, which gradually transform to a Pt richer alloy environment deeper into the particles. This would indicate a lower surface energy for Ga under these conditions.

5.4 *In-situ* X-ray diffraction of Pt_3Ga supported on SBA-15

5.4.1 Experimental Set Up

A 9 wt.% 3:1 Pt:Ga supported on SBA-15was prepared. This was carefully loaded into a 1.5 mm diameter glass capillary to prepare a 3 cm catalyst bed. The catalyst bed was tightly packed such that the sample would not be expelled upon exposure to flowing gas or be too compressed such that gas could not flow through. A small roll of glass wool was inserted in both ends of the capillary to form a plug that would trap any mobile particulates. This is illustrated in Figure 5.8 below. The glass capillary was typically ~ 8 cm in length. The system was made gas tight using the back ferrule and Viton O-ring combination previously described for glass to Swagelok connections. Once the sample was prepared, it was mounted onto a steel block and held in place by some hollow alumina tubes (inserted beneath the nut and above the metal block, Figure 5.8). A 1/8” piece of plastic tubing was used at the immediate end of the inlet and outlet, to stabilize the capillary and avoid use of more rigid stainless steel (SS) tubing, which would shatter the capillary with the slightest displacement. A transition was made to 1/8" SS tubing following the ½ foot of plastic tubing, Gas was introduced into the system using thermal mass flow controllers to deliver 20% O_2/Ar, pure Ar and a 2.4 % C_3H_8 /Ar mixture. The sample block was heated to 400 ^{0}C using embedded heating rods within at a rate of 10 ^{0}C/min under pure Ar. Then, 20% O_2/Ar was flowed for 15 minutes (mimic a pretreatment), followed by a 10 minute purge in Ar. A 2.4 % C_3H_8 /Ar mixture was then flowed for 20 minutes, followed by another Ar purge and a 15 minute treatment in 20% O_2/Ar to mimic a regeneration cycle. The reaction was then cooled to room temperature (RT) under Ar.

This work was done on beam line 12.2.2 [164] at the Advanced Light Source, Lawrence Berkeley National Laboratory. The detector used was a Perkin Elmer CMOS with an x-ray spot size of 30 x 30 μm (FWHM). This beam line has a flux of 1.9 GeV, 500 mA (1 x 10^{11} photons/sec into 10 μm FWHM beam spot size) and an energy resolution (E/ΔE) of 7000. A Si [111] crystal was used to tune the wavelength energy. A 25 keV x-ray energy (0.497326 Å) was used as the source. An exposure time of 30 seconds every 1 minute was used to collect data throughout the experiment. No diffraction peaks were observed on a spot outside of the sample. All data work up was performed using the Fit2D software and parameters were selected based on a calibration with LaB_6. Raw data was fit to a Voigtian, and selected snapshots prior to fitting are shown in the Appendix A2.9.

It should be noted that direct temperature control of the sample was impossible under the current design (adapted from the Somorjai group, Figure 5.8), thus the exact temperature of the catalyst bed was unknown. Rather, the temperature of the heating block was tracked over time and as different gases were flown through the system. While higher temperatures are typically required for appreciable C_3H_8 conversions, we were limited by our equipment in the maximal achievable temperature and had to use very dilute gas mixtures for safety reasons.

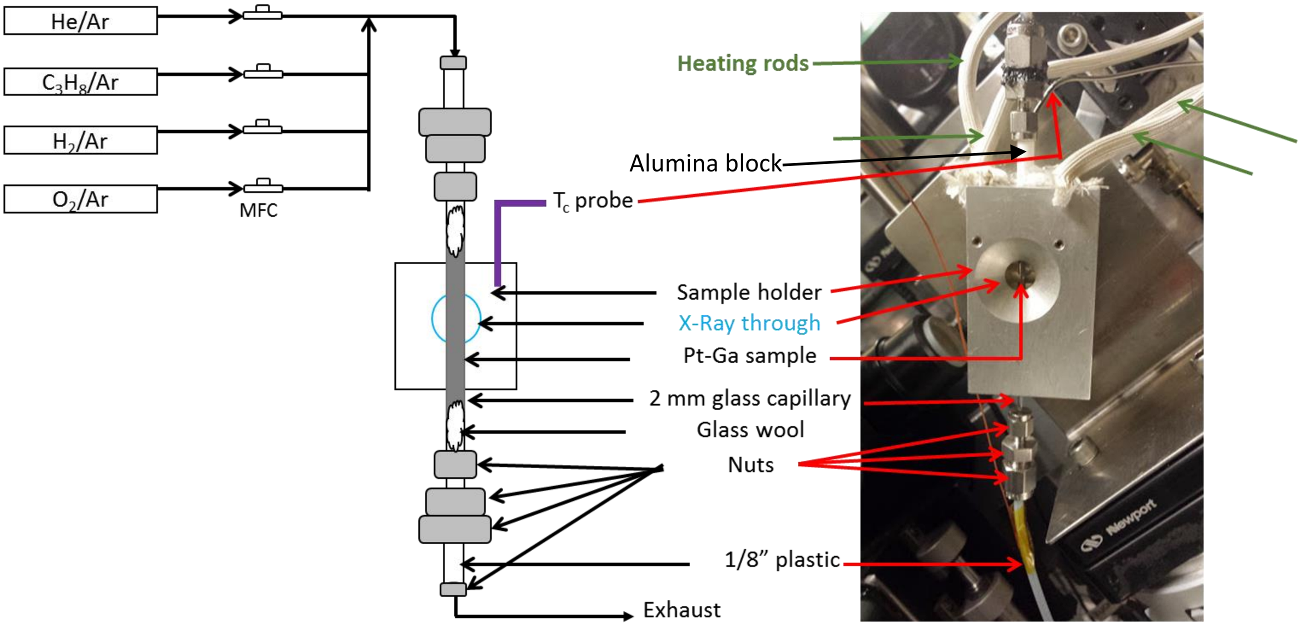

Figure 5.8. Experimental set up for performing in-situ XRD experiments at beam line 12.2.2

5.4.2 Discussion of Results

The raw data at selected times during the reaction are shown as an example in the appendix, A2.9. XRD scans taken after a 30 minute exposure show the growth and emergence of several peaks. After working up the raw data in the Fit2D software, XRD scans as a function of 2θ can be obtained. Representative example spectra are shown in Figure 5.9 below.

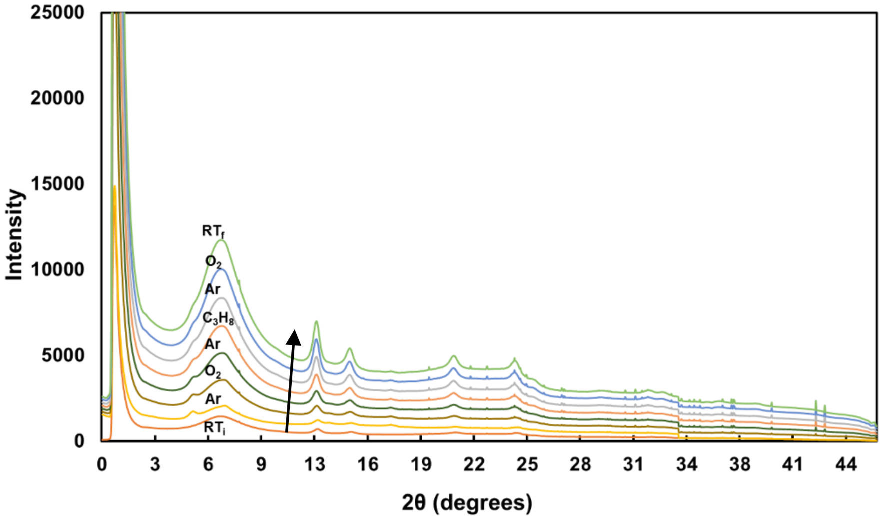

Figure 5.9. XRD spectra taken under different environments

The changes in d-spacing are compiled into a single plot (Figure 5.10) to observe the structural changes which occurred under each environment. The pink plot represents the XRD scan taken at 50 ^{0}C, followed by a scan (red) taken at the end of the heating ramp to 400 ^{0}C in argon. By this time, a diffraction peak at 3.5 Å is present, suggesting a new Pt-Ga phase of unknown composition and structure has formed. Next, a scan (green) is taken during the first 30 seconds of exposure to oxygen, followed by another scan after 8 and 11 minutes. This feature at 3.5 Å is unstable, as it disappears within the first few minutes of oxidation. When the sample is purged with argon, another scan is taken after an exposure of 30 seconds and 9.5 minutes in this atmosphere. At this time, a decrease in the d-spacing is observed and held fairly constant after 30 seconds of exposure to propane (first data point in blue). Subsequent scans in propane after 5, 11 and 19 minutes show an eventual reversal of the d-spacing to that seen at the end of the oxidation pretreatment, starting at 11 minutes. Furthermore, the peak seen at 3.5 Å reappears (third data point in blue) and persists 30 seconds into the subsequent argon purge (first red data point after PDH). This peak is no longer observed after 5 minutes under argon and never reappears throughout later scans. A regeneration cycle in air was performed following PDH, accompanied by 30 second scans under oxygen after 30 seconds and 8 minute exposures. The sample was finally cooled in Argon at the end of this regeneration, with a final scan (black) taken at the end at room temperature.

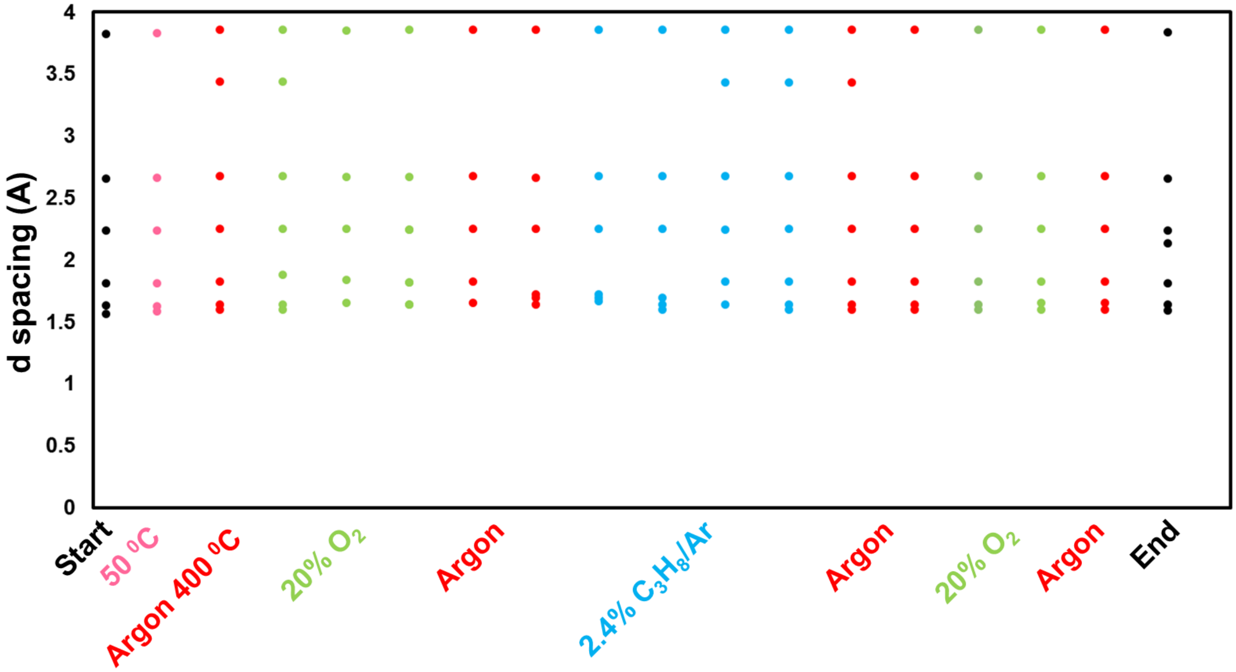

Figure 5.10. Change in d-spacing mapped out under different gaseous environments. The first and last scans (black) are at room temperature.

Lattice expansion due to thermal heating of the crystal accounts for very minor shifts in the d-spacing. However, distinct and somewhat transient new features are seen when the sample is heated under Argon, and again during PDH. A comparison of the FWHM used to calculate the crystallite size according to the Scherer formula revealed the initial crystallite size at room temperature was 11.3 nm, but increased to 24.8 nm at the end. The FWHM was already half its initial starting value by the time the temperature got to 400 ^{0}C under argon. This peak narrowing is attributed to sintering of the nanoparticles, as further proven by TEM (Figure 5.11). A unique peak grows in toward the end of the experiment at 2.14 Å (Figure 5.12). The initial peaks at 3.8 Å and 2.6 Å match the Pt_3Ga (100) and Pt (111) respectively, while the feature at 2.14 Å cannot be confidently assigned to a particular phase of Pt-Ga. Possible assignments for this peak include Pt_5Ga_3 (311) and α-Ga_2O_3 (113). These results are similar to that reported by Marin [165], who although able to observe new Pt-Ga alloy formation under oxidation and reduction was unable to assign each new feature to a specific Pt-Ga phase.

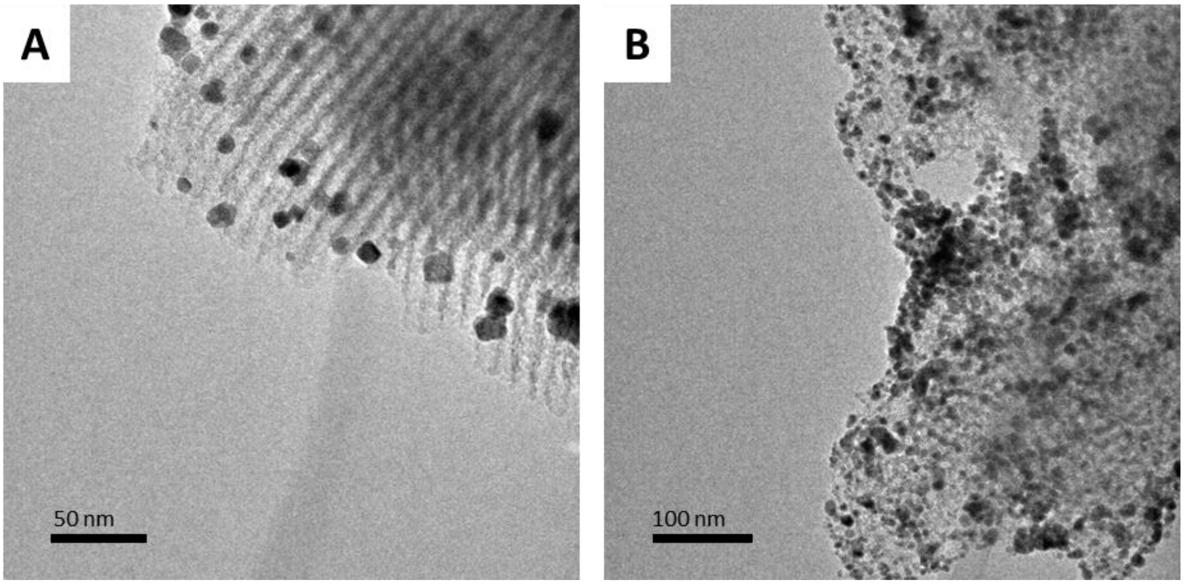

Figure 5.11 Pt_3Ga supported on γ-Al_2O_3 (A) before and (B) after heating

Figure 5.12 shows a transient feature around 3.4 Å which seems to appear and reappear at different times. This could be an indicator of $PtGa_2$ (111). Since the actual temperature of the catalyst bed was unknown, it is difficult to make any solid conclusions from red shifting d-spacing. However, it is clear from this initial study that segregation and alloying occurs under experimental conditions, some of which are unique to propane. The alloys formed *in-situ* don’t seem to be stable, as they are not permanent features. Possible assignments of the peaks observed at the start and end of the reaction are described in the Appendix Table A2.2.

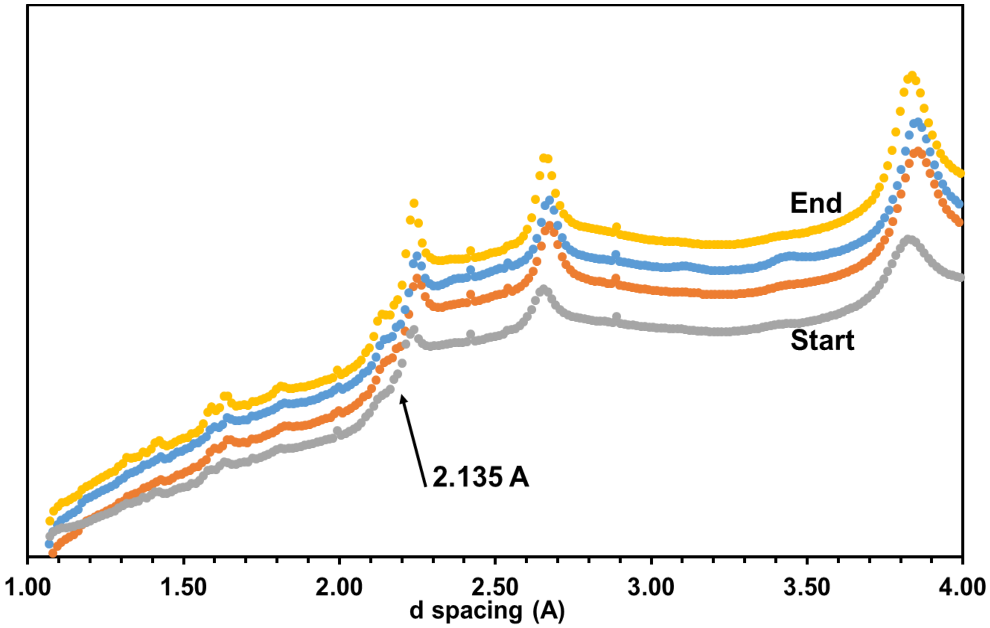

Figure 5.12. Unique and transient features seen under the different gases as a function of the d spacing. The orange and blue lines represent 6 and 12 minutes under a C_3H_8 environment. The start and end scans were taken at room temperature under Ar. The feature around 2.14 Å grows in and the one at 3.4 Å is transient.

5.5 Conclusions

It is very clear that surface and structural changes occur under experimental conditions. The transient nature of some of these changes were seen in the in-situ XRD work, where new peaks appeared, disappeared, and then reappeared under different environments. Furthermore, surface segregation was observed in the in-situ APXPS work. Both changes are expected to impact the catalytic behavior of the catalyst, and more experiments are needed to fully understand this effect. This preliminary work leaves many interesting questions yet to be answered regarding the active phase of the Pt-Ga alloy catalyst. Synchrotron based characterization techniques will prove quite useful in building in mechanistic picture of what happens to the catalyst during the first moments of PDH and thereafter in the long-term.

As expected, sintering was observed, as the crystallite size determined from XRD more than doubled by the time the reaction temperature was reached. Thus, it is imperative that these alloy nanocrystal catalysts be fully encapsulated by a porous oxide shell, as prior work has shown the thermal stability of such core-shell nanoparticles is greatly improved. This chemistry is sensitive to the ligands on the nanocatalysts, and future work involves the optimization of this oxide shell coating procedure using conventional sol-gel chemistry. Initial silica coatings have already been prepared according to established protocols (Figure 5.13) [166].

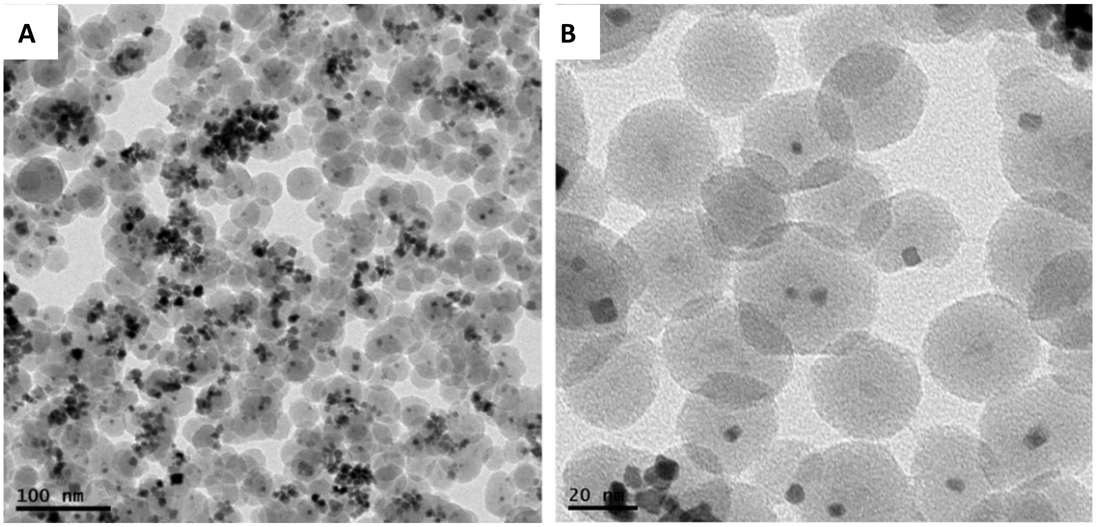

Figure 5.13. Silica coated Pt_3Ga nanoparticles (synthesized using GaAc)

Chapter 6. Concluding Remarks

As the sea of nanocrystal building blocks with superb control over the size, morphology and composition continues to rise, endless opportunities in catalysis, solar energy conversion, electronic devices, optics and biomedical fields continue to be realized. These versatile, tunable building blocks are now frequently assembled to create sophisticated nano-architectures in a modular fashion. This work discussed several conditions under which different sequential growth modes are favoured and why particular attention must be given to the nanocrystal surface prior to these depositions. CdSe/CdS nanorods can be modified with metal nanocrystals at different locations. In this work, the stability of the nanocrystal seed played a crucial role in accessing higher order architectures of Ru-CdSe@CdS-Pt nanorods. This important fact will no doubt spur the creation of more advanced nanoheterostructures, as ligand induced degradation of individual components within a nanoparticle is most likely a more often than not occurrence. Colloidal nanocrystal synthesis will continue to evolve as a useful, versatile tool in nanoparticle synthesis.

Accessing alloy nanocrystals comprised of a noble and non-precious metal can be a formidable challenge. Strong reducing agents might achieve co-reduction of all metal precursors, but at the expense of nucleation and growth kinetic control. The local ligand environment can greatly impact the reactivity of the precursor. Thus, non-precious metal precursors with neutral ligand environments might be better suited for alloying with noble metals. Alternatively, bimetallic precursor formation and decomposition can give added compositional control in the resulting alloy. Simultaneous co-reduction is difficult and thermal decomposition routes require appropriate precursors be selected. Ga alkyl amide and silyl amide precursors were found to be more reactive than Ga precursors with electron withdrawing groups of chloride and acetylacetonate. This is attributed to the Ga-N bonds, which readily decompose at high temperatures. This work examined the compositional heterogeneity of Pt-Ga alloys synthesized with different Ga precursors. Future structure-activity relationships in catalytic reactions should be quite interesting.

Appendix

1. Pt-Sn synthesis and Characterization

Pt-Sn nanoparticles were synthesized using a modified protoccol originally developed by Olesiak, as previously described for Pt-Ga alloys but using tin (II) acetylacetonate as the Sn precursor. TEM images were taken on a 200kV LaB_6 FEI Tecnai G2 20 using Pt-Sn nanoparticles drop casted onto a lacey carbon grid. HRTEM, HAADF-STEM and EDS point spectra/line scans were taken on a JEOL 2100F at the Molecular Foundry using 10 second exposures at 120 kV at the Pt M (red) and Sn L (green) edges. Rietveld Refinement was performed using the Materials Analysis Using Diffraction (MAUD) software.

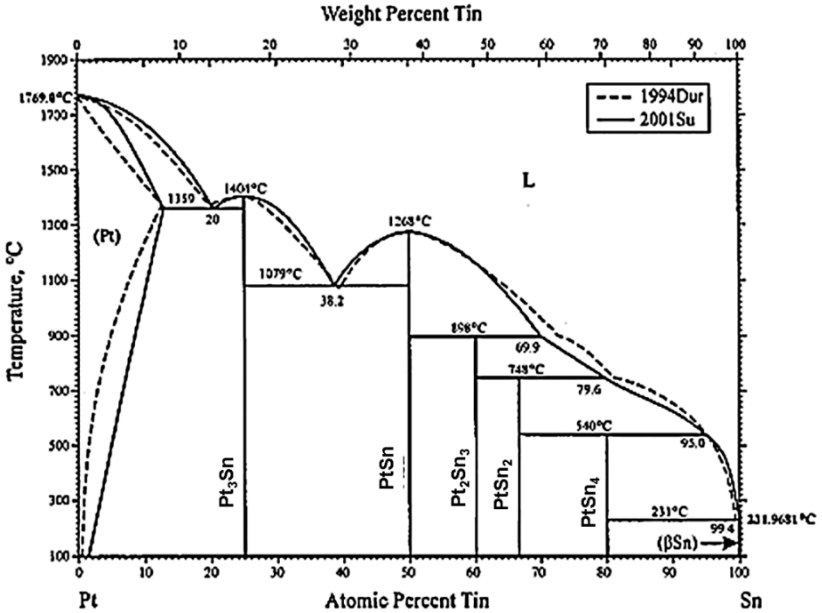

A1.1 Phase Diagram of Pt-Sn

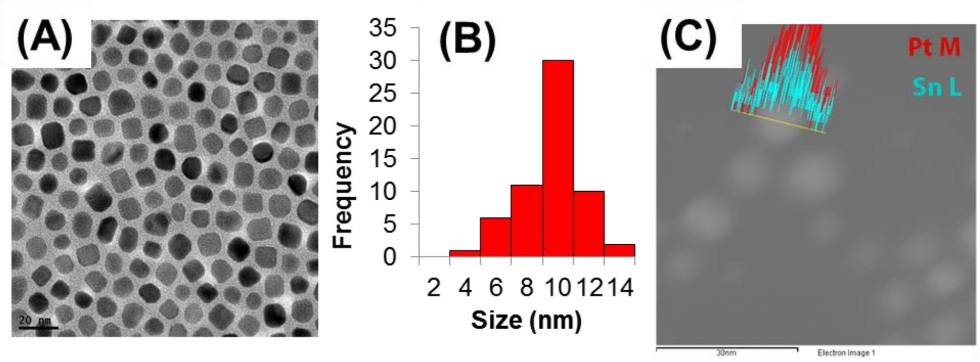

A1.2 (A) TEM and corresponding (B) size distribution and (C) HAADF of Pt_3Sn nanoparticles. EDS line scans in (C) reveal a homogeneous alloy of average % atomic Sn 24.1 ± 1.1. This σ is solely based on particle heterogeneity for a few particles and excludes from the σ fitted spectra.

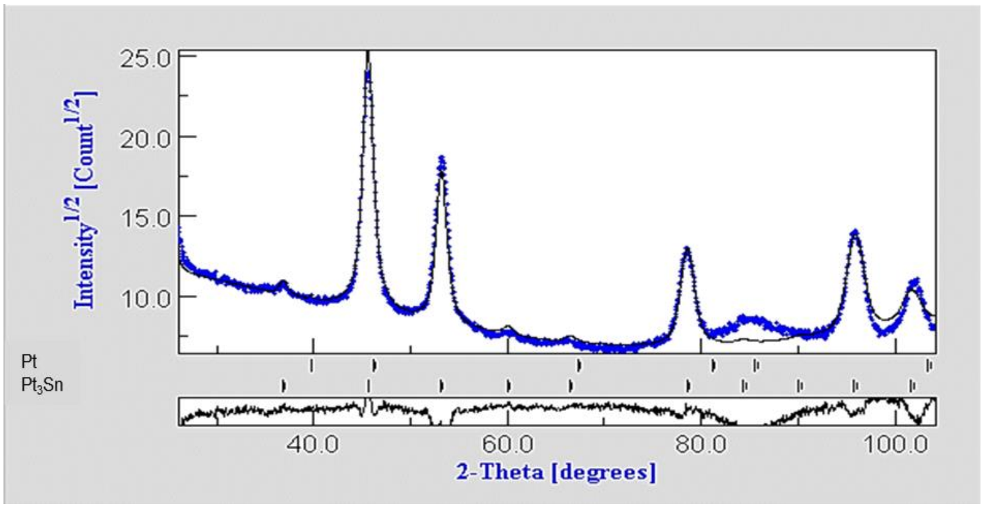

A1.3 Rietveld Refinement of Pt_3Sn nanoparticles reveals a 99.2 ± 0.0 wt. % Pt_3Sn and 0.8 ± 0.8 wt. % Pt. The goodness of the fit was shown by a σ of 0.93 and Rw 9.54 %.

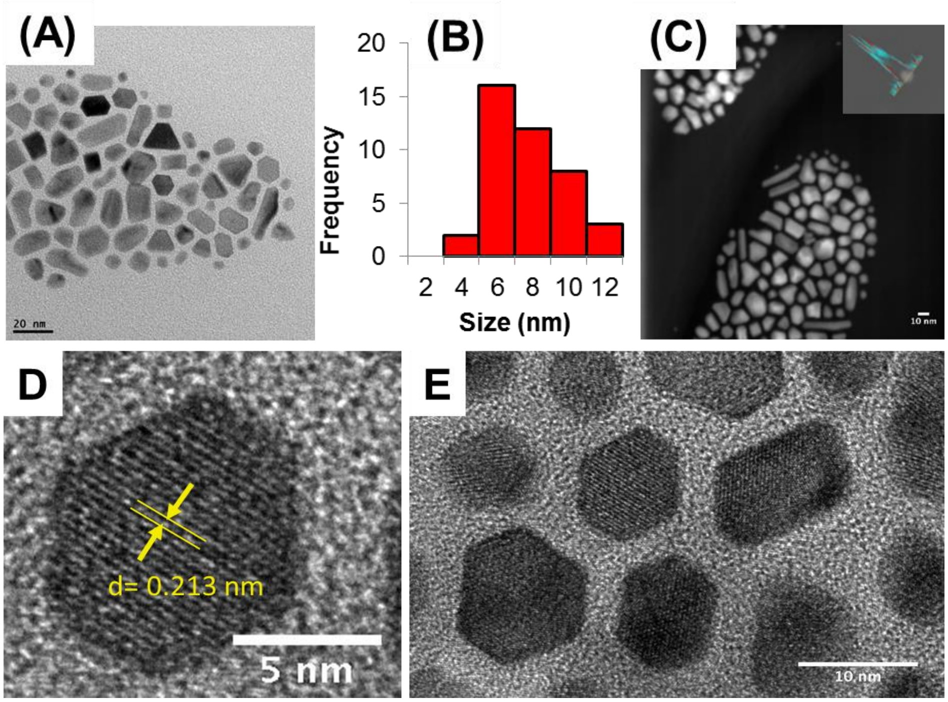

A1.4 (A) TEM of PtSn nanoparticles and (B) corresponding size distribution. (C) HAADF image and EDS line scan (inset) of a PtSn nanoparticle (D, E) HRTEM of PtSn nanoparticles. EDS reveals a homogeneous alloy of an average atomic % Sn 56.1 ±1.4. This σ is solely based on particle heterogeneity for a few particles and excludes from the σ fitted spectra.

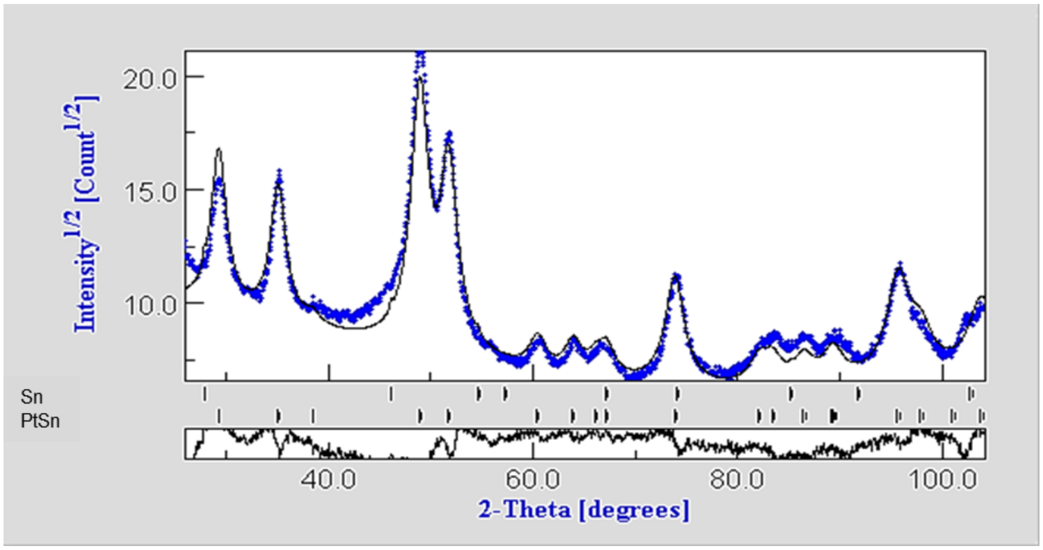

A1.5 Rietveld Refinement of PtSn nanoparticles reveals a 99.6 ± 0.0 wt. % PtSn and 0.4 ± 0.15 wt. % Sn. The goodness of the fit was shown by a σ of 1.04 and Rw 10.45 %.

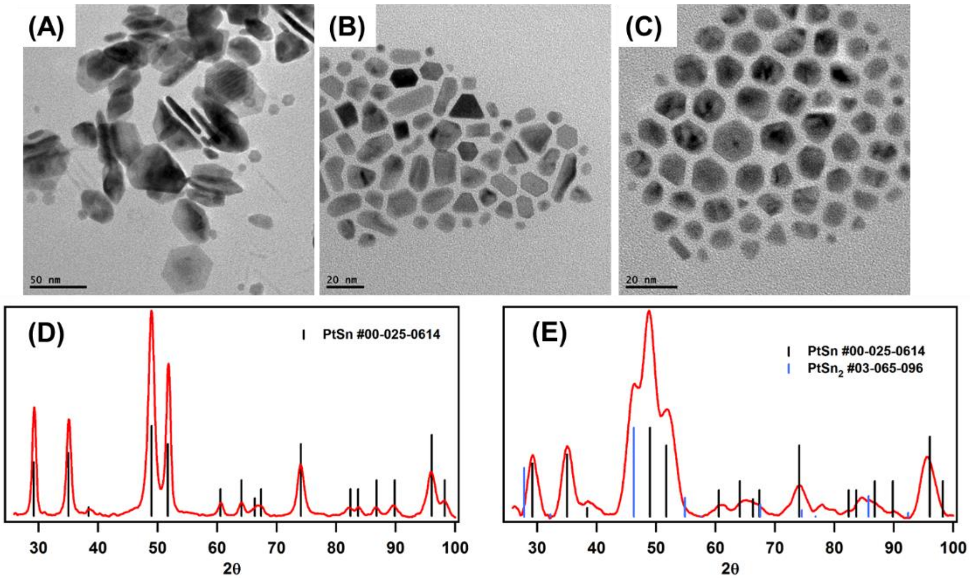

A1.6 TEM of PtSn nanoparticles with different OAc: OLAm. (A) 1:3 (B) 1:1 (C) 3:1 and XRD of PtSn with excess (D) OLAm and (B) OAc. Reference PDFs are listed for each XRD.

As A1.2 and A1.4 show, the PtSn nanoparticles have a variety of shapes, in contrast to the Pt_3Sn which has a cubic instead of hexagonal crystal lattice. On average, PtSn nanoparticles had a diameter of 6.68 nm ± 1.97 nm for smaller hexagonal nanoparticles. Elongated PtSn nanoparticles varied from 13-30 nm in length, and larger hexagonal nanoparticles varied from 10-13 nm wide. Pt_3Sn displayed primarily cubic and quasi-spherical shapes, with a minor portion of tetragonal nanoparticles. The cubic particles had an average diameter of 8.62 nm ± 1.87 nm. HRTEM of the PtSn showed lattice fringes of 2.13 Å, matching the PtSn (102) reflection. Individual EDS line scans of the PtSn indicates ~ 56 % atomic Sn is present, presumably due to surface Sn enrichment, while Pt_3Sn nanoparticles contain ~ 24 % atomic Sn. A homogeneous distribution of Pt and Sn was observed in these particles, as proven by the individual line scans.

Bulk XRD patterns indicate a hexagonal crystal structure for PtSn and a cubic structure for Pt_3Sn, as expected. The Rietveld Refinement for these samples (A1.3 and A1.5) suggests phase purity, with over 99% of the composition indicating an intermetallic Pt-Sn structures. The discrepancy at $2\theta = 85^0$ for Pt_3Sn could be due to a number of factors, such as a poor background or low signal. Reference pdf files for PtSn, Pt_3Sn and Pt were #00-025-0614, #00-035-1360 and #00-004-0802 respectively.

Initial attempts to achieve size controlled Pt-Sn nanoparticles were unsuccessful. For the case of PtSn, different ratios of $Pt^{(II)}/Pt^{(IV)}$ were used by addition of $PtCl_4$ and the OAc:OLAm ratio was varied. In each case, polydisperse samples resulted. Ligand stabilization is important for controlling both the nucleation and growth kinetics. Excess oleic acid may give rise to Sn or Pt-oleate formation, which can reduce the nucleation rate and produce less nuclei, leading to larger particles, as seen in A1.6 c. Oleylamine can be used as a solvent, reductant or to selectively bind to certain facets. Here, excess oleylamine produced discs or plates, some of which are hexagonal, as seen in A1.6 a. XRD patterns of PtSn nanoparticles made with excess oleylamine indicated a hexagonal crystal structure (A1.6 d), while excess oleic acid indicated both PtSn and $PtSn_2$ were present (A1.6 e).

2. Pt-Ga Characterization

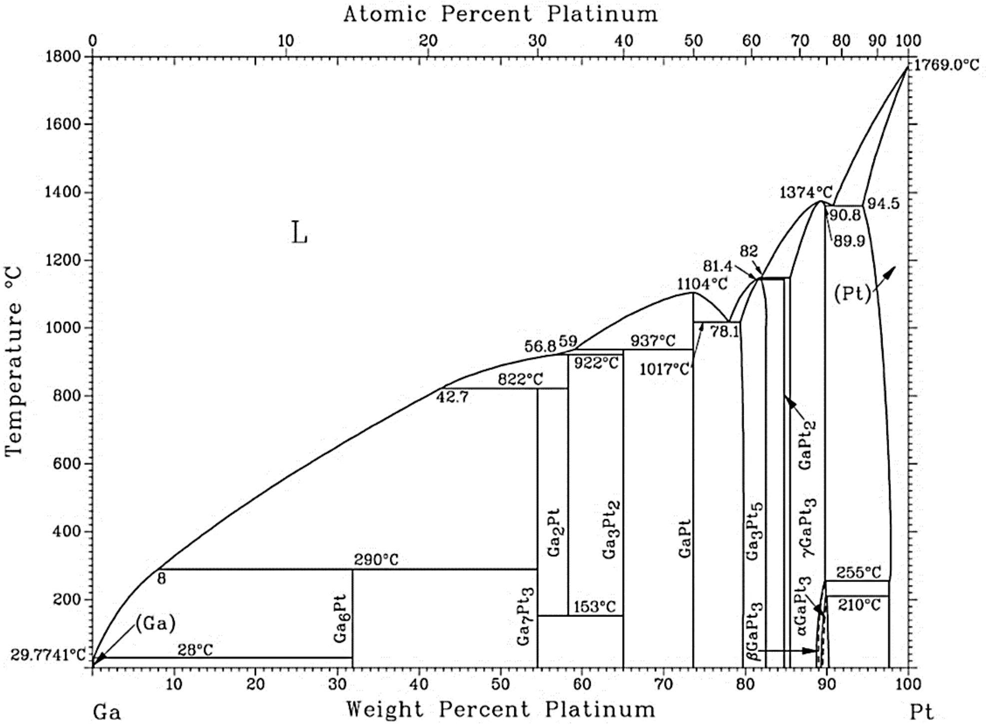

A2.1 Phase Diagram of Pt-Ga

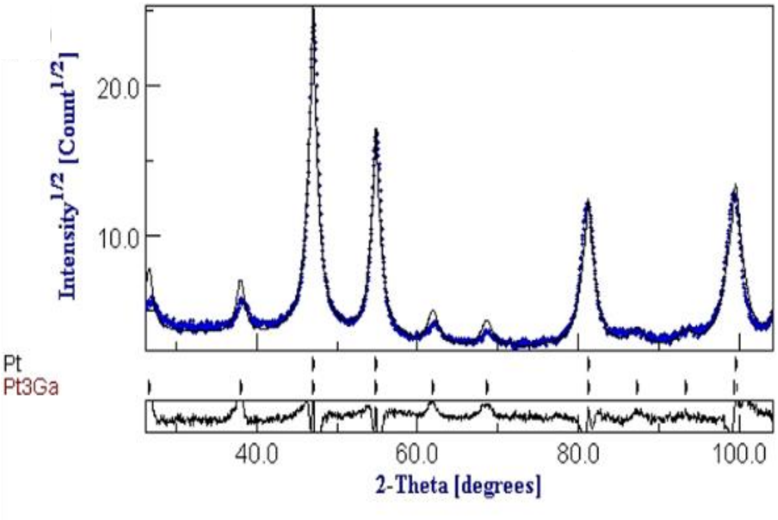

A2.2 Rietveld Refinement of 3:1 Pt:Ga nanoparticles (GaAc) reveals a 89.8 ± 0.0 wt. % Pt_3Ga and 10.2 ± 0.7 wt. % Pt. The goodness of the fit was shown by a σ of 1.17 and Rw 20.16 %.

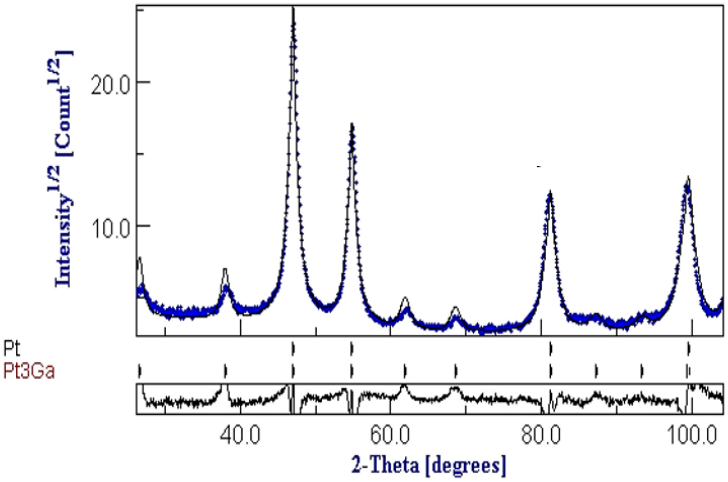

A2.3 Rietveld Refinement of 3:1 Pt:Ga nanoparticles ($GaCl_3$) reveals a 98.0 ± 0.1 wt. % Pt_3Ga and 2 ± 0.3 wt. % Pt. The goodness of the fit was shown by a σ of 2.39 and Rw 11. 56%.

A Rietveld Refinement (A2.2) of for 3:1 Pt:Ga using GaAc showed ~90 % of the alloy was Pt_3Ga, and ~10% was Pt, which yields an estimated Pt weight of 90% and 10% Ga. A Rietveld Refinement (A2.3) of 3:1 Pt:Ga using $GaCl_3$ showed ~2% of the alloy was Pt_3Ga, and ~98% was Pt, which yields an estimated Pt weight of almost 100%. Initial attempts at size control by varying the concentration of oleic acid and oleylamine were unsuccessful. A2.4 shows how changing the ligand concentration affected the growth using $Ga(acac)_3$, when compared to using $GaCl_3$ (A2.5). Excess OLAm produced larger nanoparticles that included aggregated clusters of smaller nanoparticles with poor colloidal stability; this was seen with both Ga precursor samples. In contrast to the PtSn case, excess oleic acid (OAc) unexpectedly produced smaller, irregularly shaped nanoparticles. X-Ray diffraction patterns for the samples in A2.4 matched bulk Pt with excess OAc but Pt_3Ga with excess OLAm, while A2.5 appeared to be bulk Pt.

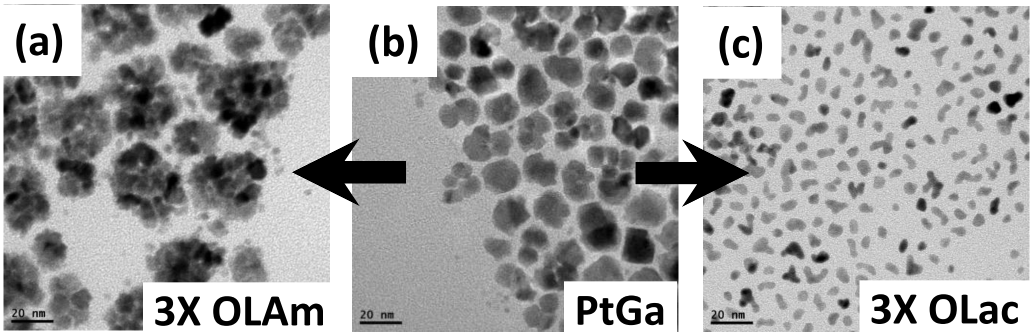

A2.4 TEM of 1:1 Pt:Ga nanoparticles synthesized using (a) 1:3 OLAc:OLAm (b) 1:1 OLAc:OLAm and (c) 3:1 OLAc:OLAm using GaAc

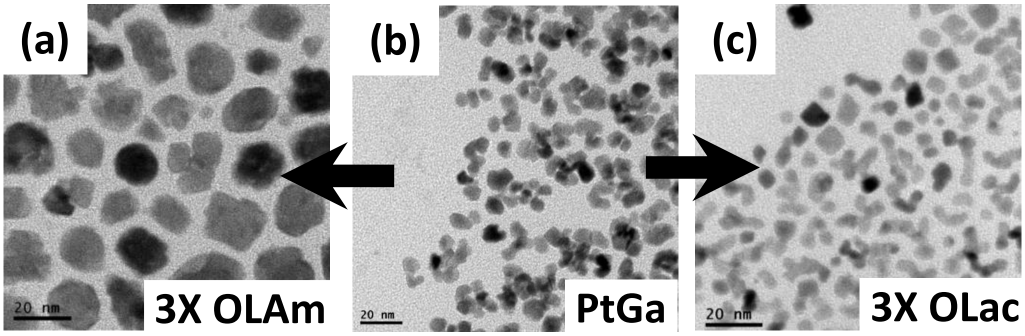

A2.5 TEM of 1:1 Pt:Ga nanoparticles synthesized using (a) 1:3 OLAc:OLAm (b) 1:1 OLAc:OLAm and (c) 3:1 OLAc:OLAm using $GaCl_3$

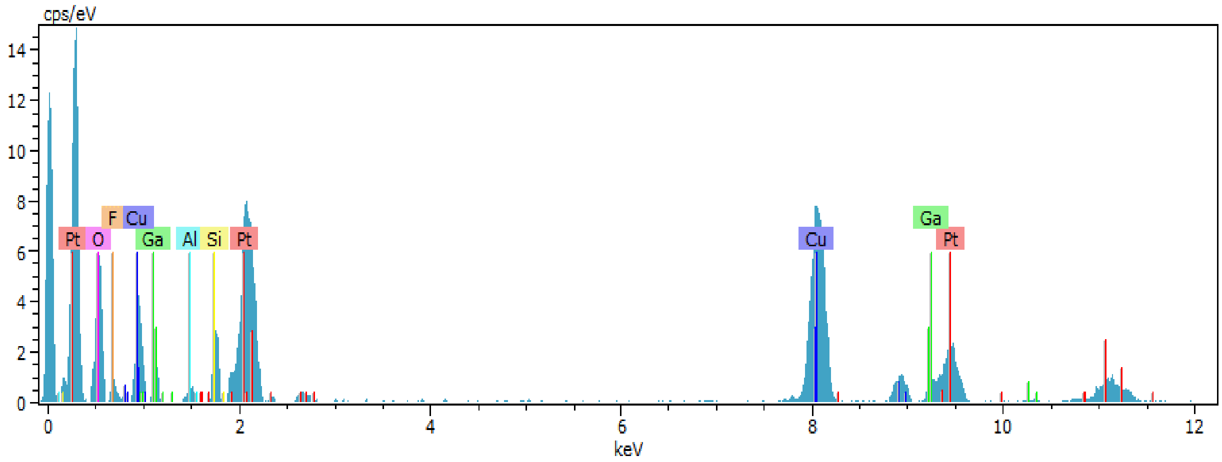

A2.6. Raw EDS data of Pt-Ga alloy nanocrystal

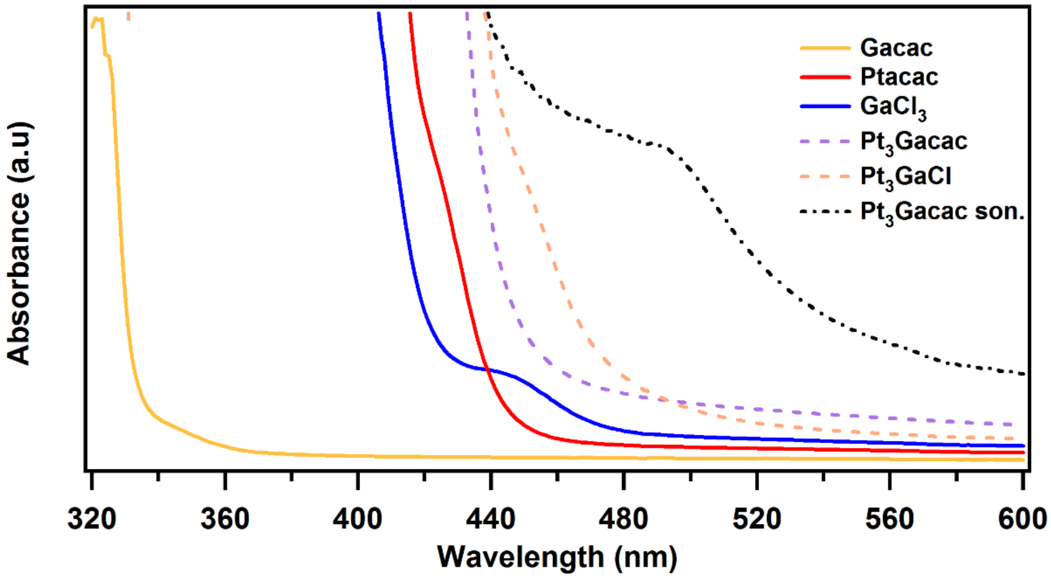

A2.7 Absorption spectra of Pt-Ga complexation using PtAc with GaAc and $GaCl_3$. If ‘wet’ benzyl ether is ever used and the solution prepared in air, the feature at 496 nm in 3:1 Pt:Ga is absent. If the precursor solution is exposed to air after complexation, the feature gradually disappears. For a 1:1 Pt:Ga complex solution, a similar absorption spectrum results. Extended sonication of the precursor solution is typically associated with the appearance of the peak at 496 nm. $GaCl_3$ has a peak at 446 nm.

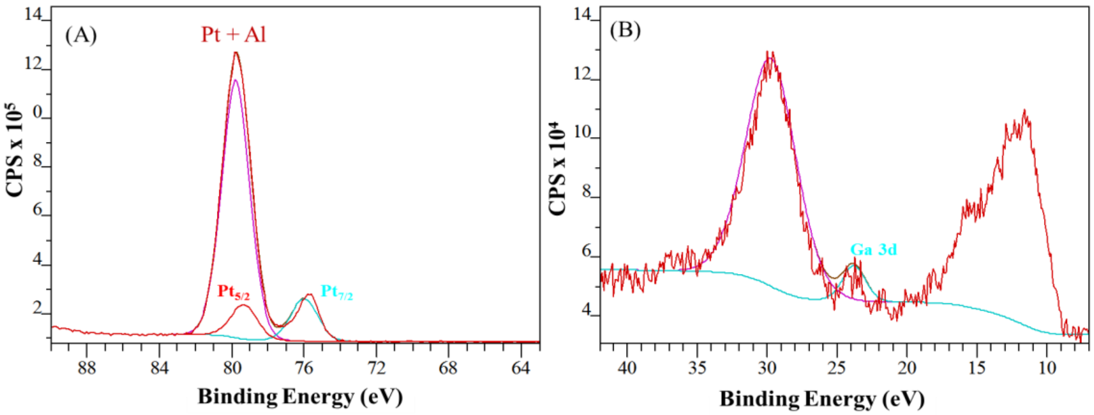

A2.8. Deconvolution of (A) Pt4f and (B) Ga 3d region

Energy (eV)	IMFP (Å)	Energy (eV)	IMFP (Å)
300	6.00	580.6	8.98
311.2	6.12	591.8	9.10
322.4	6.24	603.1	9.21
333.7	6.36	614.3	9.33
344.9	6.49	625.5	9.44
356.1	6.61	636.7	9.56
367.3	6.73	648	9.67
378.6	6.85	659.2	9.78
389.8	6.97	670.4	9.90
401	7.09	681.6	10.01
412.2	7.21	692.9	10.12
423.5	7.33	704.1	10.24
434.7	7.45	715.3	10.35
445.9	7.57	726.5	10.46
457.1	7.69	737.8	10.57
468.4	7.81	749	10.68
479.6	7.93	760.2	10.79
490.8	8.05	771.4	10.90
502	8.17	782.7	11.02
513.3	8.28	793.9	11.13
524.5	8.40	805.1	11.24
535.7	8.52	816.3	11.35
546.9	8.64	827.6	11.46
558.2	8.75	838.8	11.57
569.4	8.87	850	11.67

Table A2.1 Simulated IMFP of electrons in Pt_3Ga from NIST IMFP Calculator (E_g was 0)

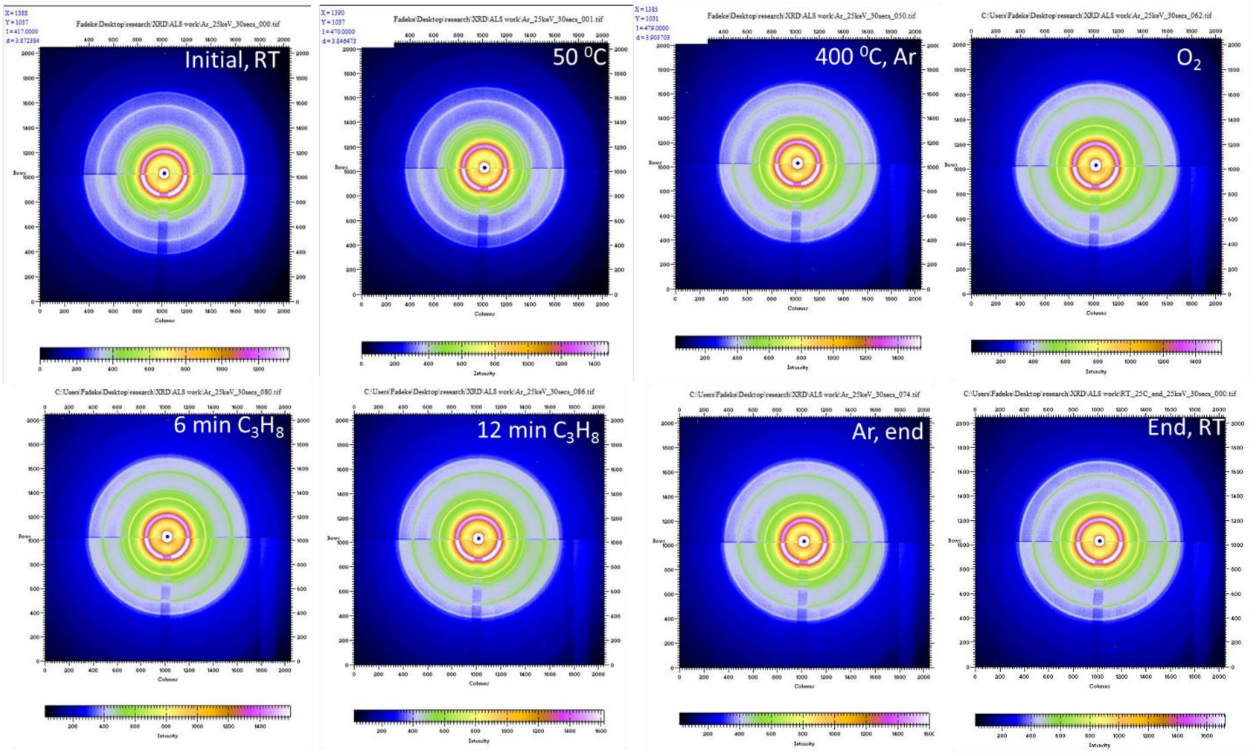

A2.9. Selected, raw 30 second XRD data scans taken every minute under gas flow

RT, initial, Å	4.434	3.824	2.655	2.239		1.811	1.629	1.564
RT, end, Å	4.473	3.837	2.655	2.240	2.135	1.811	1.642	1.590
Pt			(111) 2.65					
Pt_2Ga	(201) 4.564	(301) 3.877		(012) 2.246	(502) 2.107			
Pt_3Ga		(100) 3.83		(111) 2.22				(211) 1.58
Pt_5Ga_3					(311) 2.123			
ε Ga_2O_3				(102) 2.209			(422) 1.681	
α Ga_2O_3	(002) 4.628		(104) 2.651		(113) 2.177	(024) 1.814	(116) 1.665	
γ Ga_2O_3								(511) 1.585

Table A2.2 Diffraction peaks pre and post catalysis at BL 12.2.2

References

[1] D. V. Talapin, J.-S. Lee, M. V. Kovalenko, and E. V. Shevchenko, “Prospects of colloidal nanocrystals for electronic and optoelectronic applications.,” *Chem. Rev.*, vol. 110, no. 1, pp. 389–458, 2010.

[2] (a) A. P. Alivisatos, “Perspectives on the Physical Chemistry of Semiconductor Nanocrystals.” *J. Chem. Phys.*, vol. 100, pp. 13226-13239, 1996. (b) J. Z. Zhang, Z. Wang, J. Liu, S. Chen and G. Liu. *Self-Assembled Nanostructures*- Optical, Electronic, and Dynamic Properties of Semiconductor Nanomaterials . US:Springer, 2003.

[3] L. E. Brus, “Electron–electron and electron-hole interactions in small semiconductor crystallites: The size dependence of the lowest excited electronic state,” *J. Chem. Phys.*, vol. 80, pp. 4403–4409, 1984.

[4] A. J. Nozik, “Physical Chemistry of Semiconductor-Liquid Interfaces,” *J. Chem. Phys.*, vol. 100, pp. 13061-13078, 1996.

[5] X. Chen, S. Shen, L. Guo, and S. S. Mao, “Semiconductor-based Photocatalytic Hydrogen Generation,” *Chem. Rev.*, vol. 110, pp. 6503–6570, 2010.

[6] L. Carbone, P. D. Cozzoli, “Colloidal heterostructured nanocrystals: Synthesis and growth mechanisms," *Nano Today*, vol 5, pp. 449-493, 2010

[7] P. D. Cozzoli, T. Pellegrino, and L. Manna, “Synthesis, properties and perspectives of hybrid nanocrystal structures,” *Chem. Soc. Rev.*, vol. 35, p. 1195, 2006.

[8] M. V. Kovalenko, L. Manna, A. Cabot, Z. Hens, D. V. Talapin, C. R. Kagan, V. I. Klimov, A. L. Rogach, P. Reiss, D. J. Milliron, P. Guyot-Sionnnest, G. Konstantatos, W. J. Parak, T. Hyeon, B. A. Korgel, C. B. Murray, and W. Heiss, “Prospects of nanoscience with nanocrystals.,” *ACS nano*, vol. 9, no. 2, pp. 1012–1057, 2015.

[9] N. T. K. Thanh, N. Maclean, and S. Mahiddine, “Mechanisms of Nucleation and Growth of Nanoparticles in Solution,” *Chem. Rev.* vol 114, pp. 7610-7630, 2014

[10] V. K. L. Mer, “Nucleation in Phase Transitions.,” *Ind. & Eng. Chem.*, vol. 44, pp. 1270–1277, 1952.

[11] M. Casavola, R. Buonsanti, G. Caputo, and P. D. Cozzoli, “Colloidal Strategies for Preparing Oxide-Based Hybrid Nanocrystals,” *Eur. J. Inorg. Chem.*, vol. 2008, pp. 837–854, Feb. 2008.

[12] Y. Xiong and X. Lu, Eds., *Metallic Nanostructures*- From Controlled Synthesis to Applications. Switzerland:Springer Science, 2015. Print.

[13] W. W. Yu, Y. A. Wang, and X. Peng, “Formation and Stability of Size-, Shape-, and Structure-Controlled CdTe Nanocrystals: Ligand Effects on Monomers and Nanocrystals,” *Chem. Mater.*, vol. 15, pp. 4300–4308, 2003.

[14] V. F. Puntes, “Colloidal Nanocrystal Shape and Size Control: The Case of Cobalt,” *Science*, vol. 291, pp. 2115–2117, 2001.

[15] L. Li, J. Hu, W. Yang, and A. P. Alivisatos, “Band Gap Variation of Size- and Shape-Controlled Colloidal CdSe Quantum Rods,” *Nano Lett.*, vol. 1, pp. 349–351, 2001.

[16] Z. A. Peng and X. Peng, “Nearly Monodisperse and Shape-Controlled CdSe Nanocrystals via Alternative Routes: Nucleation and Growth,” *J. Am. Chem. Soc.*, vol. 124, pp. 3343–3353, 2002.

[17] L. Liu, Z. Zhuang, T. Xie, Y. Wang. J. Li, Q. Peng and Y. Li. “Shape Control of CdSe Nanocrystals with Zinc Blende Structure," *J. Am. Chem. Soc.*, vol. 131, pp. 16423-16429, 2009.

[18] W. Shi, H. Zeng, Y. Sahoo, T. Y. Ohulchanskyy, Y. Ding, Z. L. Wang, M. Swihart, and P.

N. Prasad, "A General Approach to Binary and Ternary Hybrid Nanocrystals," *Nano Lett.*, vol. 6, pp. 875–881, 2006.

[19] S. E. Habas, P. Yang, and T. Mokari, "Selective Growth of Metal and Binary Metal Tips on CdS Nanorods," *J. Am. Chem. Soc.*, vol. 130, pp. 3294–3295, 2008.

[20] T. Mokari, E. Rothenberg, I. Popov, R. Costi, and U. Banin, "Selective growth of metal tips onto semiconductor quantum rods and tetrapods," *Science*, vol. 304, pp. 1787–1790, 2004.

[21] M. R. Buck, J. F. Bondi, and R. E. Schaak, "A total-synthesis framework for the construction of high-order colloidal hybrid nanoparticles.," *Nat. Chem.*, vol. 4, no. 1, pp. 37–44, 2012.

[22] R. Jiang, B. Li, C. Fang, and J. Wang, "Metal/Semiconductor Hybrid Nanostructures for Plasmon-Enhanced Applications," *Adv. Mater.*, vol. 26, pp. 5274–5309, 2014.

[23] S. He, H. Zhang, S. Delikanli, Y. Qin, M. T. Swihart, and H. Zeng, "Bifunctional Magneto-Optical FePt−CdS Hybrid Nanoparticles," *J. Phys. Chem. C*, vol. 113, pp. 87–90, 2009.

[24] H. Yu, M. Chen, P. M. Rice, S. X. Wang, R. L. White, and S. Sun, "Dumbbell-like Bifunctional Au−Fe_3O_4Nanoparticles," *Nano Lett.*, vol. 5, pp. 379–382, 2005.

[25] H. Gu, R. Zheng, X. Zhang, and B. Xu, "Facile One-Pot Synthesis of Bifunctional Heterodimers of Nanoparticles: A Conjugate of Quantum Dot and Magnetic Nanoparticles," *J. Am. Chem. Soc.*, vol. 126, pp. 5664–5665, 2004.

[26] U. Banin, Y. Ben-Shahar, and K. Vinokurov, "Hybrid Semiconductor–Metal nanocrystals: From Architecture to Function," *Chem. Mater.*, vol. 26, pp. 97–110, 2013.

[27] X. Li, J. Lian, M. Lin, and Y. Chan, "Light-induced selective deposition of metals on gold-tipped CdSe-seeded CdS nanorods," *J. Am. Chem. Soc.*, vol. 133, pp. 672–675, 2010.

[28] G. Menagen, J. E. Macdonald, Y. Shemesh, I. Popov and U. Banin. "Au growth on Semiconductor Nanorods: Photoinduced versus Thermal Growth Mechanisms," *J. Am. Chem. Soc.*, vol. 131, pp. 17406-17411, 2009.

[29] C.-M. Huang, S.-H. Cheng, U.-S. Jeng, C.-S. Yang, and L.-W. Lo, "Formation of CdSe/CdS/ZnS-Au/SiO2 dual-yolk/shell nanostructures through a Trojan-type inside-out etching strategy," *Nano Res.*, vol. 5, pp. 654–666, 2012.

[30] H. Schlicke, D. Ghosh, L.-K. Fong, H. L. Xin, H. Zheng, and A. P. Alivisatos, "Selective placement of faceted metal tips on semiconductor nanorods.," *Angew. Chem.*, vol. 52, no. 3, pp. 980–982, 2013.

[31] S. Deka, A. Falqui, G. Bertoni, C. Sangregorio, G. Poneti, G. Morello, M. D. Giorgi, C. Giannini, R. Cingolani, L. Manna, and P. D. Cozzoli, "Fluorescent Asymmetrically Cobalt-Tipped CdSe@CdS Core@Shell Nanorod Heterostructures Exhibiting Room-Temperature Ferromagnetic Behavior," *J. Am. Chem. Soc.*, vol. 131, pp. 12817–12828, 2009.

[32] L. J. Hill, M. M. Bull, Y. Sung, A. G. Simmonds, P. T. Dirlam, N. E. Richey, S. E. DeRosa, I.-B. Shim, D. Guin, P. J. Costanzo, N. Pinna, M.-G. Willinger, W. Vogel, K. Char, and J. Pyun, "Directing the deposition of ferromagnetic cobalt onto Pt-tipped CdSe@CdS nanorods: synthetic and mechanistic insights.," *ACS nano*, vol. 6, no. 10, pp. 8632–8645, 2012.

[33] K. Vinokurov, J. E. Macdonald, and U. Banin, "Structures and Mechanisms in the Growth of Hybrid Ru–Cu2S Nanoparticles: From Cages to Nanonets," *Chem. Mater.*, vol. 24, pp. 1822–1827, 2012.

[34] S. Liang, X.-L. Liu, Y.-Z. Yang, Y.-L. Wang, J.-H. Wang, Z.-J. Yang, L.-B. Wang, S.-F. Jia, X.-F. Yu, and L. Zhou, "Symmetric and Asymmetric Au–AgCdSe Hybrid Nanorods," *Nano Lett.*, vol. 12, pp. 5281–5286, 2012.

[35] A. Fujishima and K. Honda, "Electrochemical photolysis of water at a semiconductor

electrode.," *Nature*, pp. 37–8, 1972.

[36] P. V. Kamat, "Manipulation of charge transfer across semiconductor interface. A criterion that cannot be ignored in photocatalyst design," *J. Phys. Chem. Lett.*, vol. 3, pp. 663–672, 2012.

[37] F. E. Osterloh, "Inorganic Materials as Catalysts for Photochemical Splitting of Water," *Chem. Mater.*, vol. 20, pp. 35–54, 2008.

[38] H. Kato, K. Asakura, and A. Kudo, "Highly efficient water splitting into H_2 and O_2 over lanthanum-doped $NaTaO_3$ photocatalysts with high crystallinity and surface nanostructure," *J. Am. Chem. Soc.*, vol. 125, pp. 3082–3089, 2003.

[39] J. Luo, J.-H. Im, M. T. Mayer, M. Schreier, M. K. Nazeeruddin, N.-G. Park, S. D. Tilley, H. J. Fan, and M. Grätzel, "Water photolysis at 12.3% efficiency via perovskite photovoltaics and Earth-abundant catalysts," *Science*, vol. 345, pp. 1593–1596, 2014.

[40] O. Khaselev and J. A. Turner, "A monolithic photovoltaic-photoelectrochemical device for hydrogen production via water splitting," *Science*, vol. 280, pp. 425–427, 1998.

[41] T. W. Kim and K.-S. Choi, "Nanoporous BiVO4 photoanodes with dual-layer oxygen evolution catalysts for solar water splitting," *Science*, vol. 343, pp. 990–994, 2014.

[42] Z. Zhang and J. T. Yates, "Band Bending in Semiconductors: Chemical and Physical Consequences at Surfaces and Interfaces," *Chem. Rev.*, vol. 112, pp. 5520–5551, 2012.

[43] S. S. Lo, T. Mirkovic, C.-H. Chuang, C. Burda, and G. D. Scholes, "Emergent Properties Resulting from Type-II Band Alignment in Semiconductor Nanoheterostructures," *Adv. Mater.*, vol. 23, pp. 180–197, 2011.

[44] A. M. Smith and S. Nie, "Semiconductor Nanocrystals: Structure, Properties, and Band Gap Engineering," *Accounts Chem. Res.*, vol. 43, pp. 190–200, 2010.

[45] A. Sitt, F. D. Sala, G. Menagen, and U. Banin, "Multiexciton Engineering in Seeded Core/Shell Nanorods: Transfer from Type-I to Quasi-type-II Regimes," *Nano Lett.*, vol. 9, no. 10, pp. 3470–3476, Aug. 2009.

[46] N. Al-Salim, A. G. Young, R. D. Tilley, A. J. McQuillan, and J. Xia, "Synthesis of CdSeS Nanocrystals in Coordinating and Noncoordinating Solvents: Solvent's Role in Evolution of the Optical and Structural Properties," *Chem. Mater.*, vol. 19, pp. 5185–5193, 2007.

[47] W. W. Yu, L. Qu, W. Guo, and X. Peng, "Experimental Determination of the Extinction Coefficient of CdTe, CdSe, and CdS Nanocrystals," *Chem. Mater.*, vol. 15, pp. 2854–2860, 2003.

[48] D. V. Talapin, J. H. Nelson, E. V. Shevchenko, S. Aloni, B. Sadtler, and A. P. Alivisatos, "Seeded Growth of Highly Luminescent CdSe/CdS Nanoheterostructures with Rod and Tetrapod Morphologies," *Nano Lett.*, vol. 7, pp. 2951–2959, 2007.

[49] X. Peng, M. C. Schlamp, A. V. Kadavanich and A. P. Alivisatos. "Epitaxial Growth of Highly Luminescent CdSe/CdS Core/Shell Nanocrystals with Photostability and Electronic Accessibility," *J. Am. Chem. Soc.* vol 119, pp. 7019-7029, 1997.

[50] D.V. Talapin, R. Koeppe, S. Gotzinger, A. Kornowski, J. M. Lupton, A. L. ROach, O. Benson, J. Feldmann and H. Weller. "Highly Emissive Colloidal CdSe/CdS Heterostructures of Mixed Dimensionality," vol 3, pp. 1677-1681.

[51] L. Carbone, C. Nobile, M. D. Giorgi, F. D. Sala, G. Morello, P. Pompa, M. Hytch, E. Snoeck, A. Fiore, I. R. Franchini, M. Nadasan, A. F. Silvestre, L. Chiodo, S. Kudera, R. Cingolani, R. Krahne, and L. Manna, "Synthesis and Micrometer-Scale Assembly of Colloidal CdSe/CdS Nanorods Prepared by a Seeded Growth Approach," *Nano Lett.*, vol. 7, pp. 2942–2950, 2007.

[52] H. N. Kim, T. W. Kim, I. Y. Kim, and S.-J. Hwang, "Cocatalyst-Free Photocatalysts for Efficient Visible-Light-Induced H2 Production: Porous Assemblies of CdS Quantum Dots and Layered Titanate Nanosheets," *Adv. Funct. Mater.*, vol. 21, pp. 3111–3118, 2011.

[53] X. Zong, H. Yan, G. Wu, G. Ma, F. Wen, L. Wang, and C. Li, “Enhancement of Photocatalytic H_2Evolution on CdS by Loading MoS_2 as Cocatalyst under Visible Light Irradiation,” *J. Am. Chem. Soc.*, vol. 130, pp. 7176–7177, 2008.

[54] L. Amirav and A. P. Alivisatos, “Photocatalytic Hydrogen Production with Tunable Nanorod Heterostructures,” *J. Phys. Chem. Lett.*, vol. 1, pp. 1051–1054, 2010.

[55] M. L. Tang, D. C. Grauer, B. Lassalle-Kaiser, V. K. Yachandra, L. Amirav, J. R. Long, J. Yano, and A. P. Alivisatos, “Structural and Electronic Study of an Amorphous MoS_3 Hydrogen-Generation Catalyst on a Quantum-Controlled Photosensitizer,” *Angew. Chem.*, vol. 123, pp. 10385–10389, 2011.

[56] M. A. Holmes, T. K. Townsend, and F. E. Osterloh, “Quantum confinement controlled photocatalytic water splitting by suspended CdSe nanocrystals,” *Chem. Commun.*, vol. 48, p. 371, 2011.

[57] N. Buhler, K. Meler and J. Reber. “Photochemicl Hydrogen Production with Cadmium Sulfide Suspensions," vol 88, pp.3261-3268

[58] K. Wu, Z. Chen, H. Lv, H. Zhu, C. L. Hill, and T. Lian, “Hole Removal Rate Limits Photodriven H_2Generation Efficiency in CdS-Pt and CdSe/CdS-Pt Semiconductor Nanorod–Metal Tip Heterostructures,” *J. Am. Chem. Soc.*, vol. 136, pp. 7708–7716, 2014.

[59] J. Aldana, Y. A. Wang, and X. Peng, “Photochemical Instability of CdSe Nanocrystals Coated by Hydrophilic Thiols,” *J. Am. Chem. Soc.*, vol. 123, pp. 8844–8850, 2001.

[60] K. P. Acharya, R. S. Khnayzer, T. O’Connor, G. Diederich, M. Kirsanova, A. Klinkova, D. Roth, E. Kinder, M. Imboden, and M. Zamkov, “The Role of Hole Localization in Sacrificial Hydrogen Production by Semiconductor–Metal Heterostructured Nanocrystals,” *Nano Lett.*, vol. 11, pp. 2919–2926, 2011.

[61] M. J. Berr, P. Wagner, S. Fischbach, A. Vaneski, J. Schneider, A. S. Susha, A. L. Rogach, F. Jäckel, and J. Feldmann, “Hole scavenger redox potentials determine quantum efficiency and stability of Pt-decorated CdS nanorods for photocatalytic hydrogen generation,” *Appl. Phys. Lett.*, vol. 100, 2012.

[62] S. Chen and L.-W. Wang, “Thermodynamic Oxidation and Reduction Potentials of Photocatalytic Semiconductors in Aqueous Solution,” *Chem. Mater.* vol 24, pp. 3659-3666, 2012.

[63] K. Tarafder, Y. Surendranath, J. H. Olshansky, A. P. Alivisatos, and L.-W. Wang, “Hole transfer dynamics from a CdSe/CdS quantum rod to a tethered ferrocene derivative,” *J. Am. Chem. Soc.*, vol. 136, pp. 5121–5131, 2014.

[64] T. X. Ding, J. H. Olshansky, S. R. Leone, and A. P. Alivisatos, “On the Efficiency of Hole Transfer from Photoexcited Quantum Dots to Covalently Linked Molecular Species,” *J. Am. Chem. Soc.*, 2015.

[65] S. A. Ivanov and M. Achermann, “Spectral and Dynamic Properties of Excitons and Biexcitons in Type-II Semiconductor Nanocrystals,” *ACS Nano*, vol. 4, pp. 5994–6000, 2010.

[66] J. Müller, J. M. Lupton, P. G. Lagoudakis, F. Schindler, R. Koeppe, A. L. Rogach, J. Feldmann, D. V. Talapin, and H. Weller, “Wave Function Engineering in Elongated Semiconductor Nanocrystals with Heterogeneous Carrier Confinement,” *Nano Lett.*, vol. 5, no. 10, pp. 2044–2049, Aug. 2005.

[67] K. A. Brown, M. B. Wilker, M. Boehm, G. Dukovic, and P. W. King, “Characterization of photochemical processes for H2 production by CdS nanorod–[FeFe] hydrogenase complexes,” *J. Am. Chem. Soc.*, vol. 134, pp. 5627–5636, 2012.

[68] G. Dukovic, M. G. Merkle, J. H. Nelson, S. M. Hughes, and A. P. Alivisatos, “Photodeposition of Pt on Colloidal CdS and CdSe/CdS Semiconductor Nanostructures,” *Adv.*

Mater., vol. 20, pp. 4306–4311, 2008.

[69] M. J. Berr, A. Vaneski, C. Mauser, S. Fischbach, A. S. Susha, A. L. Rogach, F. Jäckel, and J. Feldmann, “Delayed Photoelectron Transfer in Pt-Decorated CdS Nanorods under Hydrogen Generation Conditions,” *Small*, vol. 8, pp. 291–297, 2012.

[70] M. V. Brink, M. A. Peck, K. L. More, and J. D. Hoefelmeyer, “Alkylamine Stabilized Ruthenium Nanocrystals: Faceting and Branching,” *J. Phys. Chem. C*, vol. 112, pp. 12122–12126, 2008.

[71] D. Rochefort, P. Dabo, D. Guay, and P. M. A. Sherwood, “XPS investigations of thermally prepared RuO_2 electrodes in reductive conditions,” *Electrochimica Acta*, vol. 48, pp. 4245–4252, 2003.

[72] A. Foelske, O. Barbieri, M. Hahn, and R. Kötz, “An X-Ray Photoelectron Spectroscopy Study of Hydrous Ruthenium Oxide Powders with Various Water Contents for Supercapacitors,” *Electrochem. Solid-state Lett.*, vol. 9, p. 268, 2006.

[73] H. Over, A. P. Seitsonen, E. Lundgren, M. Smedh, and J. N. Andersen, “On the origin of the Ru-$3d_{5/2}$ satellite feature from RuO_2 (110),” *Surf. Sci.*, vol. 504, 2002.

[74] W. Vogel, V. L. Rhun, E. Garnier, and N. Alonso-Vante, “Ru Clusters Synthesized Chemically from Dissolved Carbonyl: In Situ Study of a Novel Electrocatalyst in the Gas Phase and in Electrochemical Environment,” *J. Phys. Chem. B*, vol. 105, pp. 5238–5243, 2001.

[75] X. Peng, J. Wickham and A. P. Alivisatos. “Kinetics of II-VI and III-V Colloidal Semiconductor Nanocrystal Growth: “Focusing” of Size Distributions,” *J. Am. Chem. Soc.*, vol 120, pp 5343–5344, 1998

[76] J. Owen, E, M. Chan, H, Liu and A. P. Alivisatos. “Precursor Conversion Kinetics and the Nucleation of Cadmium Selenide Nanocrystals," *J. Am. Chem. Soc*, vol 132, pp. 18206-18213, 2010.

[77] H. Liu, J. Owen and A. P. Alivisatos. “Mechanistic Study of Precursor Evolution in Colloidal Group II-VI Semiconductor Nanocrystal Synthesis,” *J. Am. Chem. Soc.* vol 129, pp. 305-312, 2007

[78] B. Mahler, N. Lequeux, and B. Dubertret, “Ligand-Controlled Polytypism of Thick-Shell CdSe/CdS Nanocrystals,” *J. Am. Chem. Soc.*, vol. 132, pp. 953–959, Jan. 2010.

[79] J. Huang, M. V. Kovalenko, and D. V. Talapin, “Alkyl Chains of Surface Ligands Affect Polytypism of CdSe Nanocrystals and Play an Important Role in the Synthesis of Anisotropic Nanoheterostructures,” *J. Am. Chem. Soc.*, vol. 132, pp. 15866–15868, 2010.

[80] A. Puzder, A. J. Williamson, N. Zaitseva, G. Galli, L. Manna, and A. P. Alivisatos, “The Effect of Organic Ligand Binding on the Growth of CdSe Nanoparticles Probed by Ab Initio Calculations,” *Nano Lett.*, vol. 4, pp. 2361–2365, 2004.

[81] J. T. Siy and M. H. Bartl, “Insights into Reversible Dissolution of Colloidal CdSe Nanocrystal Quantum Dots,” *Chem. Mater.*, vol. 22, pp. 5973–5982, 2010.

[82] R. Costi, A. E. Saunders, E. Elmalem, A. Salant, and U. Banin, “Visible Light-Induced Charge Retention and Photocatalysis with Hybrid CdSe-Au Nanodumbbells,” *Nano Lett.*, vol. 8, pp. 637–641, Feb. 2008.

[83] R. A. L. Berghe, W. P. Gomes, and F. Cardon, “Electrochemical Reactions at the Illuminated CdSe Anode,” *Z. für Phys. Chem.*, vol. 92, pp. 91–100, 1974.

[84] J. E. Yourey, J. B. Kurtz, and B. M. Bartlett, “Water oxidation on a CuWO4–WO3 composite electrode in the presence of [Fe (CN) 6] 3–: Toward solar Z-scheme water splitting at zero bias,” *J. Phys. Chem. C*, vol. 116, pp. 3200–3205, 2012.

[85] W. Wang, J. Chen, C. Li, and W. Tian, “Achieving solar overall water splitting with hybrid

photosystems of photosystem II and artificial photocatalysts," *Nat Comms*, vol. 5, Aug. 2014.

[86] K.-W. Kwon and M. Shim, "γ-Fe_2O_3/II−VI Sulfide Nanocrystal Heterojunctions," *J. Am. Chem. Soc.*, vol. 127, pp. 10269–10275, 2005.

[87] A. W. Lin, C. Y. Ang, P. K. Patra, Y. Han, H. Gu, J.-M. Le Breton, J. Juraszek, H. Chiron, G. C. Papaefthymiou, and S. T. Selvan, "Seed-mediated synthesis, properties and application of γ-Fe_2O_3–CdSe magnetic quantum dots," *J. Solid State Chem.*, vol. 184, pp. 2150–2158, 2011.

[88] A. Agiral, H. S. Soo and H. Frei. " Visible Light Induced Hole Transport from Sensitizer to Co_3O_4 Water Oxidation Catalyst across Nanoscale Silica Barrier with Embedded Molecular Wires," *Chem. Mater*., vol 25, pp 2264–2273, 2013

[89] Y. Guo, S. R. Alvarado, J. D. Barclay, and J. Vela, "Shape-Programmed Nanofabrication: Understanding the Reactivity of Dichalcogenide Precursors," *ACS nano*, vol. 7, pp. 3616–3626, 2013.

[90] S. R. Alvarado, Y. Guo, T. P. A. Ruberu, E. Tavasoli, and J. Vela, "Inorganic chemistry solutions to semiconductor nanocrystal problems," *Coord. Chem. Rev.*, vol. 263, pp. 182–196, 2014.

[91] D. J. Barber and I. C. Freestone "An Investigation of the Origin of the Color of the Lycurgus Cup by Analytical Transmission Electron Microscopy," *Archaeometry*, vol. 32, pp. 33–45, Feb. 1990.

[92] G. Padeletti and P. Fermo, "How the masters in Umbria, Italy, generated and used nanoparticles in art fabrication during the Renaissance period," *Appl. Phys. A: Mater. Sci. & Process.*, vol. 76, pp. 515–525, Mar. 2003.

[93] M. Faraday, "The Bakerian lecture: experimental relations of gold (and other metals) to light," *Philos. Trans. R. Soc. Lond.*, vol. 147, pp. 145–181, 1857.

[94] G. Mie, "Contributions to the optics of turbid media, particularly of colloidal metal solutions," *Contrib. to Opt. Turbid. media, Part. colloidal Met. solutions Transl. into Engl. from Ann. Phys.*, vol. 1, pp. 377–445, 1976.

[95] D. Wang and Y. Li, "Bimetallic Nanocrystals: Liquid-Phase Synthesis and Catalytic Applications," *Adv. Mater.*, vol. 23, pp. 1044–1060, Jan. 2011.

[96] M. Sankar, N. Dimitratos, P. J. Miedziak, P. P. Wells, C. J. Kiely, and G. J. Hutchings, "Designing bimetallic catalysts for a green and sustainable future," *Chem. Soc. Rev.*, vol. 41, 2012.

[97] C. J. Murphy, T. K. Sau, A. M. Gole, C. J. Orendorff, J. Gao, L. Gou, S. E. Hunyadi, and T. Li, "Anisotropic metal nanocrystals: synthesis, assembly, and optical applications," *J. Phys. Chem. B*, vol. 109, pp. 13857–13870, 2005.

[98] P. K. Jain, X. Huang, I. H. El-Sayed, and M. A. El-Sayed, "Noble metals on the nanoscale: optical and photothermal properties and some applications in imaging, sensing, biology, and medicine," *Accounts Chem. Res.*, vol. 41, pp. 1578–1586, 2008.

[99] P. Alivisatos, "The use of nanocrystals in biological detection," *Nat. Biotechnol.*, vol. 22, pp. 47–52, 2004.

[100] R. Ferrando, J. Jellinek, and R. L. Johnston, "Nanoalloys: From Theory to Applications of Alloy Clusters and Nanoparticles," *Chem. Rev.*, vol. 108, pp. 845–910, 2008.

[101] W. P. Halperin, "Quantum size effects in metal particles," *Rev. Mod. Phys.*, vol. 58, pp. 533–606, 1986.

[102] A. Nilsson, L. G. M. Pettersson, B. Hammer, T. Bligaard, C. H. Christensen, and J. K. Norskov, "The electronic structure effect in heterogeneous catalysis," *Catal. Lett.*, vol. 100, pp. 111–114, 2005.

[103] B. Hammer and J. K. Nørskov, "Theoretical surface science and catalysis—calculations

and concepts," *Adv. Catal.*, vol. 45, pp. 71–129, 2000.

[104] J. K. Nørskov, F. Abild-Pedersen, F. Studt, and T. Bligaard, "Density functional theory in surface chemistry and catalysis," *Proc. Natl. Acad. Sci.*, vol. 108, pp. 937–943, 2011.

[105] J. Greeley, J. K. Nørskov, and M. Mavrikakis, "Electronic structure and catalysis on metal surfaces," *Annu. Rev. Phys. Chem.*, vol. 53, pp. 319–348, 2002.

[106] M.-L. Yang, Y.-A. Zhu, X.-G. Zhou, Z.-J. Sui, and D. Chen, "First-Principles Calculations of Propane Dehydrogenation over PtSn Catalysts," *ACS Catal.*, vol. 2, pp. 1247–1258, 2012.

[107] L. Nykänen and K. Honkala, "Density Functional Theory Study on Propane and Propene Adsorption on Pt(111) and PtSn Alloy Surfaces," *J. Phys. Chem. C*, vol. 115, no. 19, pp. 9578–9586, 2011.

[108] A. Cybulski, J. A. Moulijin and A. Stankiewicz. "Novel Concepts in Catalysis and Chemical Reactors: Improving the Efficiency for the Future." Wiley, 2010.

[109] K. An and G. A. Somorjai, "Size and Shape Control of Metal nanocrystals for Reaction Selectivity in Catalysis," *ChemCatChem*, vol. 4, pp. 1512–1524, 2012.

[110] J. Shi, "On the synergetic catalytic effect in heterogeneous nanocomposite catalysts," *Chem. Rev.*, vol. 113, pp. 2139–2181, 2012.

[111] X. Liu, D. Wang, and Y. Li, "Synthesis and catalytic properties of bimetallic nanomaterials with various architectures," *Nano Today*, vol. 7, pp. 448–466, 2012.

[112] H. Jing and H. Wang, "Structural Evolution of Ag–Pd Bimetallic nanocrystals through Controlled Galvanic Replacement: Effects of Mild Reducing Agents," *Chem. Mater.*, vol. 27, pp. 2172–2180, 2015.

[113] Z. Cui, H. Chen, M. Zhao, D. Marshall, Y. Yu, H. Abruña, and F. J. DiSalvo, "Synthesis of Structurally Ordered Pt_3Ti and Pt_3V Nanoparticles as Methanol Oxidation Catalysts," *J. Am. Chem. Soc.*, vol. 136, pp. 10206–10209, 2014.

[114] N. Ortiz and S. E. Skrabalak, "Manipulating Local Ligand Environments for the Controlled Nucleation of Metal nanocrystals and their Assembly into Nanodendrites," *Angew. Chem. Int. Ed.*, vol. 51, pp. 11757–11761, 2012.

[115] N. Ortiz, R. G. Weiner, and S. E. Skrabalak, "Ligand-Controlled Co-reduction versus Electroless Co-deposition: Synthesis of Nanodendrites with Spatially Defined Bimetallic Distributions," *ACS Nano*, vol. 8, pp. 12461–12467, 2014.

[116] N. Ortiz and S. E. Skrabalak, "On the Dual Roles of Ligands in the Synthesis of Colloidal Metal Nanostructures," *Langmuir*, vol. 30, pp. 6649–6659, 2014.

[117] M. He, L. Protesescu, R. Caputo, F. Krumeich, and M. V. Kovalenko, "A General Synthesis Strategy for Monodisperse Metallic and Metalloid Nanoparticles (In, Ga, Bi, Sb, Zn, Cu, Sn, and Their Alloys) via in Situ Formed Metal Long-Chain Amides," *Chem. Mater.*, vol. 27, pp. 635–647, 2015.

[118] L. Bednarova, C. E. Lyman, E. Rytter, and A. Holmen, "Effect of Support on the Size and Composition of Highly Dispersed Pt–Sn Particles," *J. Catal.*, vol. 211, pp. 335–346, 2002.

[119] M. S. Kumar, D. Chen, A. Holmen, and J. C. Walmsley, "Dehydrogenation of propane over Pt-SBA-15 and Pt-Sn-SBA-15: Effect of Sn on the dispersion of Pt and catalytic behavior," *Catal. Today*, vol. 142, pp. 17–23, 2009.

[120] B. K. Vu, E. W. Shin, I. Y. Ahn, J.-M. Ha, D. J. Suh, W.-I. Kim, H.-L. Koh, Y. G. Choi, and S.-B. Lee, "The Effect of Tin–Support Interaction on Catalytic Stability over Pt–Sn/xAl–SBA-15 Catalysts for Propane Dehydrogenation," *Catal. Lett.*, vol. 142, pp. 838–844, May 2012.

[121] Y. Kang, J. B. Pyo, X. Ye, T. R. Gordon, and C. B. Murray, "Synthesis, shape control, and methanol electro-oxidation properties of Pt–Zn alloy and Pt_3Zn intermetallic nanocrystals," *ACS*

Nano, vol. 6, pp. 5642–5647, 2012.

[122] L. R. Alden, D. K. Han, F. Matsumoto, H. D. Abruña, and F. J. DiSalvo, "Intermetallic PtPb Nanoparticles Prepared by Sodium Naphthalide Reduction of Metal-Organic Precursors: Electrocatalytic Oxidation of Formic Acid," *Chem. Mater.*, vol. 18, no. 23, pp. 5591–5596, 2006.

[123] X. Wang, L. Altmann, J. Stover, V. Zielasek, M. Ba?umer, K. Al-Shamery, H. Borchert, J. Parisi, and J. Kolny-Olesiak, "Pt/Sn Intermetallic, Core/Shell and Alloy nanocrystals: Colloidal Synthesis and Structural Control," *Chem. Mater.*, vol. 25, pp. 1400–1407, 2012.

[124] X. Wang, J. Stover, V. Zielasek, L. Altmann, K. Thiel, K. Al-Shamery, M. Baumer, H. Borchert, J. Parisi and J. Kolny-Olesiak."Colloidal Synthesis and Structural Control of PtSn Bimetallic Nanoparicles," *Langmuir*, vol 27, pp. 11052-11061, 2011

[125] M. Yarema, R. Caputo, and M. V. Kovalenko, "Precision synthesis of colloidal inorganic nanocrystals using metal and metalloid amides," *Nanoscale*, vol. 5, 2013.

[126] F. Tao, M. E. Grass, Y. Zhang, D. R. Butcher, J. R. Renzas, Z. Liu, J. Y. Chung, B. S. Mun, M. Salmeron, and G. A. Somorjai, "Reaction-driven restructuring of Rh-Pd and Pt-Pd core-shell nanoparticles," *Science*, vol. 322, pp. 932–934, 2008.

[127] A. Cao, R. Lu, and G. Veser, "Stabilizing metal nanocrystals for heterogeneous catalysis," *Phys. Chem. Chem. Phys.*, vol. 12, 2010.

[128] R. Ouyang, J.-X. Liu, and W.-X. Li, "Atomistic Theory of Ostwald Ripening and Disintegration of Supported Metal Particles under Reaction Conditions," *J. Am. Chem. Soc.*, vol. 135, pp. 1760–1771, 2013.

[129] S. H. Joo, J. Y. Park, C.-K. Tsung, Y. Yamada, P. Yang, and G. A. Somorjai, "Thermally stable Pt/mesoporous silica core–shell nanocatalysts for high-temperature reactions," *Nat. Mater.*, vol. 8, pp. 126–131, 2009.

[130] K. An, Q. Zhang, S. Alayoglu, N. Musselwhite, J.-Y. Shin, and G. A. Somorjai, "High-Temperature Catalytic Reforming of n-Hexane over Supported and Core–Shell Pt Nanoparticle Catalysts: Role of Oxide–Metal Interface and Thermal Stability," *Nano Lett.*, vol. 14, pp. 4907–4912, 2014.

[131] K. Nakagawa, Y. Tanimoto, T. Okayama, K.-I. Sotowa, S. Sugiyama, S. Takenaka, and M. Kishida, "Sintering resistance and catalytic activity of platinum nanoparticles covered with a microporous silica layer using methyltriethoxysilane," *Catal. Lett.*, vol. 136, pp. 71–76, 2010.

[132] J. Lu, B. Fu, M. C. Kung, G. Xiao, J. W. Elam, H. H. Kung, and P. C. Stair, "Coking- and Sintering-Resistant Palladium Catalysts Achieved Through Atomic Layer Deposition," *Science*, vol. 335, pp. 1205–1208, 2012.

[133] D. E. Resasco. "Dehydrogenation by Heterogeneous Catalysts." *Encyclopedia of Catalysis.* 2000.

[134] H. Zimmermann. "Propene." Ullmann's Encyclopedia of Industrial Chemistry." 2013

[135] R. L. Puurunen, B. G. Beheydt, and B. M. Weckhuysen, "Monitoring chromia/alumina catalysts in situ during propane dehydrogenation by optical fiber UV–visible diffuse reflectance spectroscopy," *J. Catal.*, vol. 204, pp. 253–257, 2001.

[136] A. Iglesias-Juez, A. M. Beale, K. Maaijen, T. C. Weng, P. Glatzel, and B. M. Weckhuysen, "A combined in situ time-resolved UV–Vis, Raman and high-energy resolution X-ray absorption spectroscopy study on the deactivation behavior of Pt and Pt Sn propane dehydrogenation catalysts under industrial reaction conditions," *J. Catal.*, vol. 276, pp. 268–279, 2010.

[137] O. A. Barias, A. Holmen, E. A. Blekkan. "Propane Dehydrogenation over Suported Pt and Pt-Sn Catalysts: Catalyst Preparation, Characterization, and Activity Measurements," vol 158, pp. 1-12, 1996.

[138] J. J. H. B. Sattler, I. D. Gonzalez-Jimenez, L. Luo, B. A. Stears, A. Malek, D. G. Barton, B. A. Kilos, M. P. Kaminsky, T. W. G. M. Verhoeven, E. J. Koers, M. Baldus, and B. M. Weckhuysen, “Platinum-Promoted Ga/Al_2O_3 as Highly Active, Selective, and Stable Catalyst for the Dehydrogenation of Propane,” *Angew. Chem.*, 2014.

[139] P. Sun, G. Siddiqi, M. Chi, and A. T. Bell, “Synthesis and characterization of a new catalyst Pt/Mg(Ga)(Al)O for alkane dehydrogenation,” *J. Catal.*, vol. 274, 2010.

[140] G. Siddiqi, P. Sun, V. Galvita, and A. T. Bell, “Catalyst performance of novel Pt/Mg(Ga)(Al)O catalysts for alkane dehydrogenation,” *J. Catal.*, vol. 274, pp. 200–206, 2010.

[141] E.L. Jablonski, A. A. Castro, O. A. Scelza and S. R. de Miguel. “Effect of Ga addition to Pt/Al_2O_3 on the activity, selectivity and deactivation in the propane dehydrogenation,” *App Catal A: General*, vol 183, pp. 189-198, 1999

[142] Y. Li, C. M. Lousada, and P. A. Korzhavyic, “The nature of hydrogen in gamma-alumina,” *J. App. Phys.* vol 115, 2014.

[143] G. D. Meitzner, E. Iglesia, J. E. Baumgartner, and E. S. Huang, “The chemical state of gallium in working alkane dehydrocyclodimerization catalysts. In situ gallium K-edge X-ray absorption spectroscopy,” *J. Catal.*, vol. 140, pp. 209–225, 1993.

[144] M. M. Bhasin, J. H. McCain, B. V. Vora, T. Imai, and P. R. Pujado, “Dehydrogenation and oxydehydrogenation of paraffins to olefins,” *Appl. Catal. A: Gen.*, vol. 221, pp. 397–419, 2001.

[145] A. D. Ballarini, P. Zgolicz, I. M. Vilella, S. R. de Miguel, A. A. Castro, and O. A. Scelza, “n-Butane dehydrogenation on Pt, PtSn and PtGe supported on γ-Al 2 O 3 deposited on spheres of α-Al 2 O 3 by washcoating,” *Appl. Catal. A: Gen.*, vol. 381, pp. 83–91, 2010.

[146] M. C. Román-Martínez, J. A. Maciá-Agulló, I. M. J. Vilella, D. Cazorla-Amorós, and H. Yamashita, “State of Pt in dried and reduced PtIn and PtSn catalysts supported on carbon,” *J. Phys. Chem. C*, vol. 111, pp. 4710–4716, 2007.

[147] J. H. Kim, S. M. Choi, S. H. Nam, M. H. Seo, S. H. Choi, and W. B. Kim, “Influence of Sn content on PtSn/C catalysts for electrooxidation of C 1–C 3 alcohols: synthesis, characterization, and electrocatalytic activity,” *Appl. Catal. B: Environ.*, vol. 82, pp. 89–102, 2008.

[148] A.-C. Boucher, N. Alonso-Vante, F. Dassenoy, and W. Vogel, “Structural and electrochemical studies of Pt-Sn nanoparticulate catalysts,” *Langmuir*, vol. 19, pp. 10885–10891, 2003.

[149] R. E. Cable and R. E. Schaak, “Reacting the unreactive: A toolbox of low-temperature solution-mediated reactions for the facile interconversion of nanocrystalline intermetallic compounds,” *J. Am. Chem. Soc.*, vol. 128, pp. 9588–9589, 2006.

[150] F. Somodi, Z. Peng, A. “Bean” Getsoian, and A. T. Bell, “Effects of the synthesis parameters on the size and composition of Pt–Sn nanoparticles prepared by the polyalcohol reduction method,” *J. Phys. Chem. C*, vol. 115, pp. 19084–19090, 2011.

[151] M. Boualleg, D. Baudouin, J.-M. Basset, F. Bayard, J.-P. Candy, J.-C. Jumas, L. Veyre, and C. Thieuleux, “Unexpected, spontaneous and selective formation of colloidal Pt3Sn nanoparticles using organometallic Pt and Sn complexes,” *Chem. Commun.*, vol. 46, pp. 4722–4724, 2010.

[152] M. Yarema, M. Wörle, M. D. Rossell, R. Erni, R. Caputo, L. Protesescu, K. V. Kravchyk, D. N. Dirin, K. Lienau, and F. von Rohr, “Monodisperse Colloidal Gallium Nanoparticles: Synthesis, Low Temperature Crystallization, Surface Plasmon Resonance and Li-Ion Storage,” *J. Am. Chem. Soc.*, vol. 136, pp. 12422–12430, 2014.

[153] S. Choi, C. Filotto, M. Bisanzo, S. Delaney, D. Lagasee, J. L. Whitworth, A. Jusko, C. Li, N. A. Wood, and J. Willingham, “Reduction and anticancer activity of platinum (IV) complexes,”

Inorg. Chem., vol. 37, pp. 2500–2504, 1998.
[154] L. Shi, A. Wang, Y. Huang, X. Chen, J. J. Delgado, and T. Zhang, “Facile Synthesis of Ultrathin AuCu Dimetallic Nanowire Networks,” *Eur. J. Inorg. Chem.*, vol. 2012, pp. 2700–2706, 2012.
[155] Z. Peng, H. You, and H. Yang, “Composition-Dependent Formation of Platinum Silver Nanowires,” *ACS Nano*, vol. 4, pp. 1501–1510, 2010.
[156] A. K. Sra and R. E. Schaak, “Synthesis of atomically ordered AuCu and AuCu3 nanocrystals from bimetallic nanocrystal precursors,” *J. Am. Chem. Soc.*, vol. 126, pp. 6667–6672, 2004.
[157] Y. Yin, R. M. Rioux, C. K. Erdonmez, S. Hughes, G. A. Somorjai, and A. P. Alivisatos, “Formation of hollow nanocrystals through the nanoscale Kirkendall effect,” *Science*, vol. 304, pp. 711–714, 2004.
[158] P. Michorczyk, P. Ku´strowski, A. Kolak, and M. Zimowska, “Ordered mesoporous Ga_2O_3 and Ga_2O_3–Al_2O_3 prepared by nanocasting as effective catalysts for propane dehydrogenation in the presence of CO_2,” *Catal. Commun.*, vol. 35, pp. 95–100, 2013.
[159] B. Zheng, W. Hua, Y. Yue, and Z. Gao, “Dehydrogenation of propane to propene over different polymorphs of gallium oxide,” *Journal of Catalysis*, vol. 232, pp. 143–151, 2005.
[160] “Dehydrogenation of Propane Over a Silica-Supported Gallium Oxide Catalyst.” .
[161] B. Xu, B. Zheng, W. Hua, Y. Yue, and Z. Gao, “Support effect in dehydrogenation of propane in the presence of CO_2 over supported gallium oxide catalysts,” *J. Catal.*, vol. 239, 2006.
[162] M. Salmeron and R. Schlögl, “Ambient pressure photoelectron spectroscopy: A new tool for surface science and nanotechnology,” *Surf. Sci. Reports*, vol. 63, pp. 169–199, 2008.
[163] M. E. Grass, P. G. Karlsson, F. Aksoy, M. Lundqvist, B. Wannberg, B. S. Mun, Z. Hussain, and Z. Liu, “New ambient pressure photoemission endstation at Advanced Light Source beamline 9.3.2,” *Rev. Sci. Instrum.*, vol. 81, 2010.
[164] M. Kunz, A. A. MacDowell, W. A. Caldwell, D. Cambie, R. S. Celestre, E. E. Domning, R. M. Duarte, A. E. Gleason, J. M. Glossinger, N. Kelez, D. W. Plate, T. Yu, J. M. Zaug, H. A. Padmore, R. Jeanloz, A. P. Alivisatos, and S. M. Clark, “A beamline for high-pressure studies at the Advanced Light Source with a superconducting bending magnet as the source,” *J Synchrotron Rad*, vol. 12, pp. 650–658, 2005.
[165] E. A. Redekop, V. V. Galvita, H. Poelman, V. Bliznuk, C. Detavernier, and G. B. Marin, “Delivering a Modifying Element to Metal nanocrystals via Support: Pt–Ga Alloying during the Reduction of Pt/Mg(Al,Ga)O x Catalysts and Its Effects on Propane Dehydrogenation,” *ACS Catal.*, vol. 4, pp. 1812–1824, 2014.
[166] S. Santra, R. Tapec, N. Theodoropoulou, J. Dobson, A. Hebard, and W. Tan, “Synthesis and characterization of silica-coated iron oxide nanoparticles in microemulsion: the effect of nonionic surfactants,” *Langmuir*, vol. 17, pp. 2900–2906, 2001.
